Hybrid Axial and Cross-Flow Fan Propulsion for Transonic Blended Wing Body Aircraft

NASA Contract NNX11CD95P
Phase 1 Final Report
September 29, 2011

Investigators:
Joe Kummer, PhD
JB Allred

Acknowledgements

The work presented in this report summarizes a Phase I SBIR effort funded by NASA Glenn Research Center. We would like to thank James Felder and Hyun Dae Kim from NASA GRC for their support of this research and extensive technical inputs. Also, we would like to acknowledge Matthew Rosanio for all of his efforts in creating the 3D BWB models and photorealistic renderings. Lastly, we would like to thank Julio Chu from NASA for providing the baseline BWB geometry.

Phase I Project Summary

Firm: Propulsive Wing, LLC
Contract Number: NNX11CD95P
Project Title: Hybrid Axial and Cross-Flow Fan Propulsion for Transonic Blended Wing Body Aircraft

Identification and Significance of Innovation:

Ideally, standard fan/engine designs can directly be embedded within the airframe of a vehicle. Unfortunately, doing so causes both performance penalties and structural challenges due to boundary layer flow ingested into the propulsors. For the present design concept, a dual-propulsion axial fan (AF) and cross-flow fan (CFF) system is investigated. This system provides the excellent efficiency of the axial fan, but with the benefit of the cross-flow fan system providing boundary layer flow mitigation. The purpose of this research was to develop the necessary computational tools to analyze this configuration, and then to show that the combined propulsor solution has performance benefits over the single axial fan system.

Technical Objectives and Work Plan:

The research performed during this SBIR Phase I effort included development of the basic theory for implementation of a hybrid axial/cross-flow fan propulsion system into a transonic BWB airframe, development of black-box CFD models for both cross-flow fans (BBCFF) and axial fans (BBAF), a parametric CFD study of a 2D airfoil section with axial fan and axial/cross-flow fan propulsors, and a first pass analysis of overall system integration. The basic theory was derived from the mass and momentum conservation equations, as well as the standard compressible flow relations. An analytical method was developed to select cross-flow fan size, speed, and power requirements given the external local flow field near the airframe and the location of the propulsor inlet and outlet. A CFF airfoil tradeoff study was also performed, which investigated the relationship between CFF inlet and outlet height, fan diameter, fan speed, and power. These analyses provided the inputs necessary for the BBCFF model, which was integrated within an airfoil comprising the mid-span of a baseline blended-wing-body (BWB) vehicle.

Technical Accomplishments:

Results from the CFD simulations clearly demonstrate the potential for reducing the efficiency penalty incurred by the axial fan due to inlet non-uniformity. Axial fan compression efficiency improvements of up to 2.5% were shown when the CFF propulsor was included in the calculation. In addition, clear trends exist between net lift and drag coefficients, total pressure ratio, and fan parameters. Lastly, the CFD data showed significant changes in the flow field around both the 2D airfoil, as well as the full 3D BWB due to the inclusion (or exclusion) of the distributed propulsors. This demonstrates that it is impossible to segregate the airframe force calculations from those for the individual fans. Instead, net lift and net drag must be calculated by directly integrating pressure and shear forces around all external surfaces (including the pressure force over the inlet and outlet control surfaces), and then adding to these values the force due to the momentum fluxes through the propulsors.

Justification for Phase II Continuation:

The Phase I work lays a solid foundation for the Phase II continuation. In Phase II, we propose a series of wind tunnel tests on an axial fan that will directly measure the performance penalty due to boundary layer ingestion. This data will then be used to validate CFD simulations, which will look further at the near-fan flow field to determine the local compression efficiency across the fan rotor. This data will be used to refine the models developed during Phase I. A robust CFD design methodology will be implemented in Phase II to develop a new baseline BWB vehicle with combined axial and cross-flow fan propulsion. The methods developed here will also be applicable to many other propulsion and airframe configurations, and hence have the potential for a wide impact within the aeronautics community.

NASA Application(s):

Analytical and computational tools for embedded, distributed engine aircraft design; manned and unmanned blended-wing-body aircraft

Non-NASA Commercial Application(s):

Small UAVs with turboelectric propulsion; High altitude, long endurance UAVs; New design methodologies for future aircraft designs

Name and Address of Principal Investigator:

Joseph Kummer, PhD
Propulsive Wing, LLC
321 Rt. 5
PO Box 321
Elbridge, NY 13060

Name and Address of Offeror:

Propulsive Wing, LLC
321 Rt. 5
PO Box 321
Elbridge, NY 13060

Introduction and Motivation for the Project

Utilization of embedded, distribution propulsion has the potential to greatly improve the cruise efficiency of next-generation transport aircraft through the ingestion of the low-momentum wake created by the surface of the wings and/or body of the vehicle into the propulsor and re-energizing of the vehicle wake. The blended-wing-body (BWB) vehicle design offers a perfect opportunity to utilize this type of propulsion system, since the majority of the viscous wake is produced by the centerbody section of the vehicle. In addition, the centerbody is thicker and wider than a standard fuselage, providing the space necessary for embedded propulsion.

Ideally, standard fan/engine designs could directly be embedded within the airframe of the vehicle. Unfortunately, doing so causes both performance penalties and structural challenges. For the present design concept, a distributed axial fan system is utilized. This type of propulsor provides excellent compression efficiency when the inflow distribution is uniform (i.e. uniform total pressure and total temperature distribution). However, previous work has demonstrated a significant efficiency penalty when a high degree of inflow distortion is present. The authors in Ref. 1 performed CFD simulations comparing the efficiency of 145 in and 76 in diameter axial fans operating with either uniform inflow or a representative boundary layer inlet profile. The inlet profile used corresponded to the non-uniform boundary layer profile calculated from CFD simulations of an offset inlet duct. The results showed a 6% reduction in compression efficiency when the distorted inflow boundary conditions were used, corresponding to a distortion index (DI) of 24% and non-uniformity height of about 40% of the inlet height. In another CFD case run in the same study, the inlet flow conditions were allowed to redistribute during the calculation through the influence of the fan. For this case, DI was reduced to about 15%, with a corresponding efficiency penalty of about 3.5%.

Jang et al. preformed CFD simulations of a small axial fan with and without flow distortion at the fan blades[2]. In this case, the flow distortion was produced by a flattened fan hub, which created an area of separated flow just beyond the hub. As expected, the fan efficiency dropped significantly, about 16%, when the fan was required to operate with a portion of the inflow comprising separated flow (i.e. very large distortion). However, even if the fan was placed far enough downstream such that it was behind the separated flow region, the efficiency penalty remained over 6%. The important point here is that even moderate amounts of flow distortion greatly impact the performance of axial fans.

The primary goals of this effort were:

1. Development of a basic theory and design procedure for implementing a hybrid Axial fan/Cross-flow fan (AF/CFF) propulsion system into a transonic blended wing body airframe.

2. Development of black-box CFD models for both cross-flow fan and axial fan propulsion systems.
3. Demonstration, through analytical and CFD calculations, that such a system offers performance gains over a propulsion system utilizing solely distributed axial fans.
4. Perform a first-pass analysis of overall system integration.

Description of Phase I Work Performed

Formulation for Design of CFF Propulsion System and Integration Within Airfoil

As a baseline case, the centerline airfoil geometry of the N3-X was used for the first part of this study. Before integrating the propulsors into the airfoil, a CFD calculation was performed for the airfoil alone. The altitude was set to 35,000 ft, angle of attack to zero, and Mach number to 0.75. A calculation was originally run corresponding to a freestream Mach Number of 0.85; however, this resulted in a stronger shock and higher Mach number values near the propulsor inlet when compared with Ref. 3. This was a result of the current calculations being 2-dimensional, as opposed to the full 3D vehicle geometry, thus the lack of 3D relieving. Regardless, the purpose here was to perform tradeoff studies and develop the cross-flow fan and axial fan modeling techniques, which can all be accomplished in 2D before moving to the full 3D design case. The computational mesh for this case is shown in Fig. 1. For this study, the cross-flow fan inlet was placed at the 85% chord location and outlet placed at 95% chord. Figure 2 shows the Mach number contours for this case, Fig. 3 the total pressure contours near the trailing edge, and Fig. 4 the total pressure and Mach number distribution at the propulsor inlet.

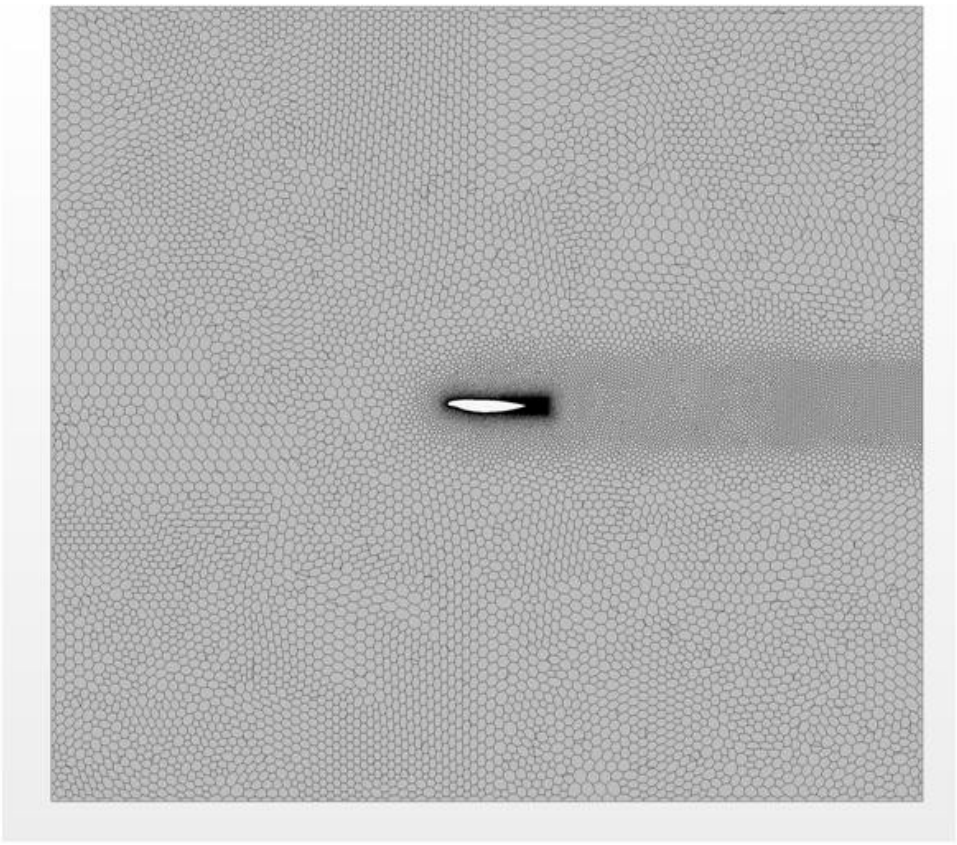

Fig. 1: BWB centerline computational mesh

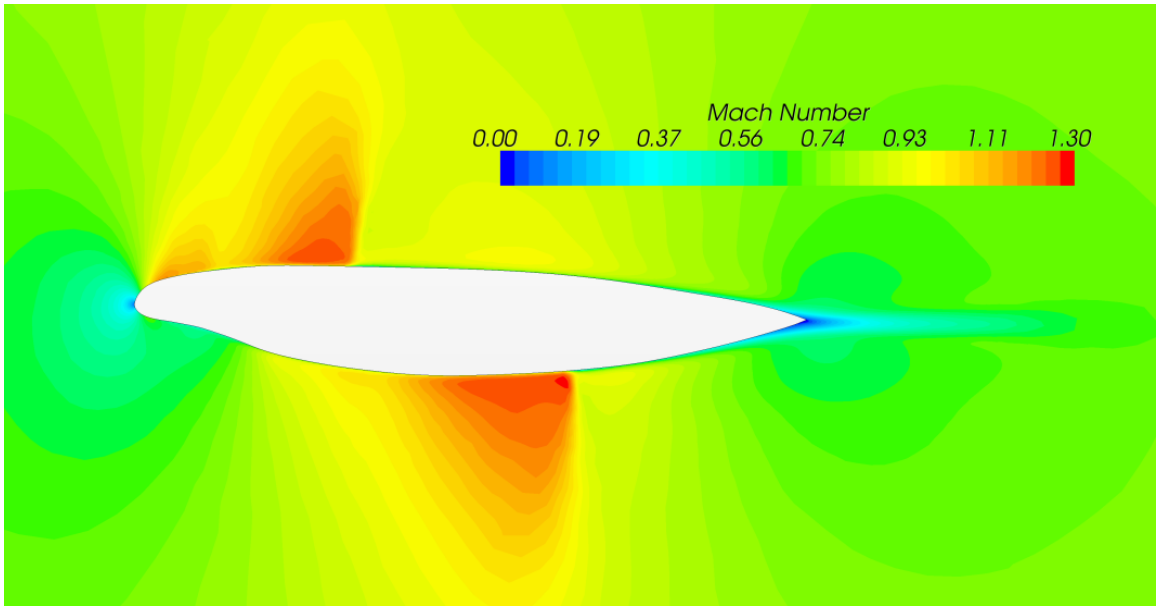

Fig. 2: Mach number contours

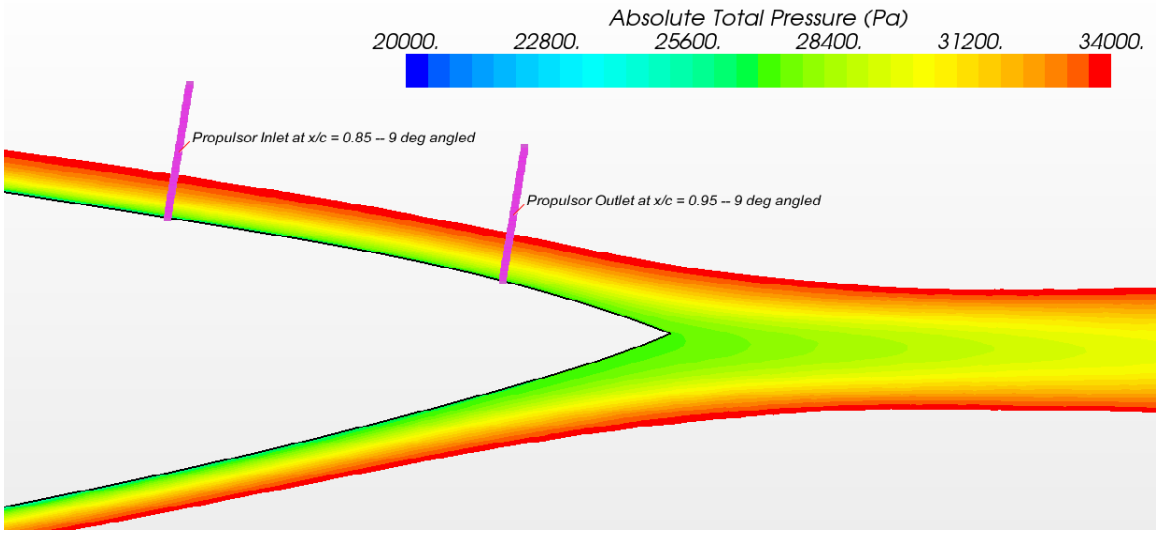

Fig. 3: Total pressure contours near trailing edge

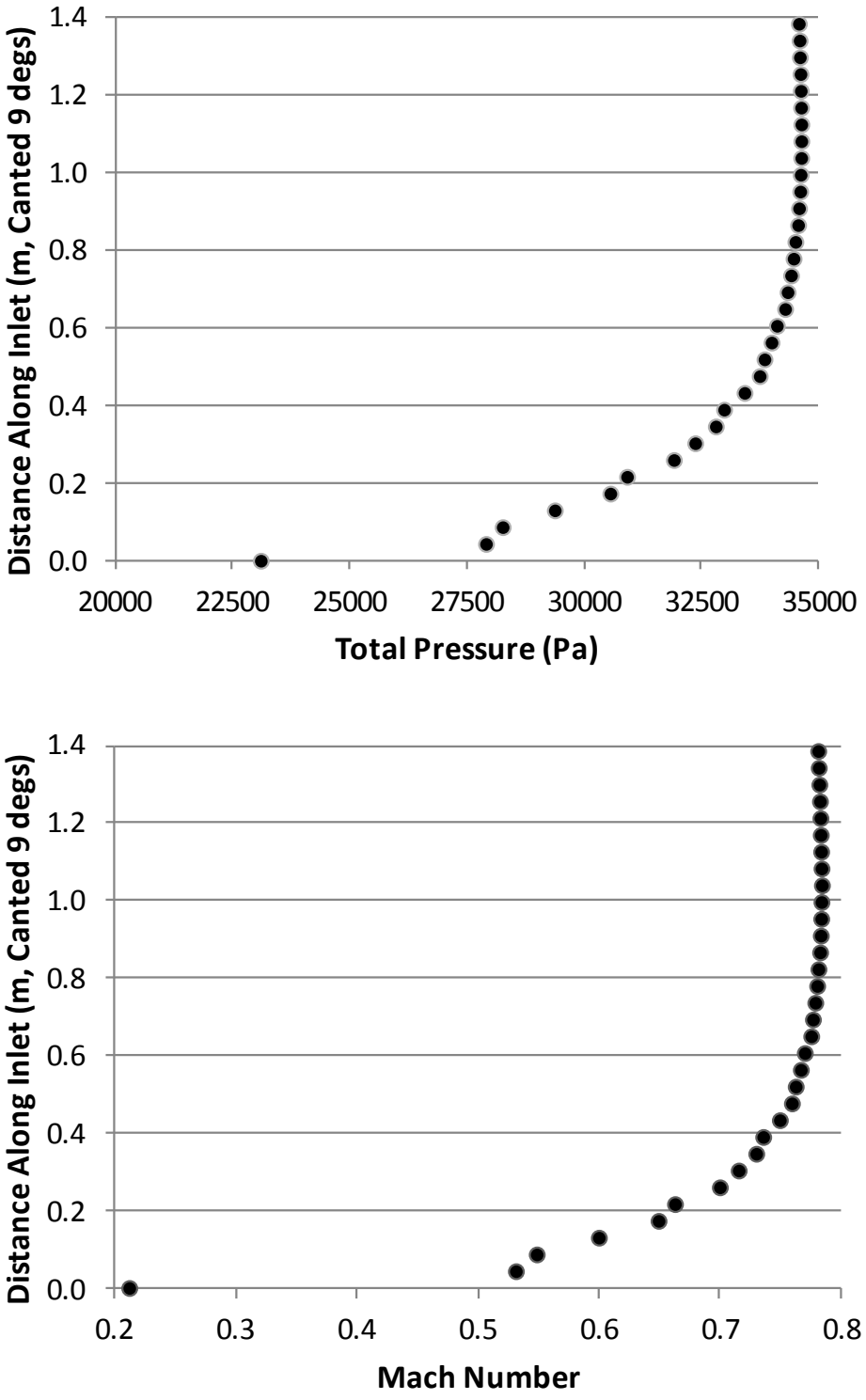

Fig. 4: Graphs of total pressure and Mach number along propulsor inlet

Before integrating a cross-flow fan design into the BWB centerbody airfoil section, a baseline CFF housing design, as well as a method for properly sizing the fan, inlet and outlet duct, and determining fan speed needed to be derived. This is inherently an iterative process, since the sizing calculations depend on the CFF performance, while the performance is affected by the airfoil integration itself. The fan operating point was changed by varying the output static pressure. Total pressure contours at three different operating points are shown in Fig. 5. For this case, the fan diameter was set to 1 ft and the fan speed to 4,000 rpm. The inlet parameters were set to the freestream values: 35000 ft altitude standard atmosphere, P = 23842.7 Pa, ρ = 0.37959 kg/m^3, T = 218.8 K, M = 0.6.

Fan performance is presented as total pressure coefficient and compression efficiency versus flow coefficient. The definition of flow coefficient is given in Eq. 1, total pressure coefficient in Eq. 2, and compression efficiency in Eq. 3. The performance results for these cases are graphed in Fig. 6.

$$\phi = \frac{\dot{m}}{\rho_o D_f U_f} \tag{1}$$

$$\psi_t = \frac{\Delta P_T}{\frac{1}{2}\rho_o U_f^2} \tag{2}$$

$$\eta_c = \frac{[\Delta T_T]_{isentropic}}{[\Delta T_T]_{actual}} = \frac{\left(\frac{P_{T_{out}}}{P_{T_{in}}}\right)^{\left(\frac{\gamma-1}{\gamma}\right)} - 1}{\left(\frac{T_{T_{out}}}{T_{T_{in}}}\right) - 1} \tag{3}$$

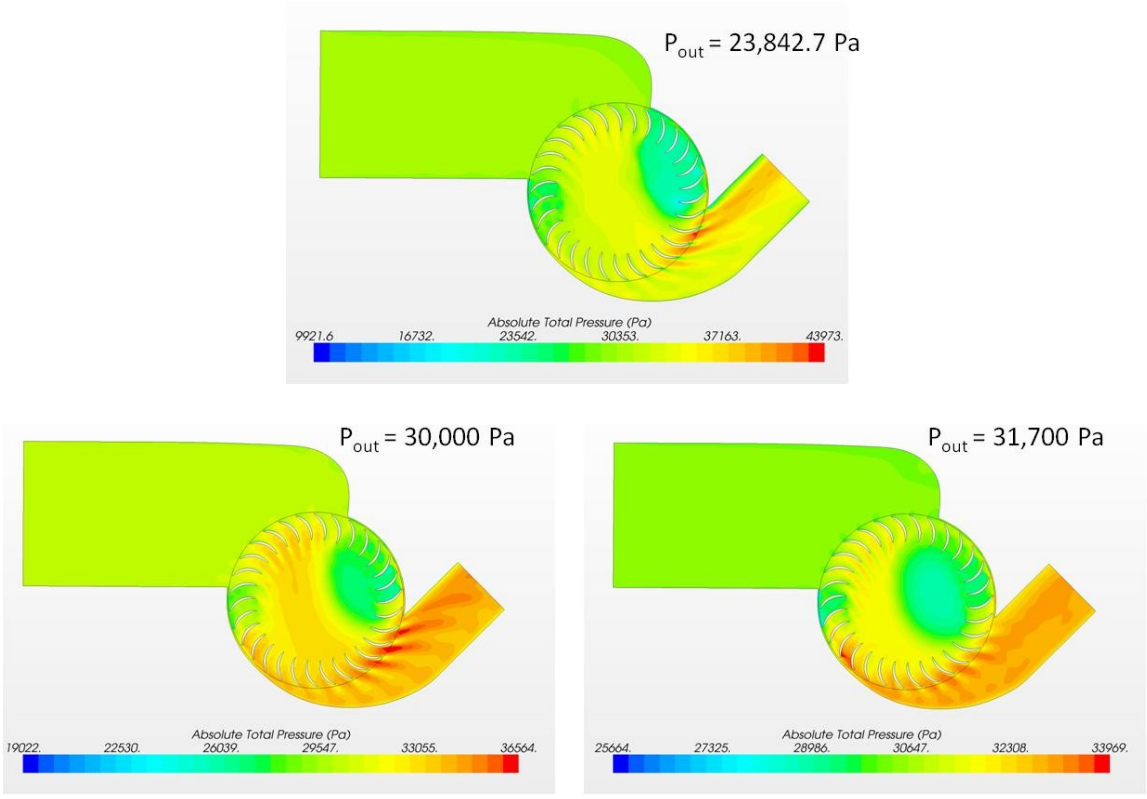

Fig. 5: Total pressure contours for baseline CFF

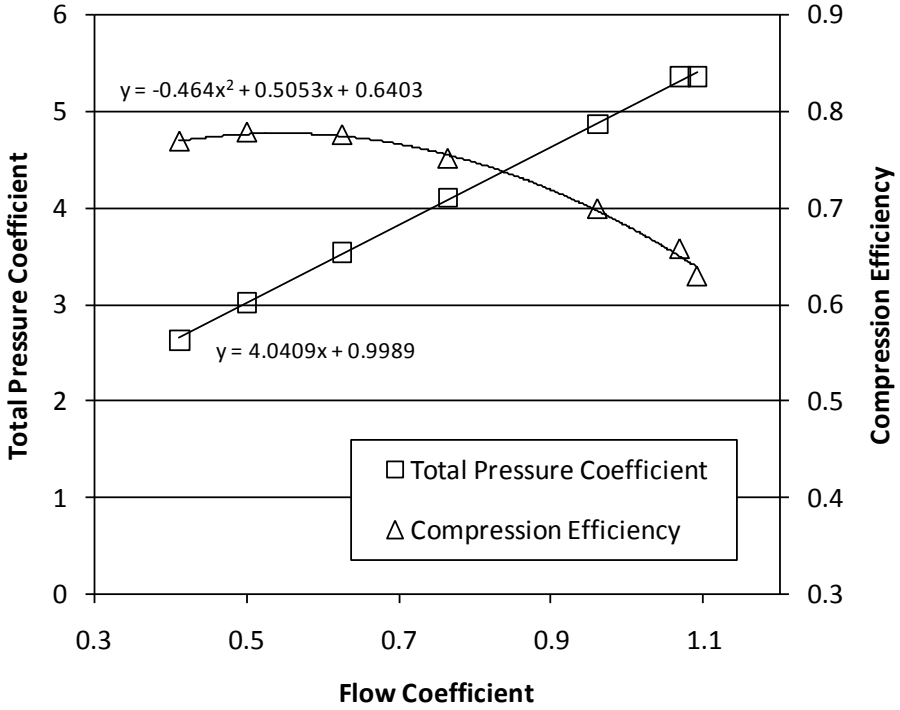

Fig. 6: Baseline CFF fan performance

The process for sizing and integrating the cross-flow fan propulsion system into a transonic airfoil is derived next. The test case here will be the BWB centerline airfoil. The process is as follows:

Given the freestream conditions, for example, 35000 ft altitude standard atmosphere, P = 23842.7 Pa, ρ = 0.37959 kg/m^3, T = 218.8 K, speed of sound (a) = 296.54 m/s. Thus freestream total pressure (P_{T_∞}) = 34,626.46 Pa, freestream total temperature (T_{T_∞}) = 243.42 K, and freestream stagnation density (ρ_{o_∞}) = 0.5 kg/m^3.

Next given the boundary layer profile at the proposed CFF inlet location (for example, the profile shown in Fig. 4 derived from the airfoil-alone CFD simulation), select the CFF propulsor inlet height, and hence the mass flow rate (assuming minimum disturbance to the baseline case). For the current example, an inlet height of 6" was selected, resulting in an inlet mass flow rate of 7.83 kg/s.

Now knowing the inlet flow properties, given the fan performance curves, shown as the polynomial curve fits in Fig. 6, the flow coefficient is selected. Ideally the flow coefficient will be at or near the maximum efficiency point on the curve; however, by adjusting the design flow coefficient, in turn the fan diameter can be adjusted to meet other design criteria. In the present test case, the flow coefficient was selected to match a 1 ft diameter fan.

The outlet total pressure is determined based on the requirements of the design. For the test case, the total pressure was set to the freestream value.

Next the tip speed (U_f), fan diameter (D_f), and fan speed (Ω) are solved for using Eqs. 4, 5, and 6, respectively.

$$U_f = \sqrt{\frac{\Delta P_T}{\frac{1}{2}\rho_o \psi_t}} \tag{4}$$

$$D_f = \sqrt{\frac{\dot{m}}{\rho_o U_f \phi}} \tag{5}$$

$$\Omega = \frac{2U_f}{D_f} \tag{6}$$

By selecting the outlet location, the local static pressure is known. Assuming this will not change appreciably with the addition of the propulsor, the outlet total temperature ($T_{T_{out}}$), Mach number (M_{out}), temperature (T_{out}), density (ρ_{out}), and speed of sound (a_{out}) are solved for using Eqs. 7-11. For the test case presented, a value of 25,101 Pa was used for the outlet static pressure.

$$T_{T_{out}} = T_{T_{in}} \left\{ \frac{1}{\eta_c} \left[\left(\frac{P_{T_{out}}}{P_{T_{in}}} \right)^{\left(\frac{\gamma-1}{\gamma}\right)} - 1 \right] + 1 \right\} \tag{7}$$

$$M_{out} = \sqrt{\frac{2}{\gamma - 1}} \left[\left(\frac{P_{T_{out}}}{P_{out}} \right)^{\left(\frac{\gamma-1}{\gamma}\right)} - 1 \right] \tag{8}$$

$$T_{out} = \frac{T_{T_{out}}}{1 + \frac{\gamma - 1}{2} M_{out}^2} \tag{9}$$

$$\rho_{out} = \frac{P_{out}}{R T_{out}} \tag{10}$$

$$a_{out} = \sqrt{\gamma R T_{out}} \tag{11}$$

Finally, the outlet height is solved for using Eq. 12.

$$h_{out} = \frac{\dot{m}}{\rho_{out} a_{out} M_{out}} \tag{12}$$

Also, the power input to the cross-flow fan can be derived from Eq. 13.

$$P = c_p \dot{m}\left(T_{T_{out}} - T_{T_{in}}\right) \tag{13}$$

Where for the present case c_p = 1005 J/kg-K. Holding D_f constant to 1 ft, the results from these calculations yield: ϕ = 0.7; Ω = 599.1 rad/s = 5,721 rpm; h_{out} = 0.1 m = 3.9"; P = 150.5 KW/m = 83.4 HP/ft.

For this design, the inlet and outlet were to be placed at the 85% and 95% airfoil chord locations, respectively, so in order to actually install the above CFF housing into the airfoil, the baseline inlet and outlet ducting needed to be extended. The inlet height was to be set to 6" and the outlet height to 3.9". These modifications were made and the CFF propulsion system was incorporated into the airfoil, as shown in Fig. 7. This case was run at M_∞ = 0.75, corresponding to the airfoil-alone case. Assuming there would be additional duct losses, the fan rpm was set to 6,000 rpm. Figure 8 shows the computational grid for this case, and Fig. 9 shows the total pressure contours near the trailing edge of the airfoil.

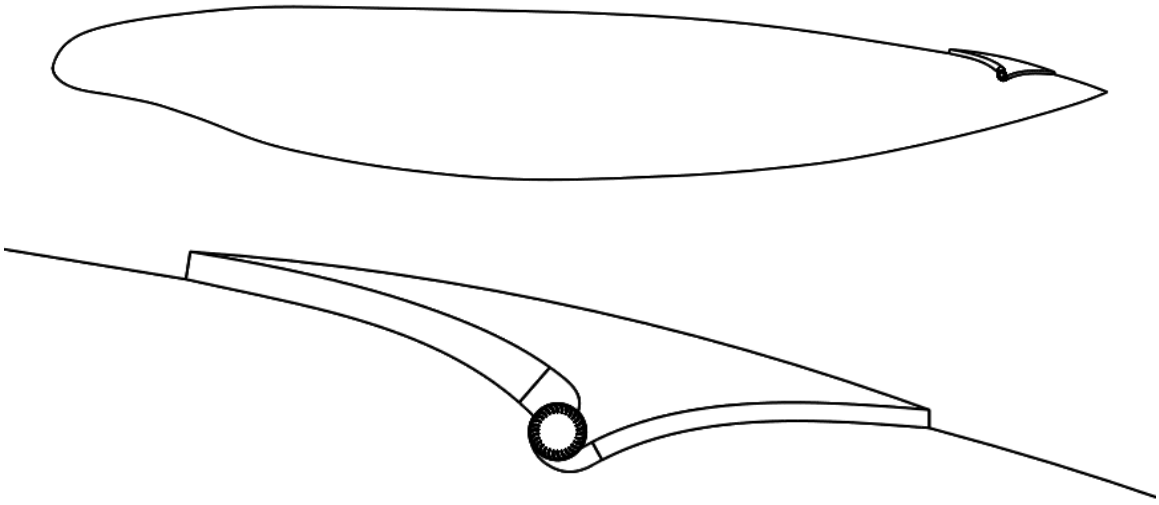

Fig. 7 CFF-Airfoil geometry

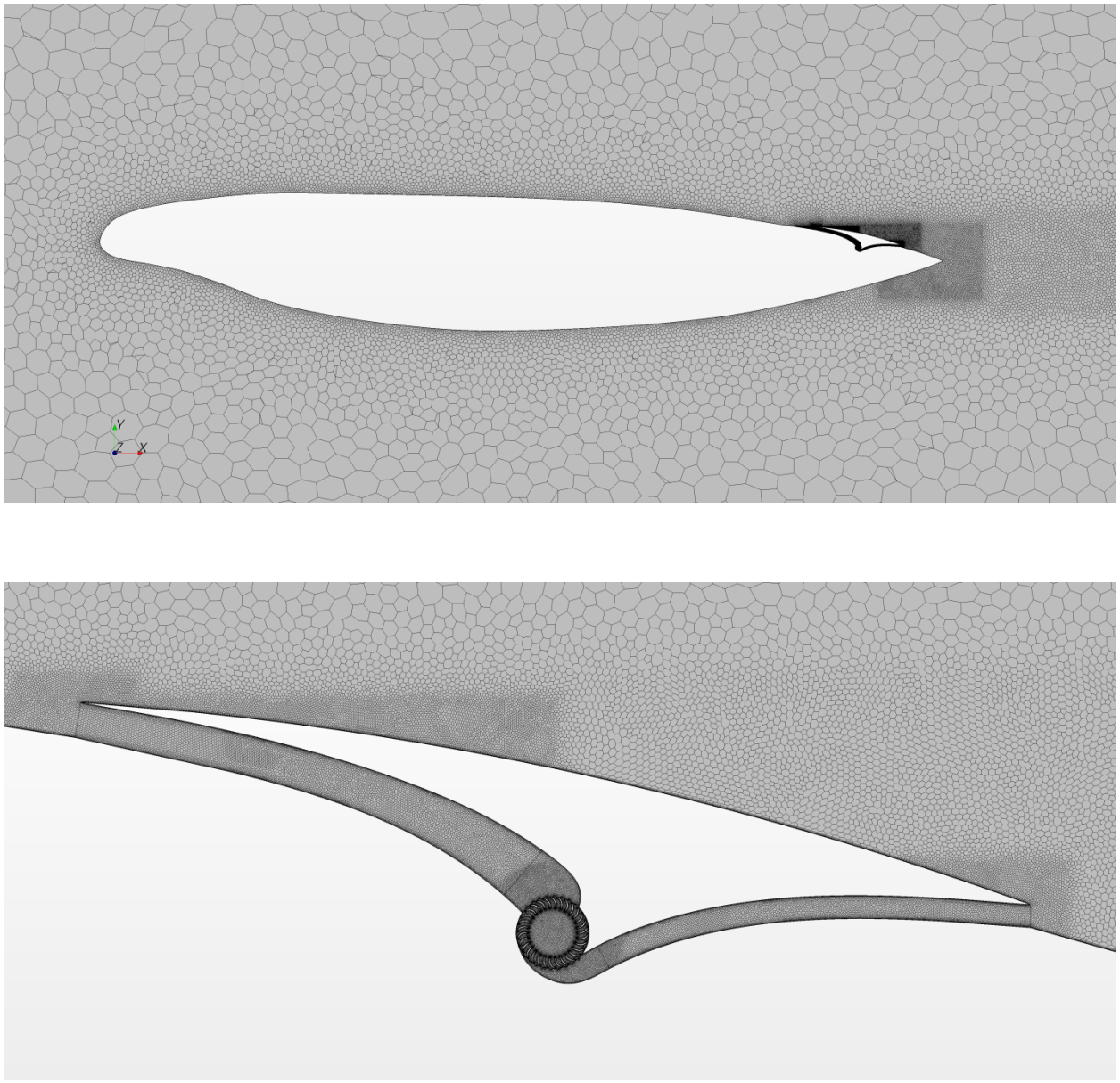

Fig. 8: CFF-Airfoil computational grid

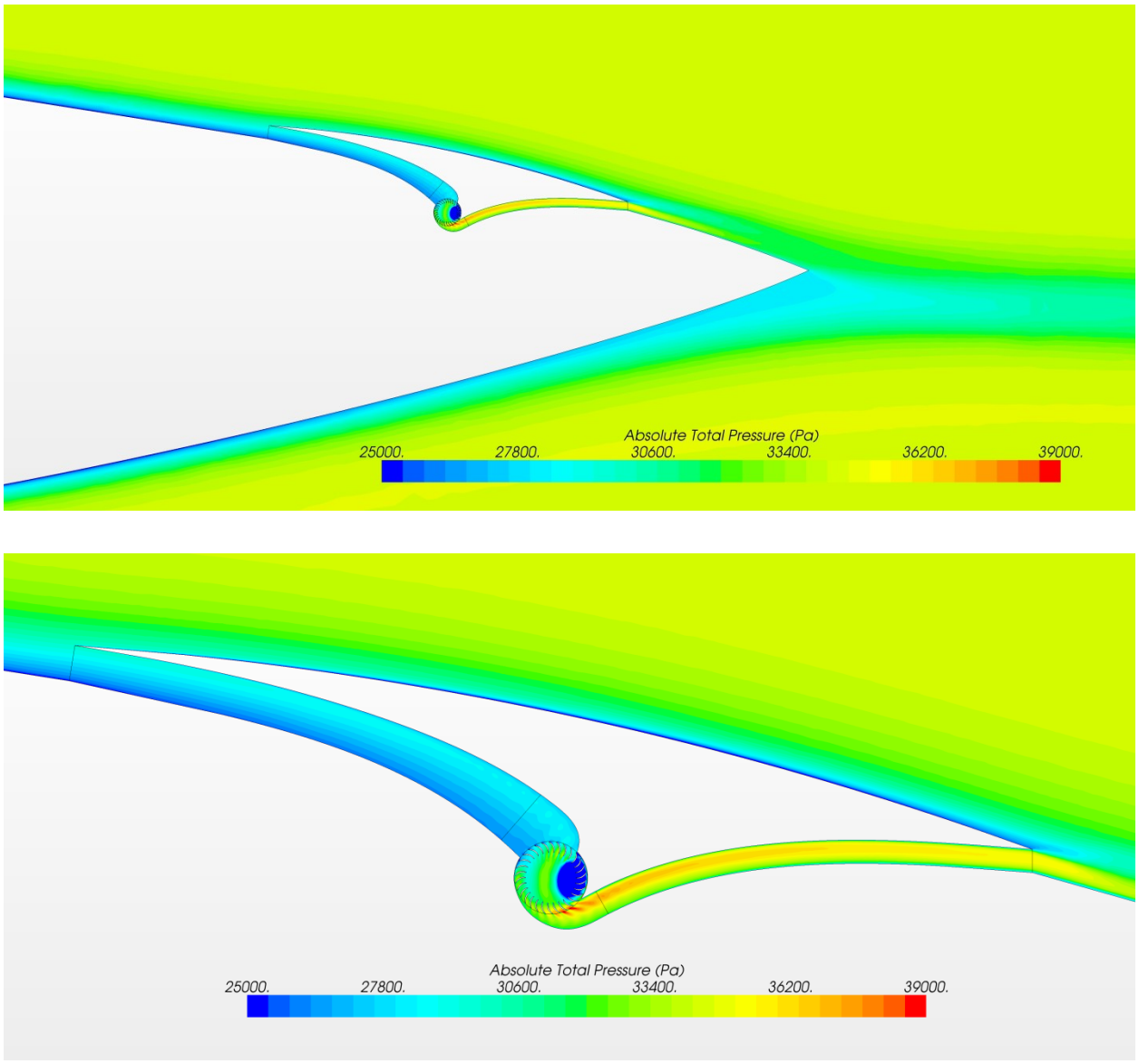

Fig. 9 Total pressure contours

For the present case, the efficiency was slightly lower than expected due to a non-optimized housing geometry (resulting in 61% compression efficiency). This in turn resulted in the mass flow rate being slightly less than the analytical predictions at 7.6 kg/s. Most of the losses, however, occurred within the duct and not the fan. Taking the values for total pressure and total temperature close to the fan, the calculated compression efficiency for the fan itself is 75%. Irrespective, it is clear that the basic integration procedure was successful, and that the cross-flow fan system is indeed capable of effectively mitigating the low momentum boundary layer fluid from the main propulsors, which would sit directly above the CFF system.

As a comparison, the total pressure profile at the axial propulsor inlet is plotted in Fig. 10 with and without the CFF system included. At this point the axial fan has yet to be included in the calculation; however, the effect of the CFF propulsor is clear. The CFF creates an environment whereby the axial fan can be utilized without the detriment of the thick boundary layer. In Fig. 10, the airfoil-alone data gives the total pressure measured up from the surface of the airfoil, whereas the data for the CFF-Airfoil plots the total pressure measured upward from the top of the CFF duct housing. It is clear from the graph that the CFF greatly reduces the total pressure deficit experienced by the axial fan. The assumption here is that without the CFF propulsion system, the axial fans would need to be placed such that their inlets come right down to the surface of the airfoil. However, with the CFF system in place, the axial fan would be mounted on top of the CFF ducting. The CFF system also takes the place of a series of pylons, which for distributed propulsion may be quite extensive, without the requisite addition in drag.

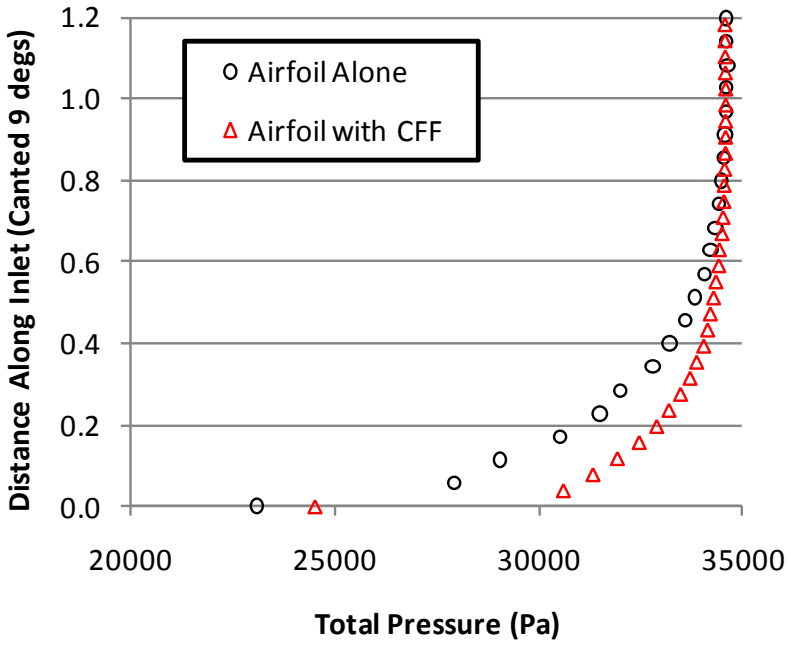

Fig. 10: Wake total pressure profile at axial fan inlet (85% chord location)

To complete this discussion, fan performance curves were generated for the CFF housing integrated within the airfoil. This was accomplished by simulating the isolated housing and varying the back-pressure, as was done previously for the baseline geometry. Fig. 11 shows a representative output for these cases (total pressure contours), and Fig. 12 gives the fan performance curves. Although the performance shown is higher than for the case where the housing was integrated into the airfoil, most of the additional losses were found to occur in the ducting itself, and more specifically in the outlet duct. With further optimization these losses can likely be minimized. The fan performance curves given in Fig. 12 will be utilized in the development of the black-box CFF model. For comparison, Fig. 13 gives the performance for the

fan itself (i.e. the total pressure and total temperature values are taken close to the fan). The difference between Figs. 12 and 13 represents the losses in the duct.

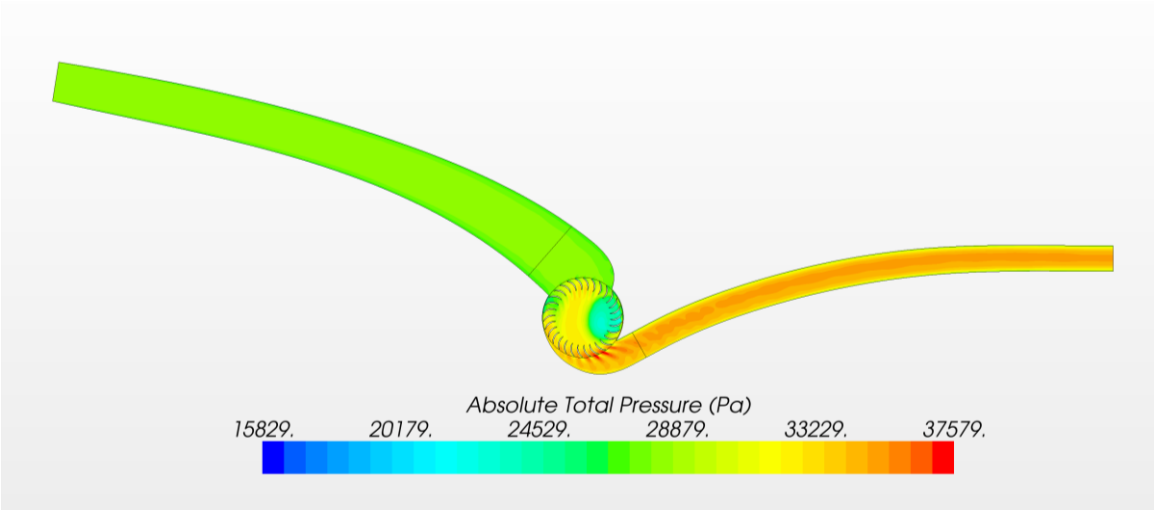

Fig. 11: Total pressure contours for isolated CFF housing

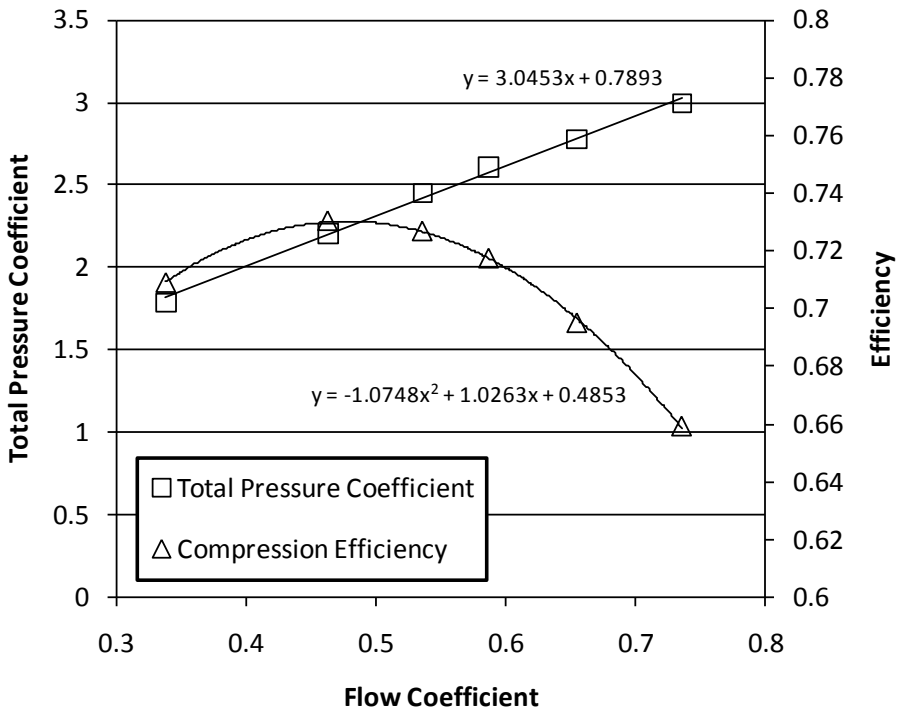

Fig. 12: Fan performance curves for isolated CFF housing: full duct

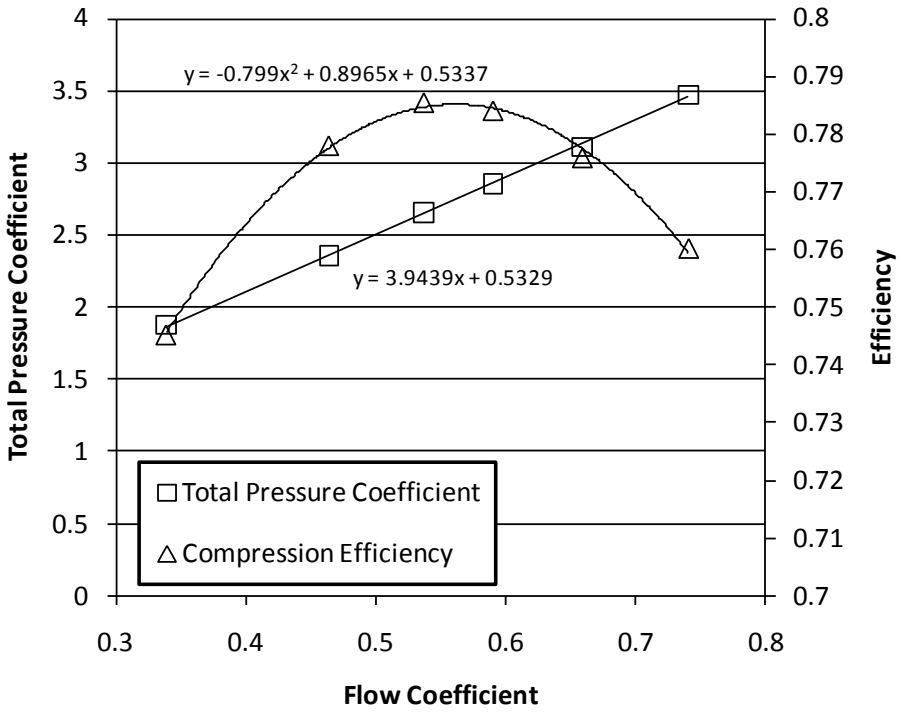

Fig. 13: Fan performance curves for isolated CFF housing: near fan

CFF Airfoil Tradeoff Study

Using the airfoil-alone case and the fan performance given in Fig. 12, a tradeoff study was performed to investigate the interrelations of the various parameters. Using the previous method (i.e. from the airfoil-alone case), mass flow rate and mass-averaged total pressure are plotted in Fig. 14 versus cross-flow fan inlet height. These calculations assume that the flow entering the fan is only what contacts the virtual inlet shown in Fig. 3. As a result, the streamlines above the inlet are essentially unaffected by the presence of the cross-flow fan propulsor.

Multiple proposed designs were derived using this data and varying both the inlet height (from 3" to 10") and the flow coefficient (from 0.3 to 1.0). Figure 15 plots the fan diameter versus the inlet height over the range of flow coefficients. As inlet height increases, the fan diameter must also increase to maintain a constant flow coefficient. In addition, as the flow coefficient increases, the fan diameter decreases.

For reduced weight, a CFF as small as possible would be ideal; however, by reducing the size of the fan, there are other tradeoffs. The first is increased fan speed. Although in this system analysis fan speed does not directly influence performance, there are clearly structural issues that would prohibit a small fan from operating at very high rpm. In a cross-flow fan, the blades are typically supported along the span using divider plates. This reduces the local bending of the

blades due to aerodynamic and centrifugal forces. As the fan size reduces, however, the blade thickness, and hence blade stiffness, also decreases. Thus practically it may be necessary to make small efficiency concessions in order to build a structurally robust fan system.

In the design process, an important parameter is the outlet height, which for these cases can be selected from the plot in Fig. 17. The effects of inlet height and flow coefficient on the required power input are shown in Fig. 18. Since a larger inlet results in higher mass flow rate, it is not surprising that as inlet height increases (for a constant outlet total pressure) the power required to drive the fan also increases. In addition, the graph demonstrates that the required power is a minimum at the flow coefficient corresponding to the maximum efficiency point of the fan.

One must bear in mind, however, that for a given inlet height, not all fan diameters can be selected, as shown in Fig. 19. By selecting the desired inlet height, there is a range of acceptable fan diameters that can be selected. In addition, CFF operation is typically best between flow coefficient values of 0.5 and 0.8. Above $\phi = 0.8$, the efficiency quickly diminishes; however, operation below $\phi = 0.4$ is usually not recommended, since the flow direction can become unstable (typically around $\phi = 0.3$).

The results of these calculations show that for an airfoil propelled solely by a cross-flow fan, best operation is to properly size the fan such that it operates close to the maximum efficiency point (here at about $\phi = 0.5$). Based on the results shown in Fig. 19, there is a range of values that will lead to near-minimum input power. For practical implementation, a smaller fan will reduce both structural weight, as well as lead to small (higher rpm) motors, due to the lower torque requirements.

In addition to the above design criteria, there are two more important parameters that need to be considered. The first is the effect of duct size on fan efficiency, due to both total pressure losses within the duct itself, as well as integration issues of a duct of considerably different size than the fan (for example, a very large inlet and outlet coupled with a small fan, or vice versa). It is anticipated that issues such as these can be overcome with careful detailed design of an actual system. The second, and one of the primary focuses of this work, is the effect of axial fan performance (in the presence of the CFF) on the efficiency of the complete system. This will be investigated by using black-box models of both the CFF and axial fan propulsors. The derivation of the necessary equations and implementation of these models into CFD simulations is discussed next.

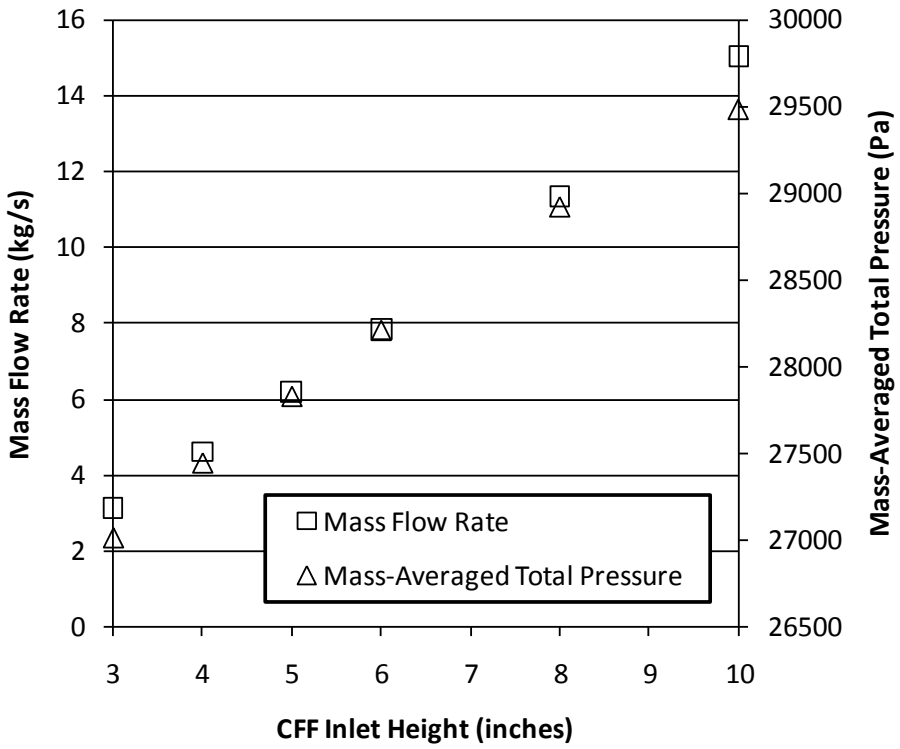

Fig. 14: Mass flow rate and total pressure versus cross-flow fan inlet height

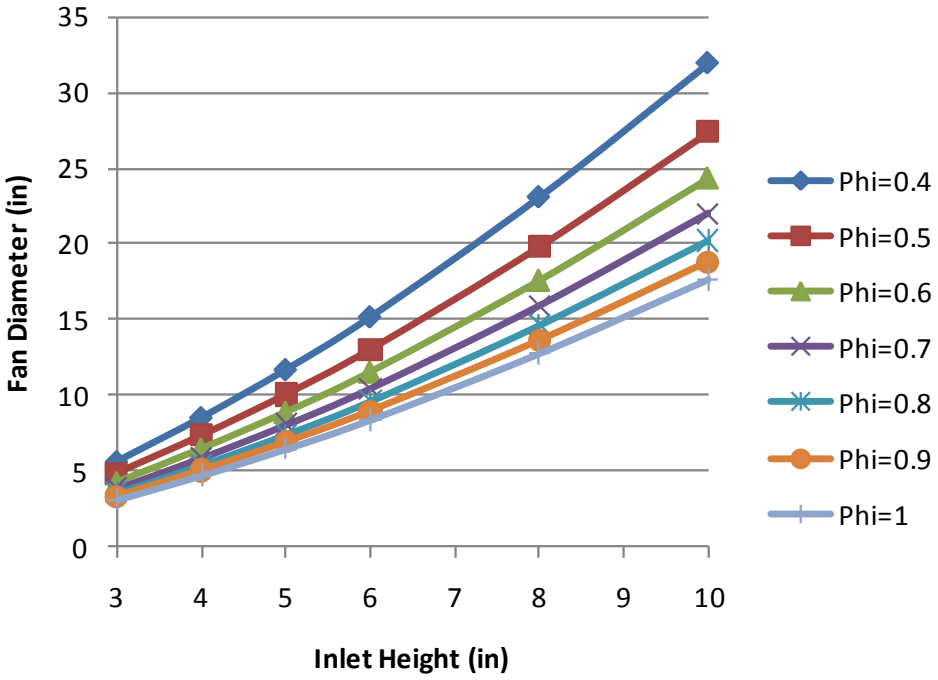

Fig. 15: Fan diameter versus cross-flow fan inlet height

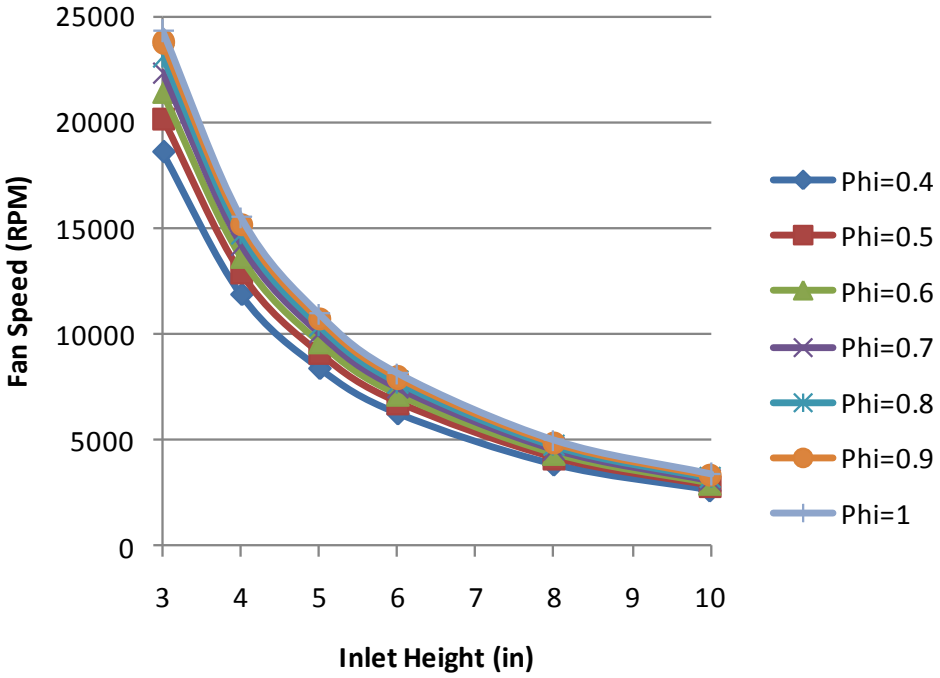

Fig. 16: Fan speed versus cross-flow fan inlet height

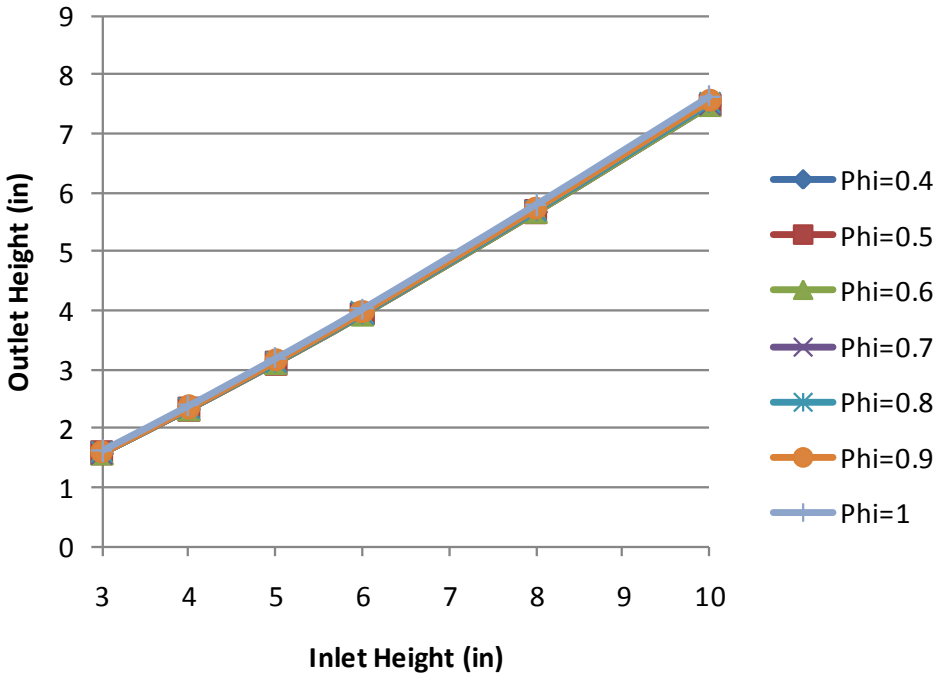

Fig. 17: CFF Outlet height versus inlet height

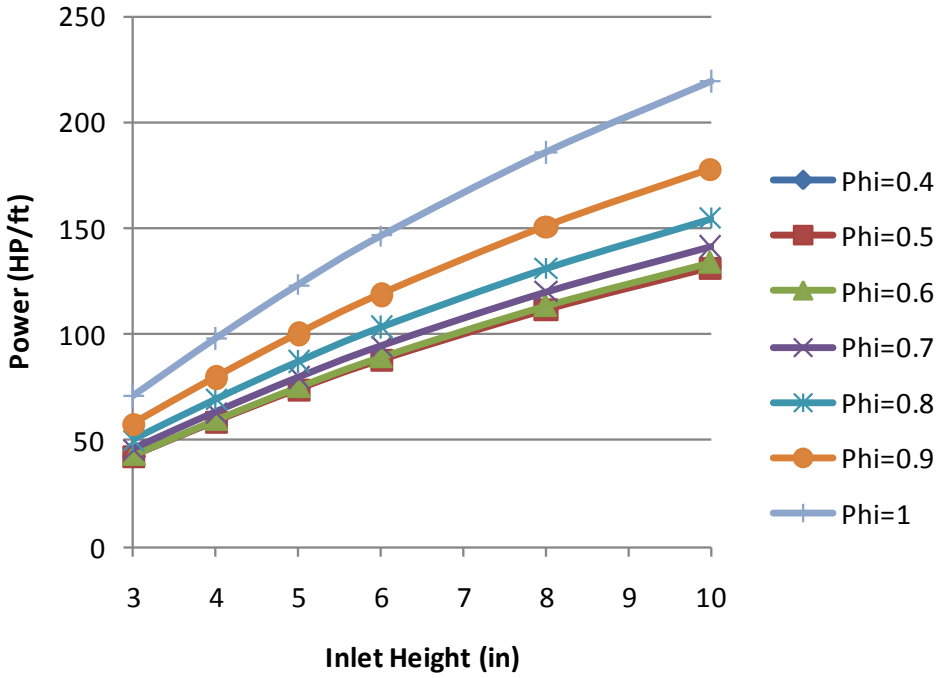

Fig. 18: Power versus CFF inlet height

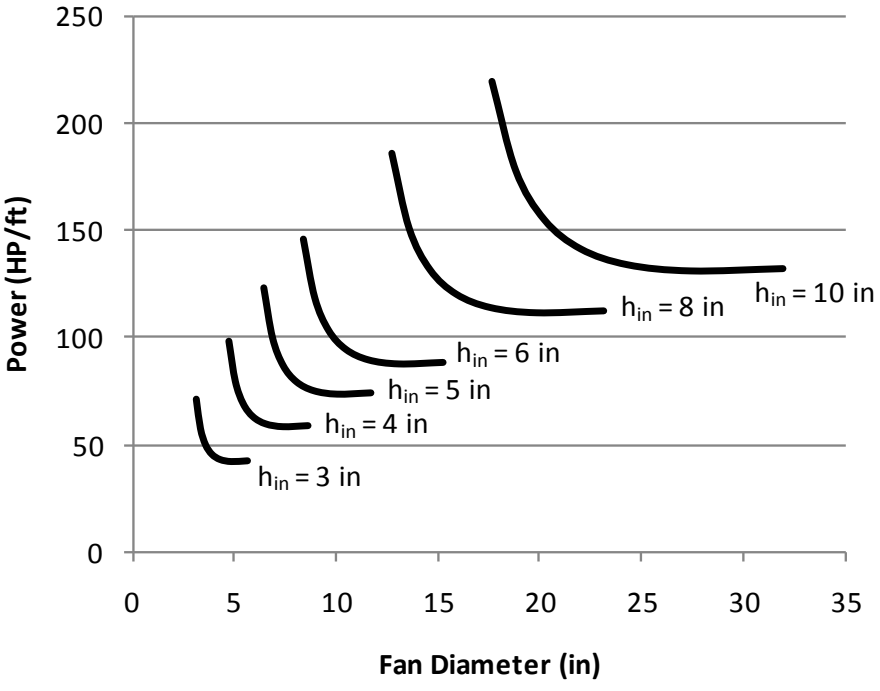

Fig. 19: Power versus fan diameter

Black-Box CFF Model

A black-box model was implemented to simulate the effect of the CFF on the external aerodynamics. The model replaces the entire fan and duct by a single inlet and outlet. Within the context of the CFD calculations, the propulsor inlet is simulated as a pressure outlet, while the propulsor outlet is simulated as a stagnation inlet. Each iteration two adjustments are made. The first is at the inlet, where the static pressure at this boundary is modified to bring the mass flow rate into the propulsor inlet (out the pressure outlet boundary) to the desired level. For the baseline cases, this was selected as the mass flow rate corresponding to the CFF-Airfoil simulations previously described; however, the mass flow rate can just as easily be set to any other value. This capability is built into the Star-ccm+ CFD software.

The second adjustment modulates the total pressure and total temperature at the propulsor outlet (i.e. at the stagnation inlet boundary) so that: 1) the mass flow rate remains equal at both the propulsor inlet and outlet, and 2) the total pressure and total temperature rise fall along the performance curves for the fan. Each iteration the mass flow rate is checked. If the mass flow rate at the fan outlet is too high, the flow coefficient is reduced, thus moving the operating point to the left along the total pressure coefficient and compression efficiency curves. Likewise, if the mass flow rate is too low, the flow coefficient is increased. Under-relaxation coefficients were also included in the formulation to stabilize the solution. Once steady-state is reached, the actual operating point ϕ for the fan is known, thus allowing calculation of the fan speed and power.

As a test case, a simulation was run corresponding as closely as possible to the CFF-Airfoil case shown in Figs. 7-9. The freestream conditions were identical in each case, and the mass flow rate into the black-box CFF propulsor (BBCFF) was set to 7.6 kg/s to match the previous result. Figure 20 shows the total pressure contours near the propulsor, and agrees favorably with the previous results with the CFF included in the calculation. For example, the flow coefficient predicted by the BBCFF model was 0.6, whereas for the full CFF-Airfoil case $\phi = 0.65$. This difference was due to the aforementioned duct losses changing the performance curves slightly. In spite of this, the agreement is quite good between the two cases, thus providing a convenient formulation for incorporating the CFF propulsor into the calculation without the need to run unsteady (i.e. time-accurate) cases, thus reducing the time to convergence from over 1 week to less than 2 hours.

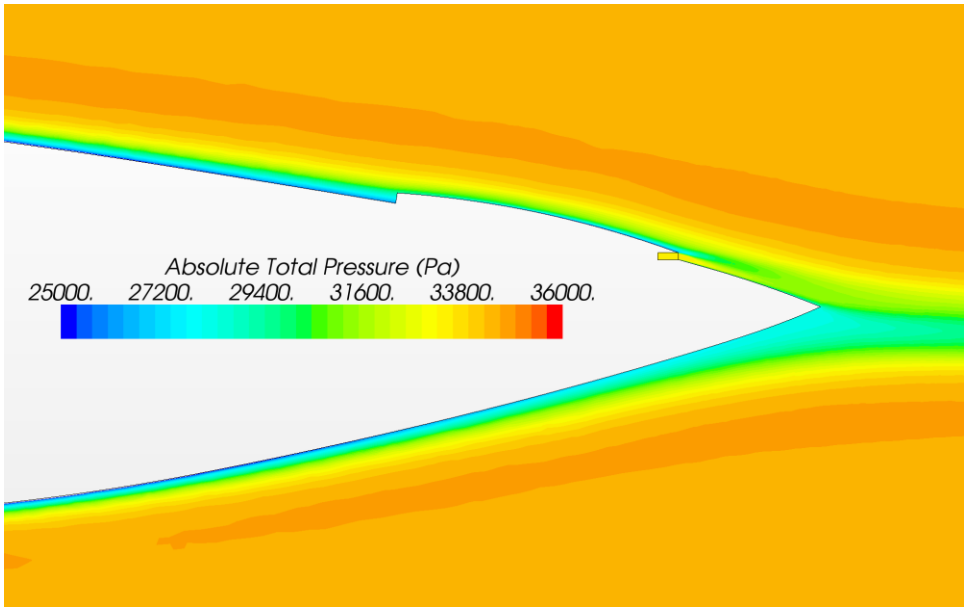

Fig. 20: Total pressure contours for BBCFF model test case

In order to compare the forces between the two cases (i.e. net lift and net drag), the force components resulting from the momentum flux through the propulsor need to be accounted for in the BBCFF case. For the case where the fan geometry is explicitly included, this is unnecessary, since the pressure and viscous forces can be summed over all wall surfaces (including the fan itself).

The method for performing this calculation involves summing the pressure and viscous forces over all external surfaces, and including in this the pressure forces along the propulsor inlet and outlet boundaries. As a test case, the simulation with the detailed fan geometry was used, since the results using either force calculation method should be identical. For the case simulated, the directly calculated lift was L = 109,550 N/m of span and drag D = 4,774 N/m. By comparison, the y-component of the force using the latter method (i.e. the black-box lift force) was L_{BB} = 109,435 N/m and black-box drag force was D_{BB} = 5,420 N/m. The forces due to the momentum flux were determined by multiplying the propulsor mass flow rate by the difference in velocity from inlet to outlet. Performing this calculation, $F_{x(mom)}$ = -646 N/m and $F_{y(mom)}$ = 115 N/m. Summing the black box and momentum forces, L_{net} = 109,550 N/m and D_{net} = 4,774 N/m, which are identical to the directly calculated values. Thus the second method for calculating the forces on the airfoil (i.e. with the propulsor operating but not explicitly included) is equivalent to simulating the fan itself and summing forces over all surfaces.

The same calculations were also performed for the BBCFF case. Here, D_{BB} = 5,300 N/m and L_{BB} = 100,500 N/m. From the momentum fluxes, $F_{x(mom)}$ = -643 N/m and $F_{y(mom)}$ = 37 N/m. Summing the black box and momentum forces, L_{net} = 100,537 N/m and D_{net} = 4,657 N/m.

Comparing these values with the ones calculated for the full 2D geometry, the lift for the BBCFF case is about 8% lower and the drag about 2% lower. This difference is primarily due to the lower fan performance in the unsteady case from propulsor inlet to outlet, which in turn alters the total pressure and total temperature at the outlet. In addition, a portion of this discrepency may be a result of the uniform profile used at the outlet and/or the interaction of this jet with the sharp corner immediately aft of the outlet. Potential fixes could involve imposing a non-uniform outlet profile, as well as rounding off this corner. Irrespective, the results show very favorable agreement between the full geometry and BBCFF models. To further show the correlation between the two models, the streamlines and wake total pressure profile are compared with the full geometry case in Figs. 21 and 22, respectively, and show excellent agreement.

Fig. 21 Comparison of streamlines for BBCFF and full geometry models

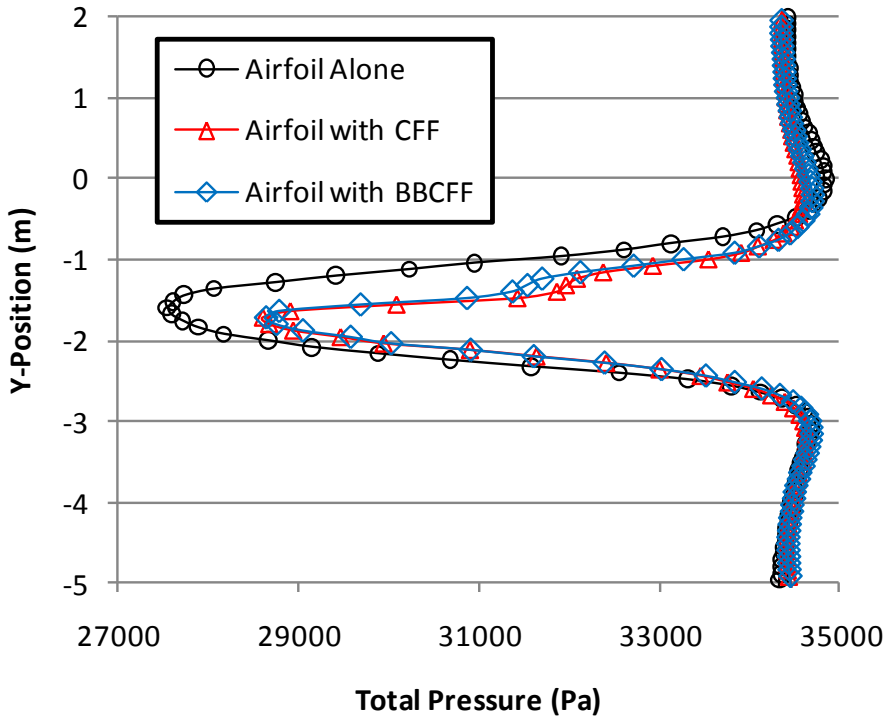

Fig. 22 Comparison of wake total pressure for BBCFF and full geometry models

Black-Box Axial Fan Model

In a similar manner to the BBCFF model, a black-box axial fan model (BBAF) was developed. The algorithm for this model is given below:

1. Given the inlet mass flow rate ($\dot{m}_{in}$), the flow properties at the inlet are known.
2. A guess for TPR is made, thus allowing calculation of the outlet total pressure ($P_{T_{out}}$).
3. Compression efficiency is calculated from the fan performance curve.
4. Outlet total temperature ($T_{T_{out}}$) is calculated.
5. The values for $P_{T_{out}}$ and $T_{T_{out}}$ are used for the stagnation inlet boundary condition at the axial fan outlet.
6. Calculate $\dot{m}_{out}$ from the CFD analysis (for the present iteration).
7. If $\dot{m}_{out} < \dot{m}_{in}$, then TPR is increased for the next iteration, otherwise it is decreased.

Using a small under-relaxation for the calculation of $P_{T_{out}}$ and $T_{T_{out}}$, the mass flow rate at the outlet approaches the inlet value fairly quickly.

A CFD simulation was setup to test the BBAF model. In order to accomplish this, an inlet and outlet height needed to be selected. Since the effect of these values on overall system

performance (and in particular their optimums when the AF is paired with the CFF) is one of the primary goals of this research effort, they were unknown a priori. By selecting an inlet height, however, the outlet height can be approximated based upon the static pressure field and anticipated TPR. The procedure for this calculation is as follows:

1. Given the inlet height, $\dot{m}_{in}$ is known, and thus so is $\dot{m}_{out}$, as well as all other inlet values (from the previous airfoil-alone CFD calculation).
2. Using a guess for TPR, $P_{T_{out}}$ and η_c are calculated.
3. Next $T_{T_{out}}$, M_{out}, T_{out}, ρ_{out}, and a_{out} are calculated.
4. Finally, h_{out} is calculated.
5. In addition, the power input to the axial fan can be calculated using Eq. 13.

As a starting point for the CFD test case, an inlet height of 25.7" is used, taken from Ref. 4. Selecting a TPR of 1.3, the compression efficiency is determined from the plot in Fig. 21, which was supplied by NASA GRC and also given in Ref. 4. The estimate for the outlet height is then calculated as 18.2". Also, the calculated power input to the AF is 525 HP/ft.

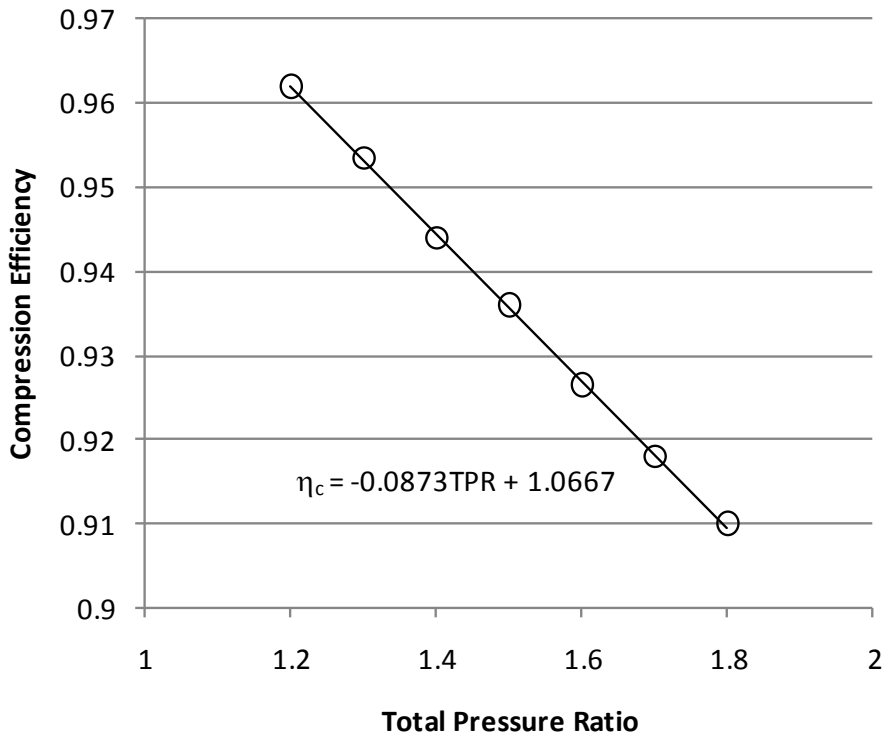

Fig. 21 Axial fan compression efficiency versus total pressure ratio (TPR)

One additional piece still needs to be added to the axial fan model, the efficiency penalty due to boundary layer ingestion (i.e. non-uniform inflow). This penalty is a function of both the magnitude of the total pressure deficit, as well as the height of the deficit region (i.e. boundary layer height). A convention is to wrap this into a parameter called distortion index. DI is defined

as the difference between the mass-averaged total pressure and the minimum total pressure divided by the average total pressure. DI gives a measure of the magnitude of the total pressure deficit relative to the average flow properties entering the fan or engine. It is commonly used to perform non-uniform inflow testing on jet engines, and is detailed in SAE Standard ARP1420.

Unfortunately, ARP1420 does not explicitly give a measurement for the location where the samples are to be taken. In the present case, the point of minimum total pressure is at the lower wall of the inlet. After performing a literature search, there is minimal published data relating DI (or non-uniform inflow in general) to fan efficiency penalty. As mentioned previously, Ref. 1 performed CFD calculations on an axial fan with inflow distortion and determined that at DI = 24% the efficiency penalty $\Delta\eta_c$ was approximately 6%. According to the authors in Ref. 1, $\Delta\eta_c$ is approximately linear in DI. One future goal of this work (beyond Phase I) will be to investigate the effect of inlet distortion on efficiency penalty. For the remainder of this work, however, it will be assumed that the above data is an acceptable representation of the current problem, hence $\Delta\eta_c = 0.25DI$.

In order to better correlate with the results in Ref. 1, $P_{T_{min}}$ will not be taken at the wall, but instead at a distance above the lower wall. For the initial BBAF test case, this value was essentially set arbitrarily as a small distance above the wall, since no indication was given in Ref. 1 as to its exact distance. Outputs from the CFD test case are shown in Figs. 22 and 23, demonstrating the use of the BBAF model to approximate the actual total pressure and total temperature rise through the real propulsor.

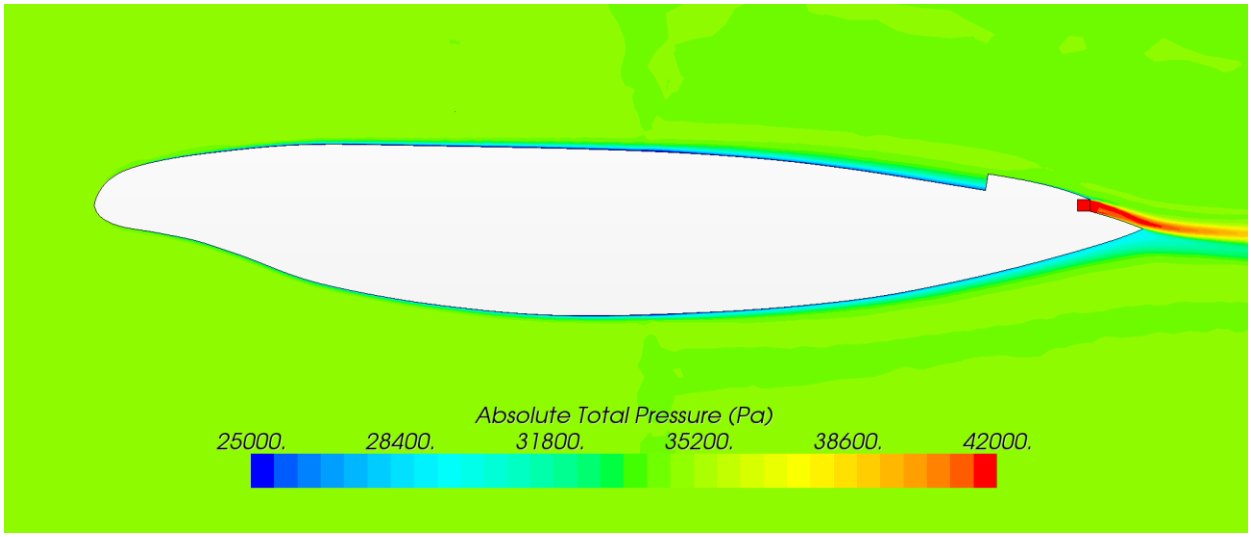

Fig. 22 Total pressure contours for BBAF model test case

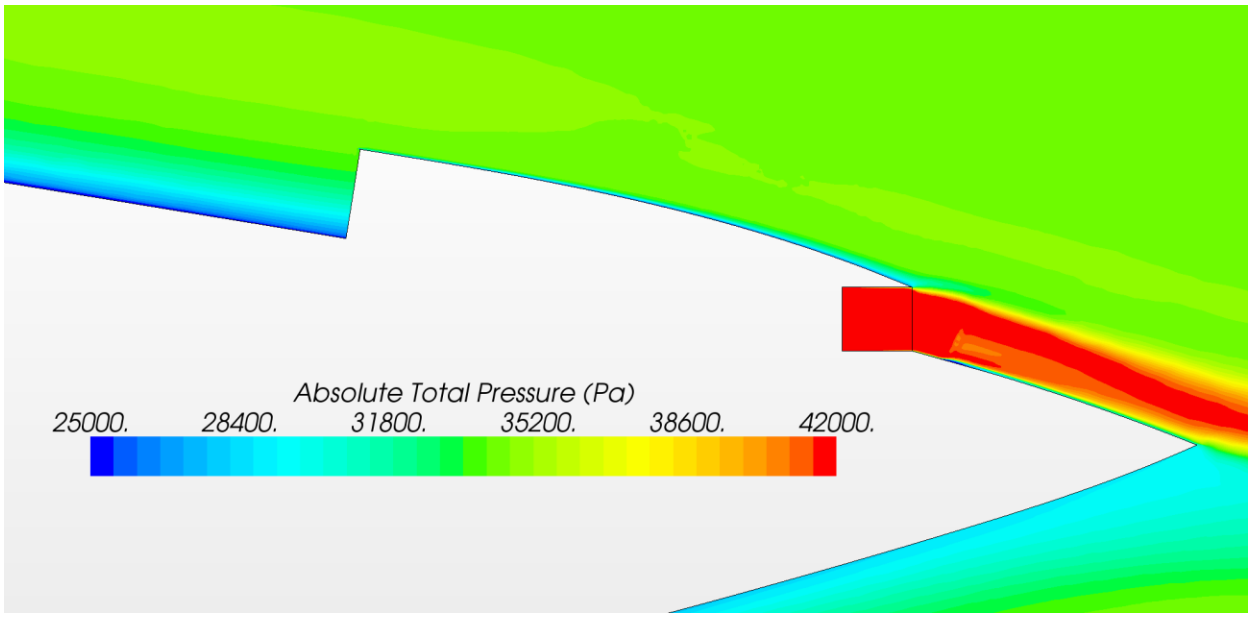

Fig. 23 Closeup of total pressure contours near BBAF

A uniform definition for the location of $P_{T_{min}}$ was needed, and a distance of 1.0 inch above the lower wall was selected. As already mentioned, the correlation of this distance (and the definition of DI in general) on axial fan performance is yet unknown; however, based on the prior work in this area the 1 inch distance seemed reasonable. An important outcome of the proposed Phase II effort will be to substantial these relations.

Figure 24 shows total pressure contours for the case where the axial fan inlet is 20" and $h_o=0.8h_i$. After several test cases, it was found that a short inlet duct (in addition to the short outlet duct) helped to stabilize the calculation. The selection of inlet height determined the mass flow rate into the fan, while the outlet height determined the total pressure ratio. In this case, with the outlet height set to 80% of the inlet height, the total pressure ratio is 1.19. The value for DI=0.14, which yields an efficiency penalty $\eta_{pen}=0.035$. Subtracting this from the calculated efficiency at TPR=1.19 yields $\eta_c=0.923$ (or 92.3%).

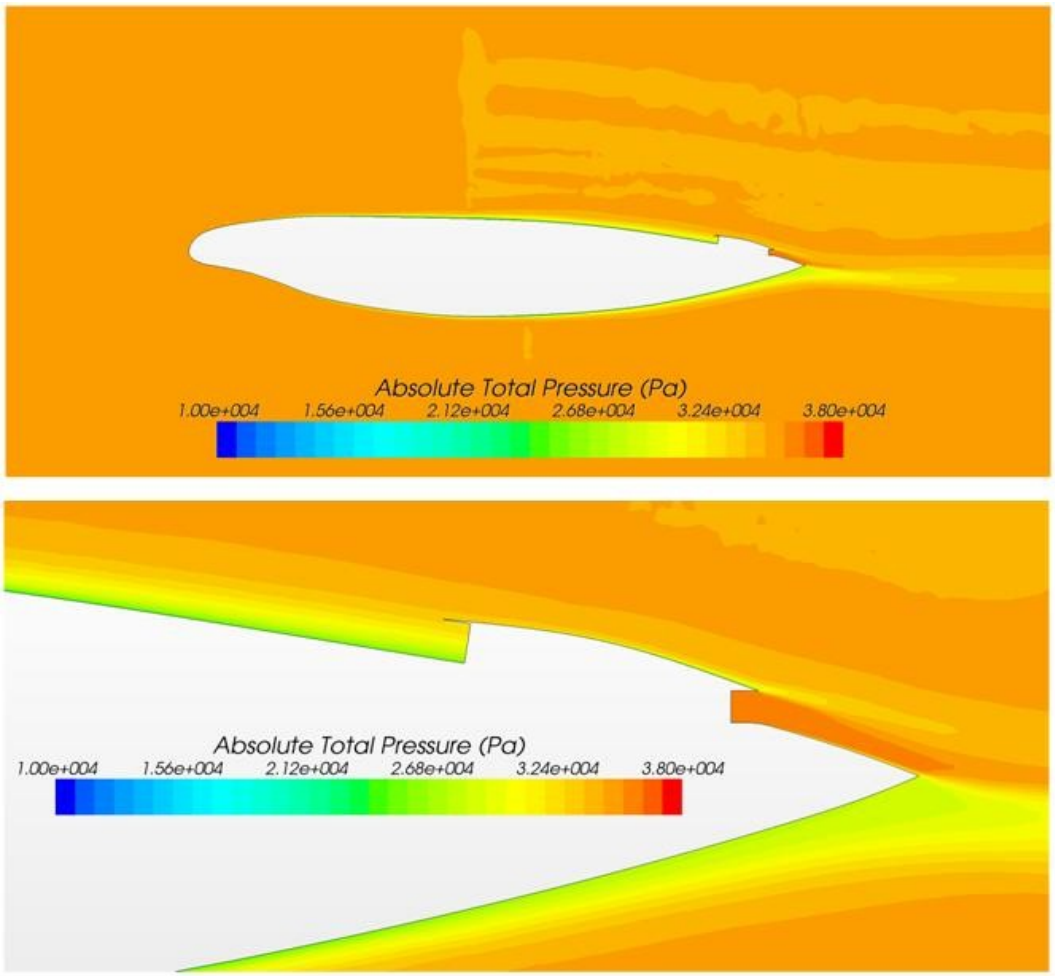

Fig. 24 Total pressure contours near BBAF: h_i = 20in, $h_o = 0.8h_i$

The effect of reducing the outlet height on the flow field is quite dramatic. As the outlet height reduces, for a fixed inlet height (and hence fixed mass flow rate), the exit Mach number must increase to compensate. As a result, for this configuration, there is a circulation control effect due to the trailing edge geometry (i.e. exhaust has downward component due to airfoil curvature). This in turn causes a shift in the shock location on the airfoil suction surface, as shown in Fig. 25. The result is an increase in the lift, but also in the drag. These cases correspond to an inlet height of 20".

Figure 26 shows a closeup of the Mach contours for h_i=35in, h_o=0.8h_i. Of particular note in the figure is the expansion fan near the outlet, which causes a rapid acceleration of the flow, here to M = 1.4, and then is immediately followed by a normal shock. This is an effect of the airfoil curvature here, and would need to be addressed in future designs to minimize drag, since it can result in shock-induced flow separation. Figure 27 shows the streamlines for this case. Of particular note is the smoothness of the flow around the propulsor, a result of proper selection of the mass flow rate and contouring of the axial fan top shroud.

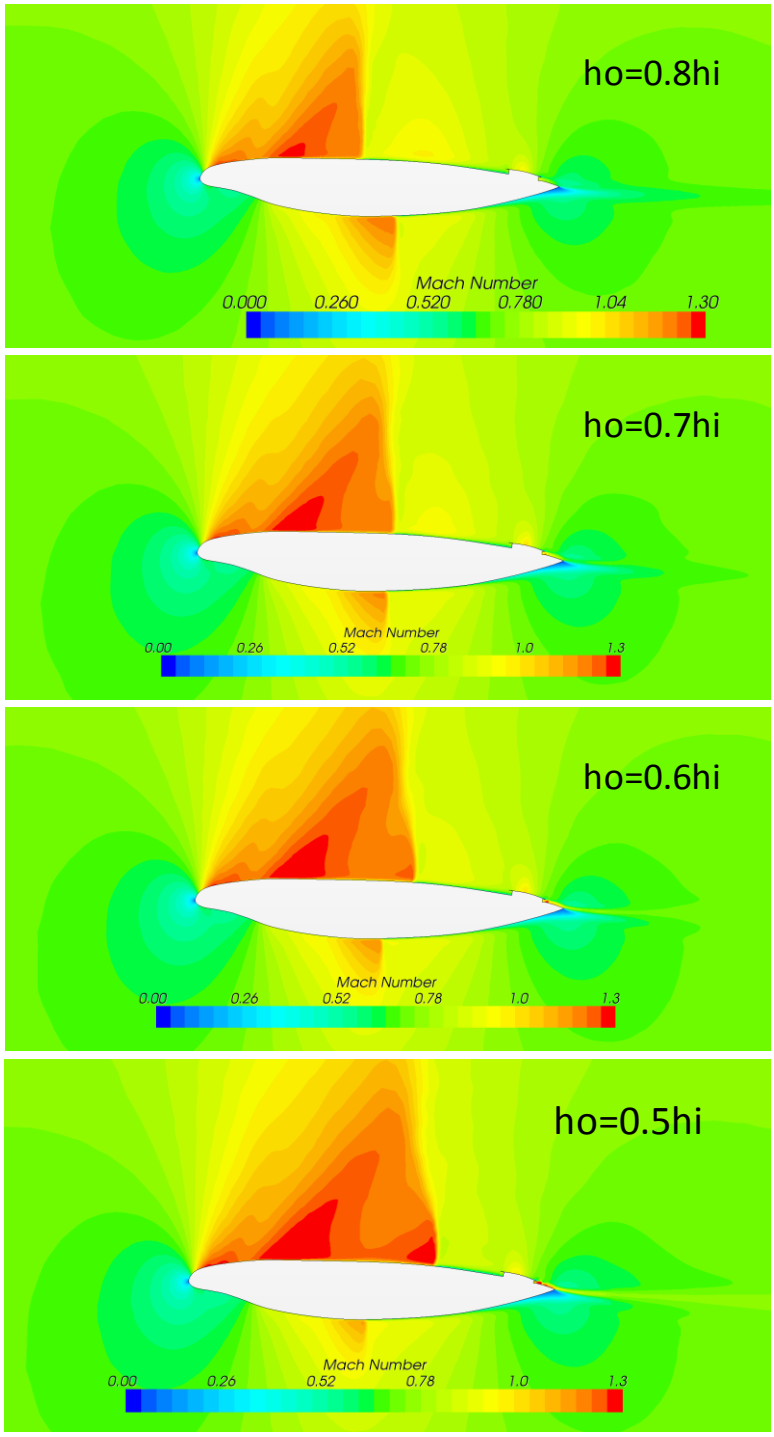

Fig. 25 Mach contours: h_i = 20in

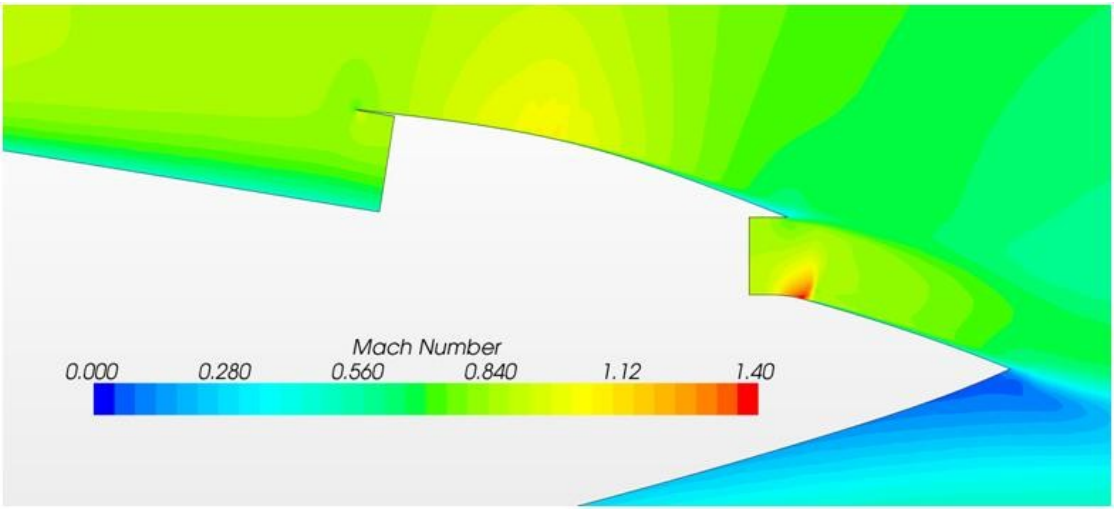

Fig. 26 Mach contours: $h_i = 35in$, $h_o = 0.8h_i$

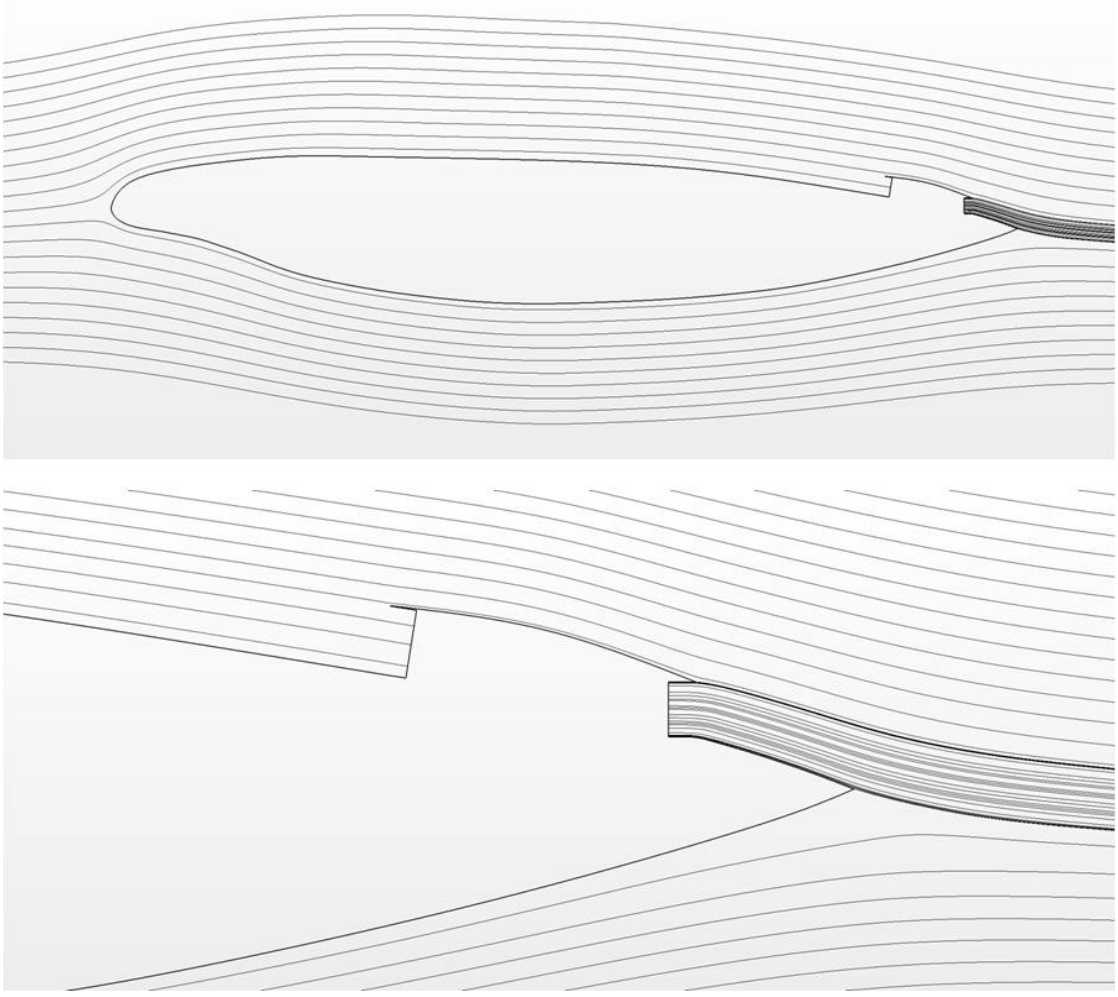

Fig. 27 Streamlines: $h_i = 35in$, $h_o = 0.8h_i$

Figures 28-34 present the key numerical data for the BBAF CFD runs. Calculations were performed for 16 configurations: inlet height = 20", 25", 30", and 35"; outlet/inlet height = 0.5, 0.6, 0.7, and 0.8. Several interesting trends can be seen in the data. The first is that as inlet height increases, the efficiency penalty (i.e. DI) also increases. This is a result of the method of calculation of DI, which relies solely on the location where the minimum total pressure is calculated and the average total pressure over the entire inlet. For each case the minimum values are approximately the same; however, as the inlet height increases, so does the average total pressure, since the flow further from the airfoil surface is closer to the freestream value. As a result, the larger inlet height results in lower compression efficiency (as seen in Fig. 32). Not surprising, the largest inlet height also has the highest power consumption (due to the larger mass flow rate), and as such has the lowest values for $C_{D(net)}$ and highest values for $C_{L(net)}$.

A typical measure of the overall performance of an aircraft is lift to drag ratio. Instead, the data here are plotted as net drag coefficient to net lift coefficient ratio in Figs. 33 and 34 versus TPR and Power, respectively. This value lends itself better to the present case, since as power increases, the curves trend toward zero. As will be seen in the cases where the cross-flow fan is included, this value can be negative, which indicates a net thrust force on the airfoil. Nonetheless, Fig. 33 shows that as the inlet height increases, $C_{D(net)}/C_{L(net)}$ reduces, with the effect particularly noticeable at lower TPR. Interestingly, however, if the data is plotted against power, with the exception of the one high power (and high TPR) case at 35", all of the plots lie almost on top of one another. Thus from an energy perspective (i.e. to propel the airfoil at a given speed), the effect of the axial fan inlet size is small. Of course, this result assumes that the current efficiency penalty modeling is realistic, since, as shown in Fig. 31, the highest penalty corresponds to the largest inlet height. A more complete understanding of the effect of boundary layer ingestion into the axial fan will allow a full evaluation of these trends.

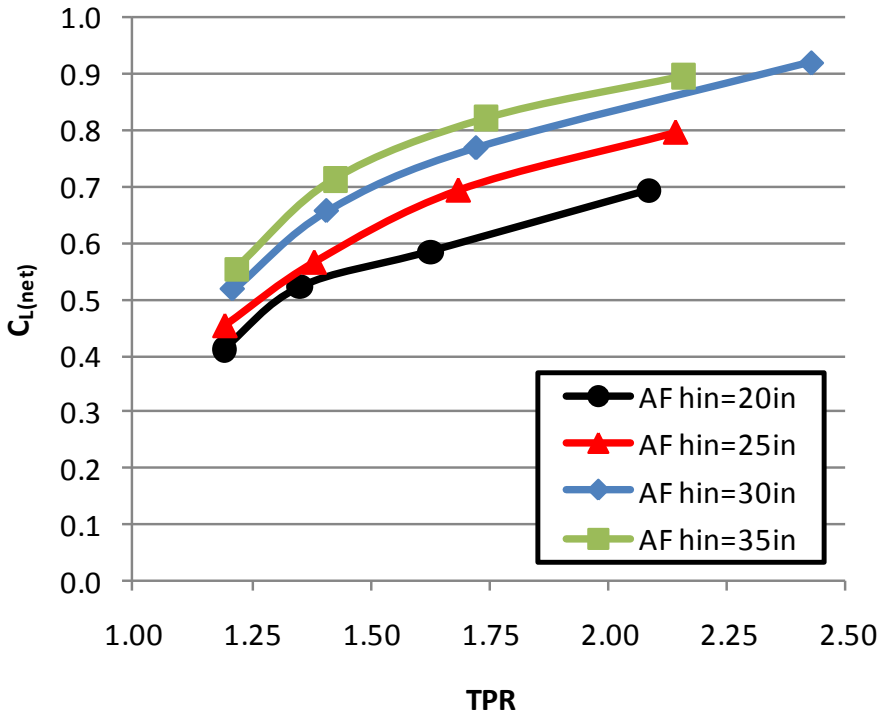

Fig. 28 Black-Box Axial Fan Runs: $C_{L(Net)}$ Vs. TPR

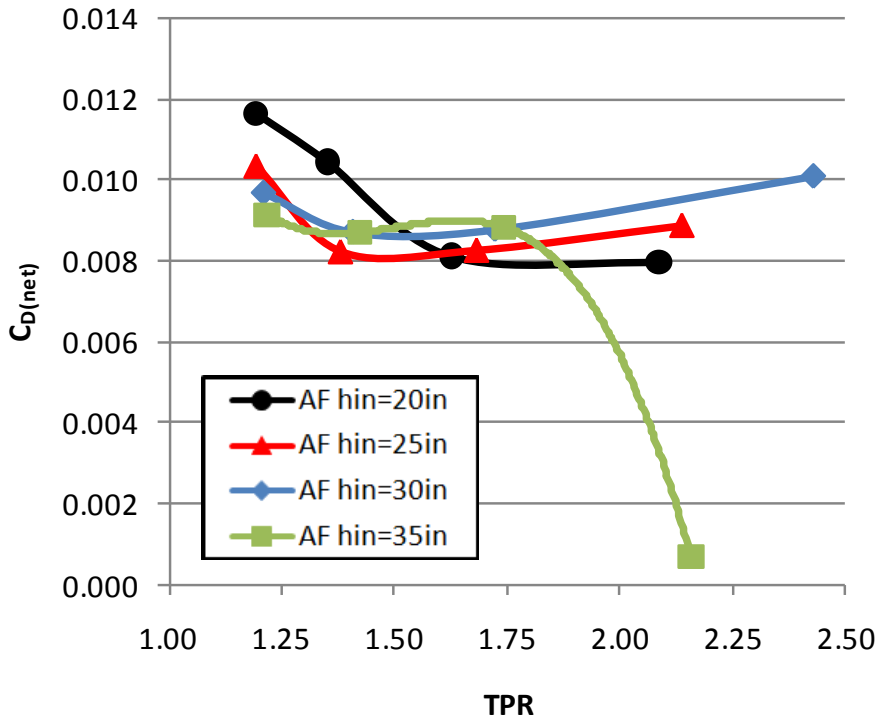

Fig. 29 Black-Box Axial Fan Runs: $C_{D(Net)}$ Vs. TPR

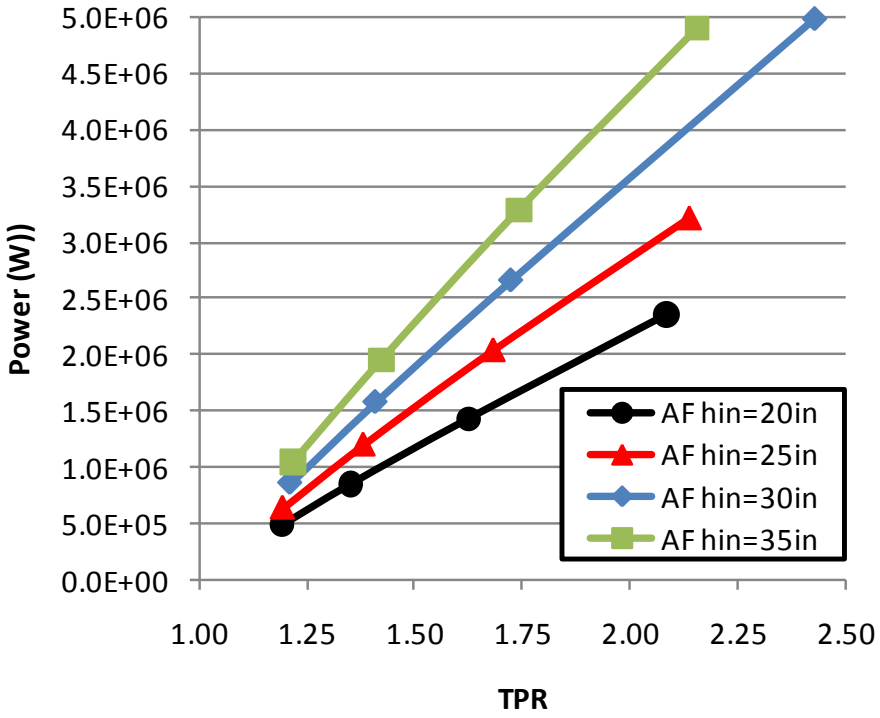

Fig. 30 Black-Box Axial Fan Runs: Power Vs. TPR

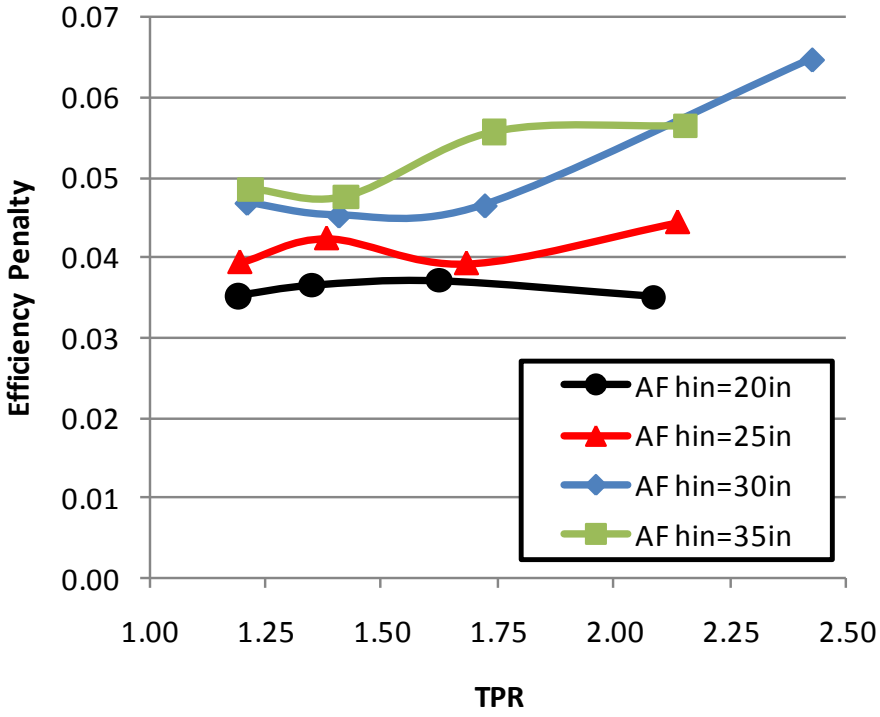

Fig. 31 Black-Box Axial Fan Runs: Efficiency Penalty Vs. TPR

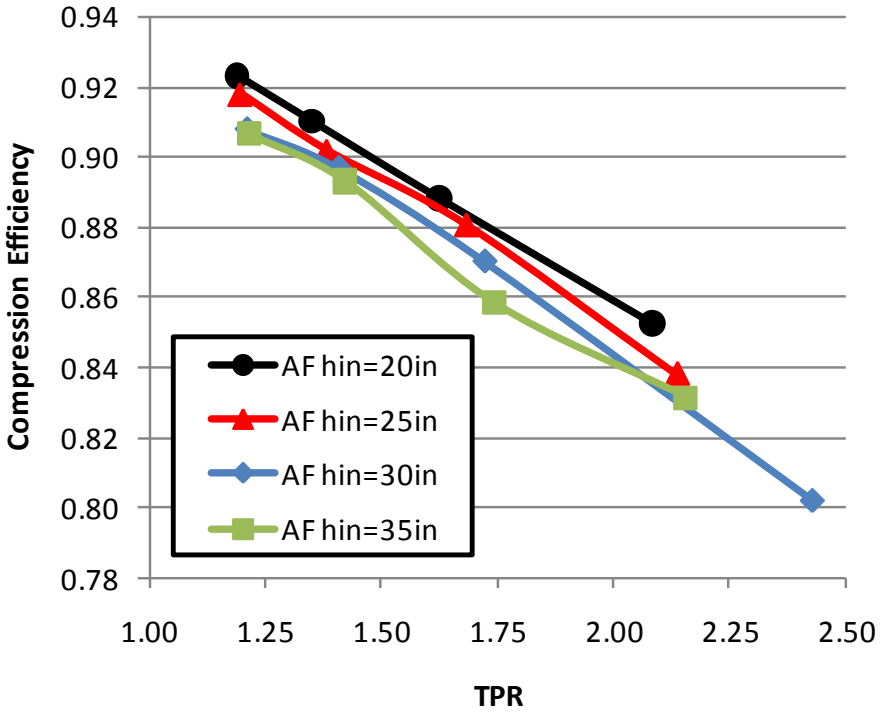

Fig. 32 Black-Box Axial Fan Runs: Compression Efficiency Vs. TPR

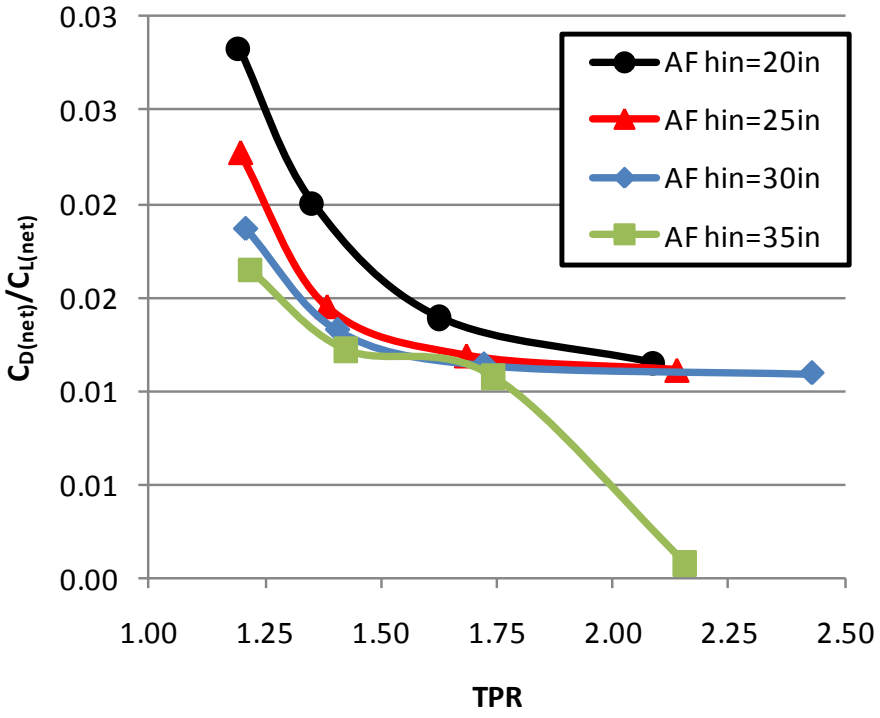

Fig. 33 Black-Box Axial Fan Runs: $C_{D(Net)}$ / $C_{L(Net)}$ Vs. TPR

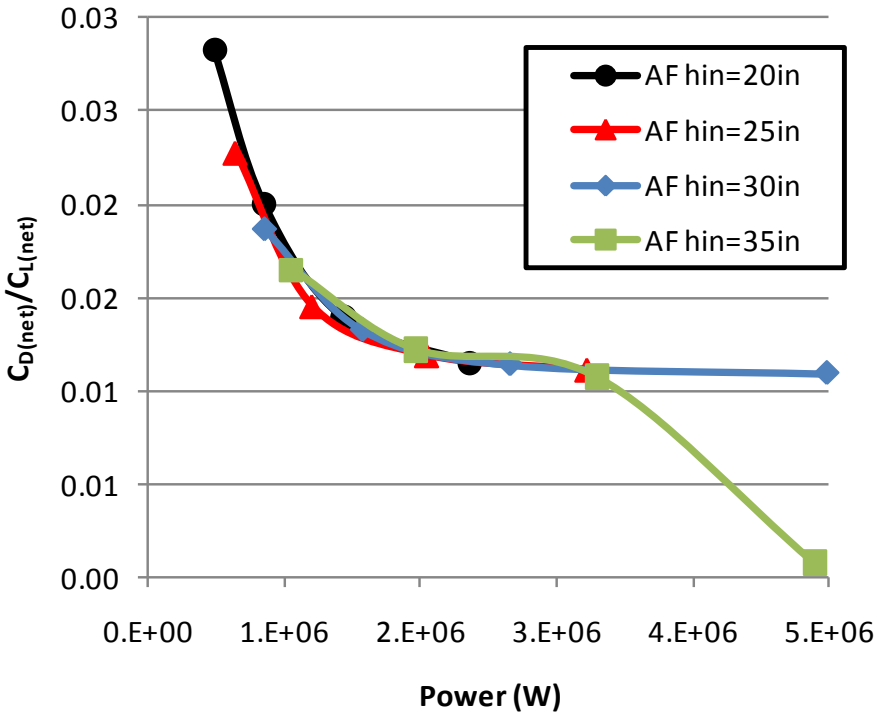

Fig. 34 Black-Box Axial Fan Runs: $C_{D(Net)}$ / $C_{L(Net)}$ Vs. Power

Combined Black-Box Axial Fan and Cross-Flow Fan Model

Next the two black-box models were combined into a single CFD calculation. The same baseline geometry was used (i.e. the mid-span airfoil section for the N3-X BWB). Figure 35 shows the grid around the airfoil, while Fig. 36 shows close-ups near the inlets and outlets. The grid here contains 87,000 cells. This configuration consists of an axial fan inlet (large inlet) sitting directly on top of a cross-flow fan inlet (small inlet). The goal is to ingest the worst portion of the non-uniform boundary layer flow into the cross-flow fan, allowing the axial fan to "see" cleaner flow. From an analytical perspective, the goal here is to reduce the distortion index at the axial fan inlet, thus increasing the fan performance. There is an inherent tradeoff here, since the cross-flow fan has lower compression efficiency than the axial fan; however, in order to be effective, the CFF inlet need only ingest 4-6" of the boundary layer, thus contributing to only a small portion of the overall power consumption.

Cases were run across a range of inlet and outlet heights in order to assess the capabilities of the CFD models, as well as evaluate the power requirements of this configuration. Although the 2D flow field will inherently be different than for the 3D case, the trends should remain intact. In addition, the development of 2D simulation techniques offers an excellent option for future design efforts.

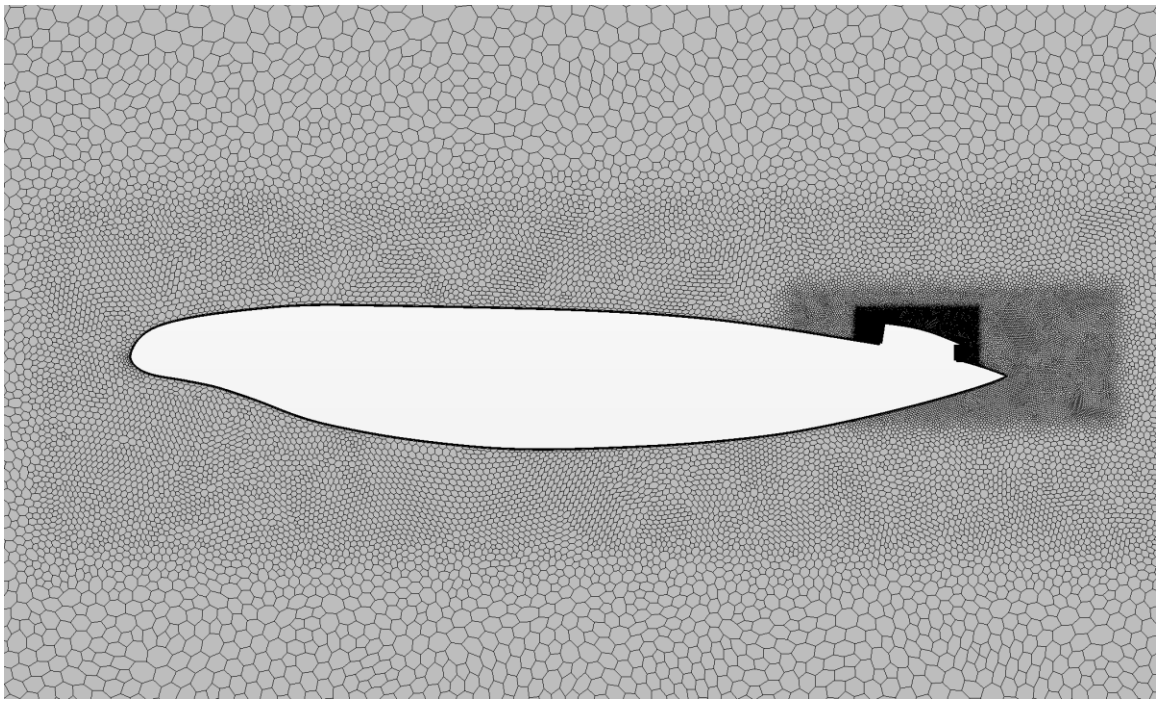

Fig. 35 Black-Box AF/CFF Grid: Complete Airfoil

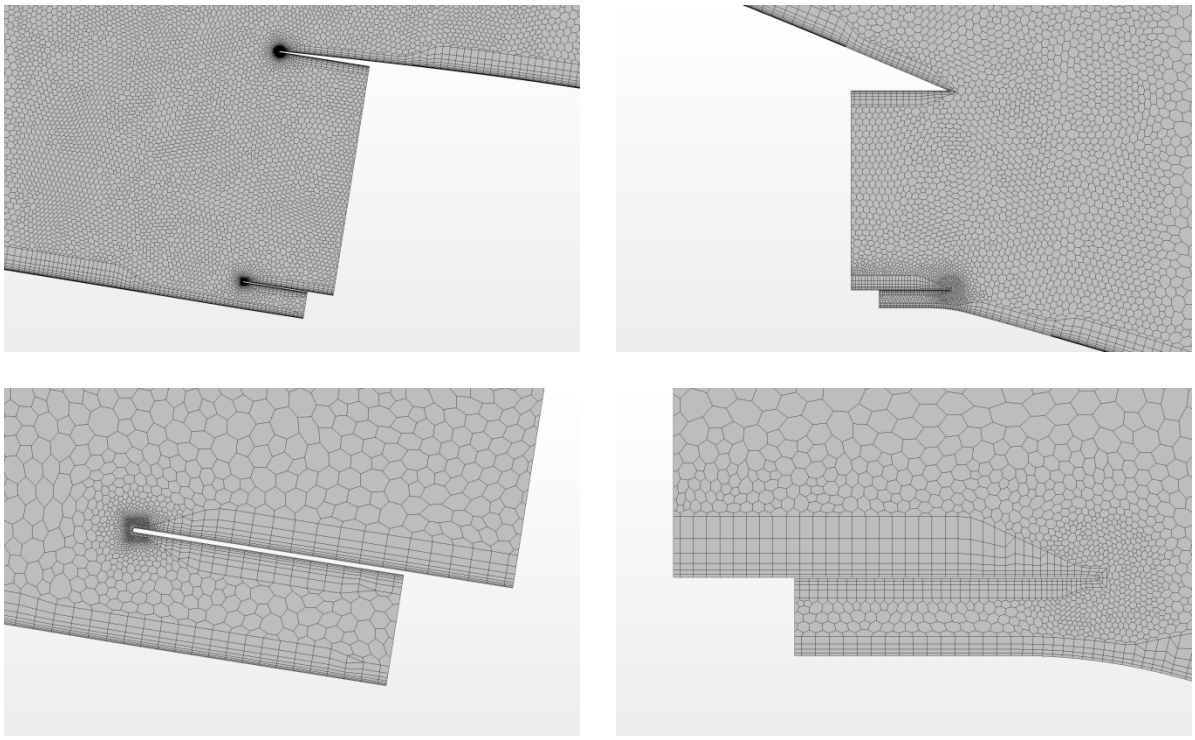

Fig. 36 Black-Box AF/CFF Grid: Closeup near AF and CFF inlets and outlets

Figure 37 shows total pressure contours corresponding to $h_{i(CFF)}$=6in, $h_{o(CFF)}$=3.9in, $h_{i(AF)}$=35in, and $h_{o(AF)}$=0.8$h_{i(AF)}$. Cases were run for two different CFF inlet heights: 4" and 6". Figures 38 and 39 show close-ups near the inlets and outlets for the 6" inlet case. The clean, uninterrupted transition between the CFF and AF inlets is clear in Fig. 38. Essentially, the AF inlet ingests the boundary layer minus the bottom 6", which is ingested into the CFF. At the outlet, the CFF exhausts the air at a lower total pressure than the axial fan, in this case just below the freestream value. It was originally hypothesized that it would be necessary to increase the total pressure through the CFF to at least the freestream value; however, this does not seem to be a requirement, thus saving power. If one wishes to increase the CFF outlet total pressure, then a reduction in the outlet height is necessary, as shown in Figs. 40 and 41.

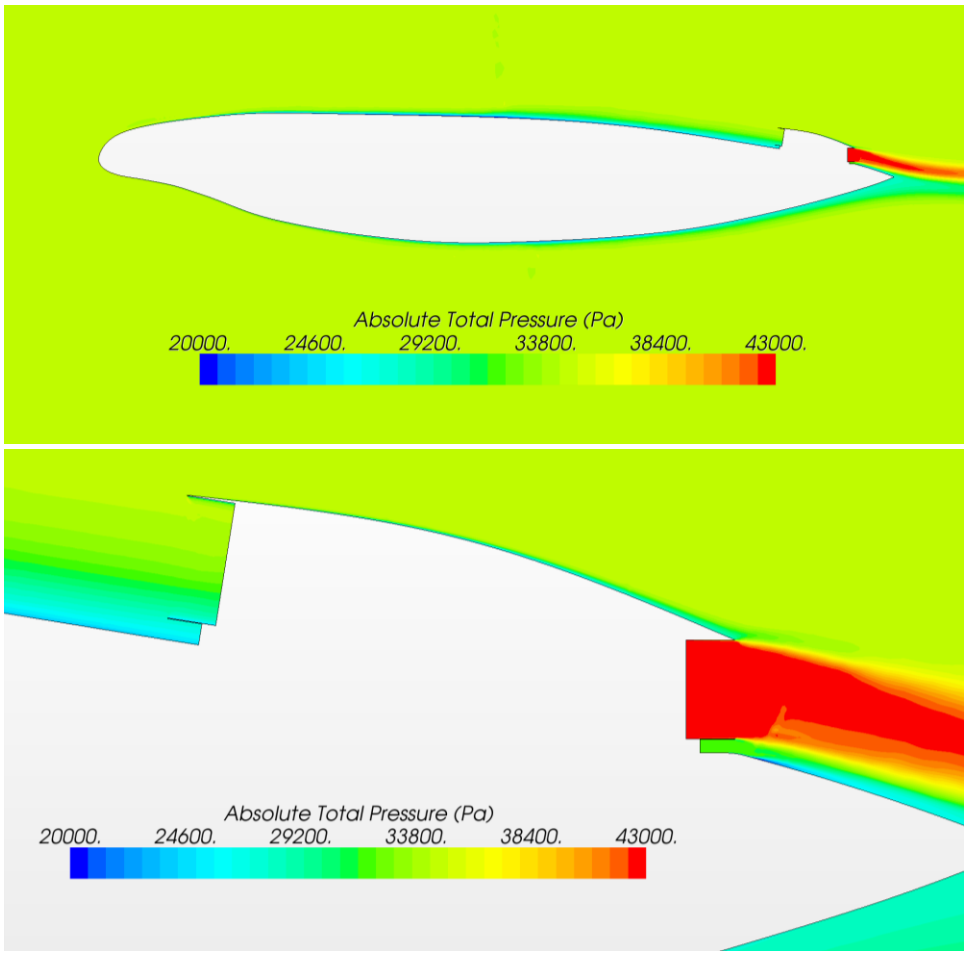

Fig. 37 BB AF/CFF: Total Pressure – $h_{i(CFF)}$=6in, $h_{o(CFF)}$=3.9in, $h_{i(AF)}$=35in, $h_{o(AF)}$=0.8$h_{i(AF)}$

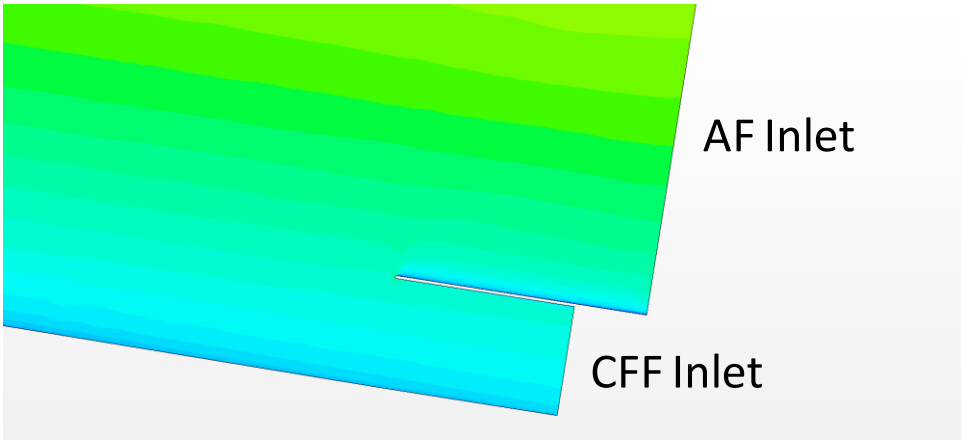

Fig. 38 Closeup near AF and CFF inlet – $h_{i(CFF)}$=6in, $h_{o(CFF)}$=3.9in, $h_{i(AF)}$=35in, $h_{o(AF)}$=0.8$h_{i(AF)}$

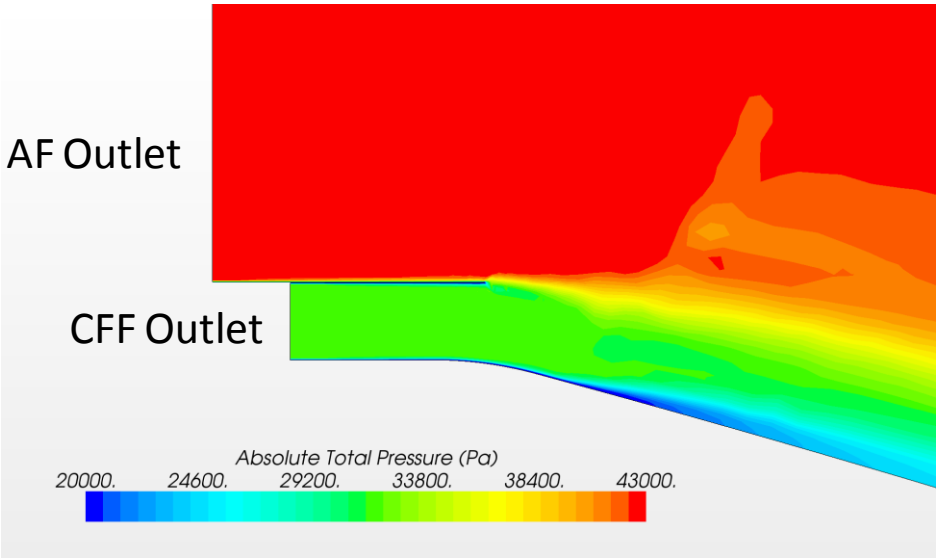

Fig. 39 Closeup near AF and CFF outlet – $h_{i(CFF)}$=6in, $h_{o(CFF)}$=3.9in, $h_{i(AF)}$=35in, $h_{o(AF)}$=0.8$h_{i(AF)}$

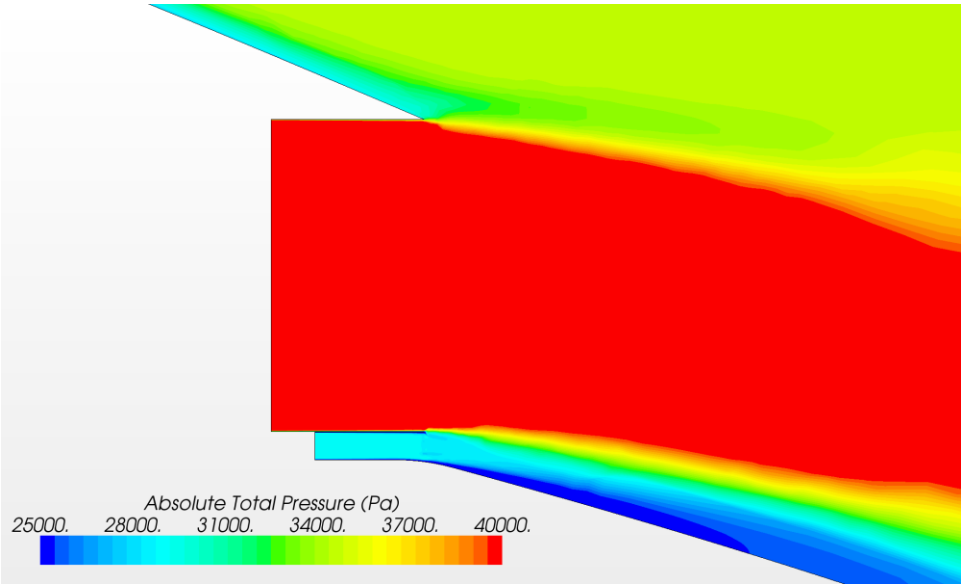

Fig. 40 Closeup near AF and CFF outlet – $h_{i(CFF)}$=4in, $h_{o(CFF)}$=2.5in, $h_{i(AF)}$=35in, $h_{o(AF)}$=0.8$h_{i(AF)}$

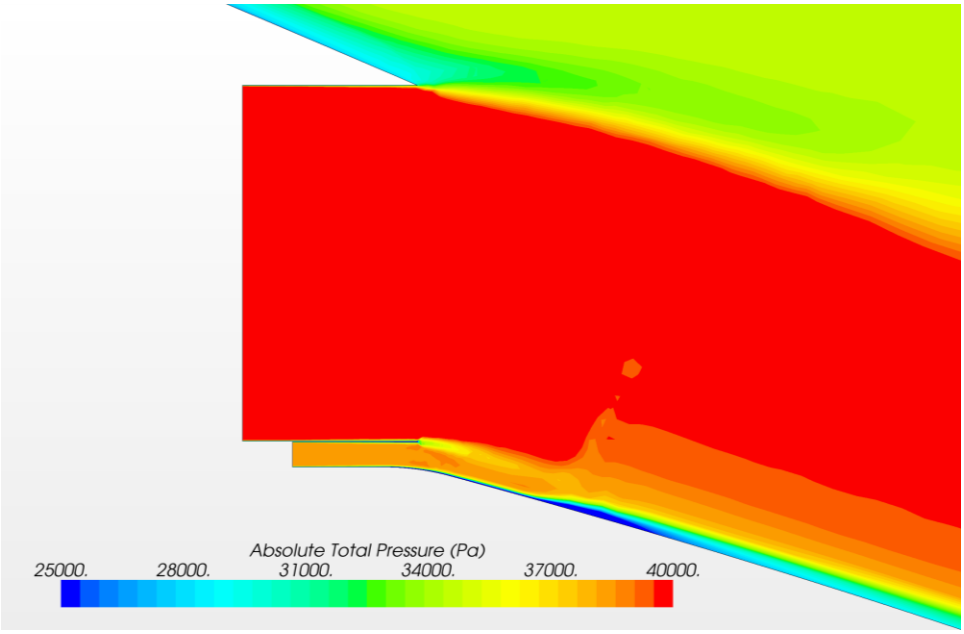

Fig. 41 Closeup near AF and CFF outlet – $h_{i(CFF)}$=4in, $h_{o(CFF)}$=2in, $h_{i(AF)}$=35in, $h_{o(CFF)}$=0.8h_i

As mentioned previously, there is a large effect from the propulsor, both on the suction side, as well as the exhaust side, on the overall airfoil aerodynamics. Figure 42 shows the effect of changing the axial fan inlet and outlet heights, while maintaining a constant CFF geometry. The effect here is rather dramatic, particularly for the high exhaust velocity case (i.e. small AF outlet). Traditional aircraft analyses tend to separate the design of the airframe from the propulsors as much as possible, with the majority of the coupling coming in the form of interference drag, scrubbing drag, or similar parameters. In the present case, however, the use of embedded, distributed propulsion necessitates a design process whereby the airframe and engines are thought of not as separate entities, but a highly coupled system. Figures 43-45 show Mach contours and streamlines for these cases, and again reaffirm the coupled nature of this design. Unlike convention aircraft designs, one cannot assume that the inclusion of the propulsor into the airframe will have a minimal impact on the external aerodynamics. In fact, the difference can be dramatic even for relatively small changes in the airfoil geometry, fan location, fan inlet and outlet sizing, and propulsor performance. Furthermore, each of these parameters has an effect on the others, again requiring a simultaneous optimization of both the airframe and propulsors for a given mission.

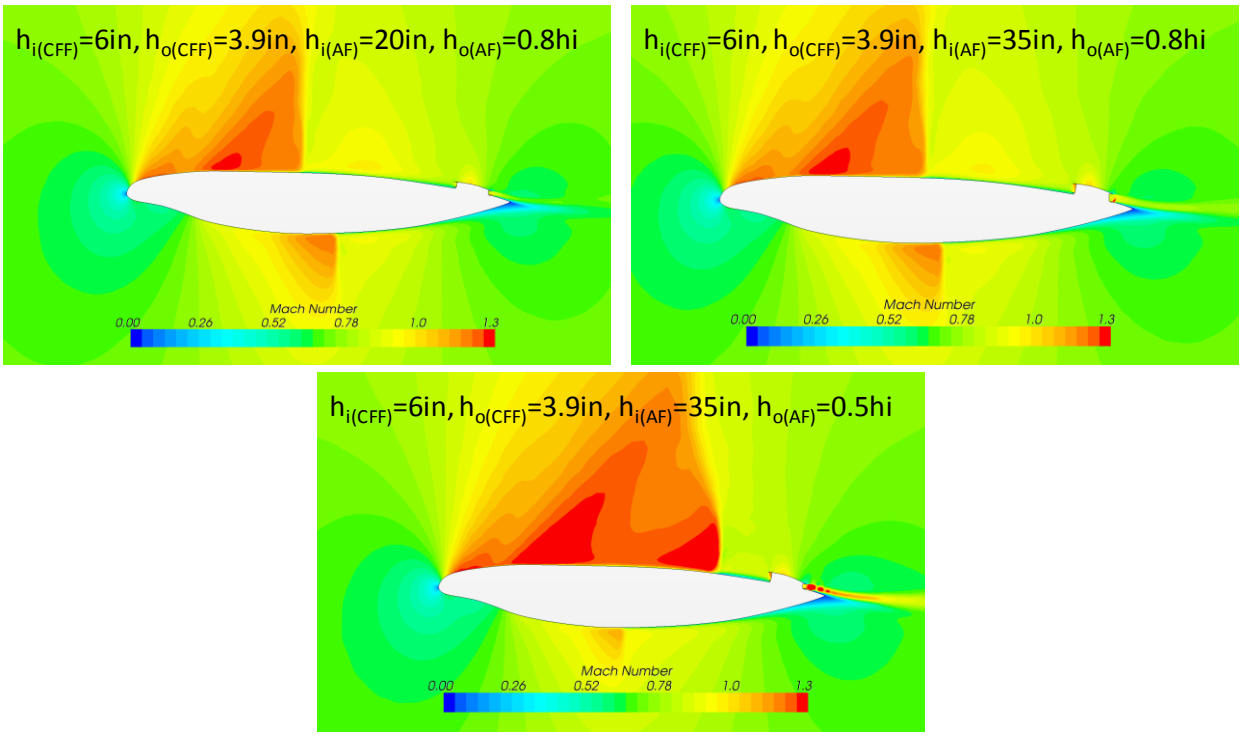

Fig. 42 Total pressure contours showing movement of shock

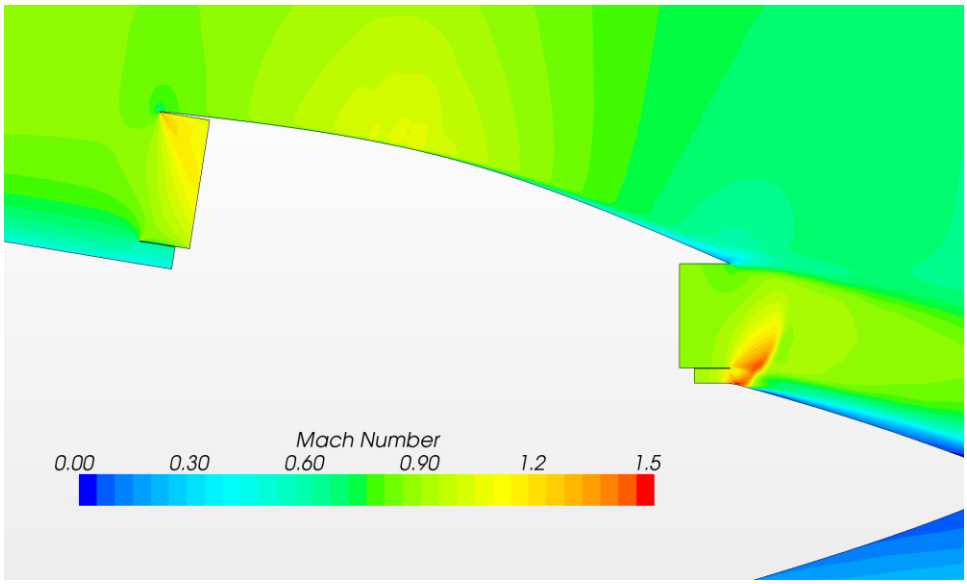

Fig. 43 Mach Contours – $h_{i(CFF)}$=6in, $h_{o(CFF)}$=3.9in, $h_{i(AF)}$=35in, $h_{o(AF)}$=0.8$h_{i(AF)}$

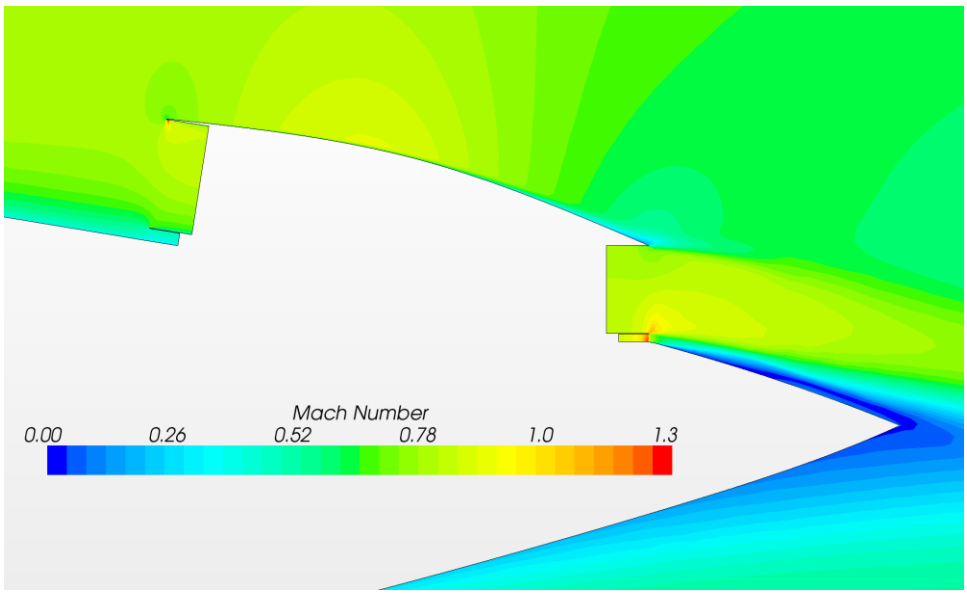

Fig. 44 Mach Contours – $h_{i(CFF)}$=4in, $h_{o(CFF)}$=2.5in, $h_{i(AF)}$=35in, $h_{o(AF)}$=0.8$h_{i(AF)}$

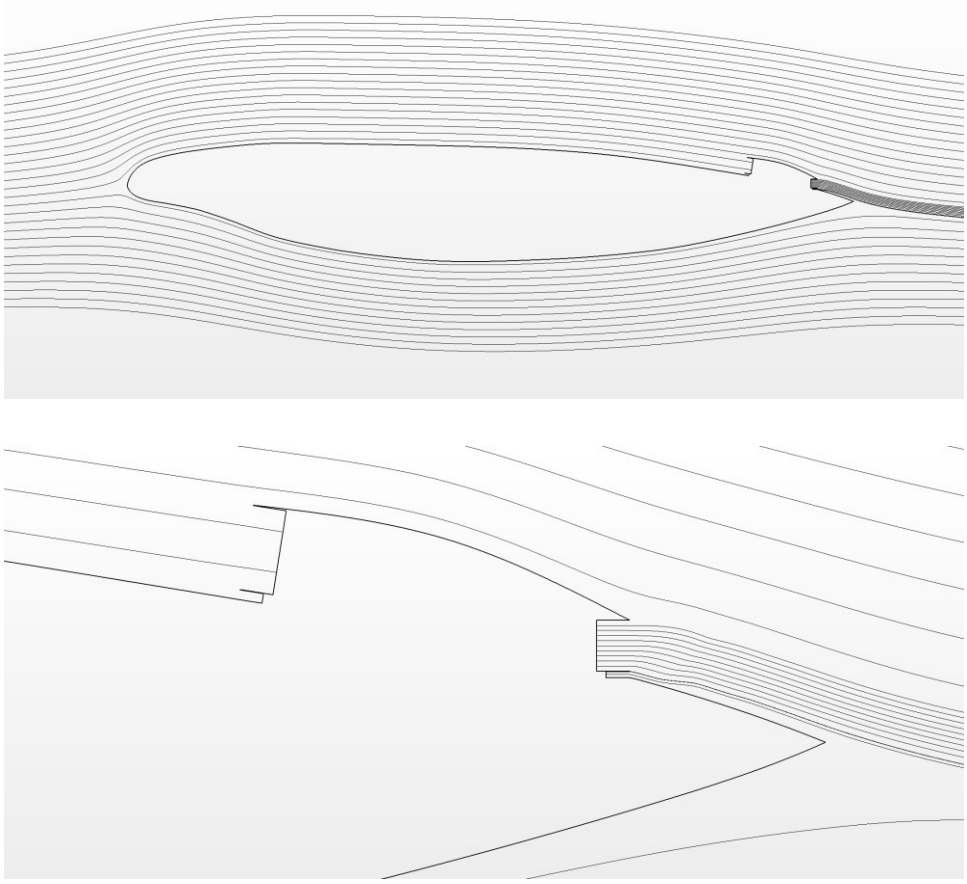

Fig. 45 Streamlines – $h_{i(CFF)}$=4in, $h_{o(CFF)}$=2.5in, $h_{i(AF)}$=35in, $h_{o(AF)}$=0.8$h_{i(AF)}$

Figures 46-51 present the numerical results from the AF/CFF CFD cases alongside the comparable results from the axial fan alone case. To facilitate direct comparisons, all cases were run at 0^o AOA. The first set, Fig. 46, gives the net lift and drag coefficients versus TPR. As expected, in general, as TPR increases, $C_{L(net)}$ increases and $C_{D(net)}$ decreases. Also, several of the AF/CFF cases have negative values for $C_{D(net)}$, indicating a net thrust force on the airfoil.

The effect of TPR on both AF and CFF efficiency, as well as the AF efficiency penalty for each case, is given in Fig. 47. It is interesting to note that the reduction in efficiency penalty is greatest at low TPR. Thus the greatest benefit from utilizing the CFF propulsor is also at low TPR. This is fortunate, since an optimized design would inherently utilize a low TPR axial fan (i.e. for higher AF efficiency). The challenge, of course, is the design of such a fan, since lower TPR fans tend to have greater sensitivity to inlet flow distortion, not only in terms of lost performance, but also with increases in mechanical vibration, leading to potential structural challenges (e.g. fatigue).

Figure 48 shows the relation between power and TPR. Clearly as TPR increases, the AF power requirement also increases. Of interest here, though, is the magnitude of the CFF power compared with that for the axial fan. The end goal of this work is to demonstrate the benefit of utilizing a small amount of power to drive a CFF propulsor in order to improve the overall performance of the complete system. Looking only at the lowest TPR case, the ratio of CFF power to AF power for the 6" CFF inlet case is 0.1. By contrast, the same ratio for the 12" diameter, 4" CFF inlet case is only 0.024. Thus the axial fan here is consuming about 42 times more power than the CFF. For a relatively small amount of power, then, the CFF system reduces the AF efficiency penalty from 4.9% to 2.6%, an improvement of 2.3%.

The performance benefit is further accentuated in Fig. 49, which plots $C_{D(net)}/C_{L(net)}$ as a function of total Power input (i.e. AF power + CFF power). Clearly, for a given amount of power, the graph shows a decrease in $C_{D(net)}/C_{L(net)}$ for the cases where the CFF is present. For example, the lowest TPR case with a 6" CFF inlet has a value for $C_{D(net)}/C_{L(net)}$ of 0.004. The comparable AF case (with the same 35" AF inlet) has a value of 0.013 for $C_{D(net)}/C_{L(net)}$ at the same power. The important point here is that, since the D/L value is lower for the AF/CFF case (i.e. the effective L/D is higher) it represents a more efficient design in terms of overall energy usage.

Figures 50-52 graph similar data to that shown in Figs. 46-48, but with the ratio of AF outlet to inlet height fixed at 0.8. The trends are similar to those seen in the first set of graphs, and are presented here for completeness.

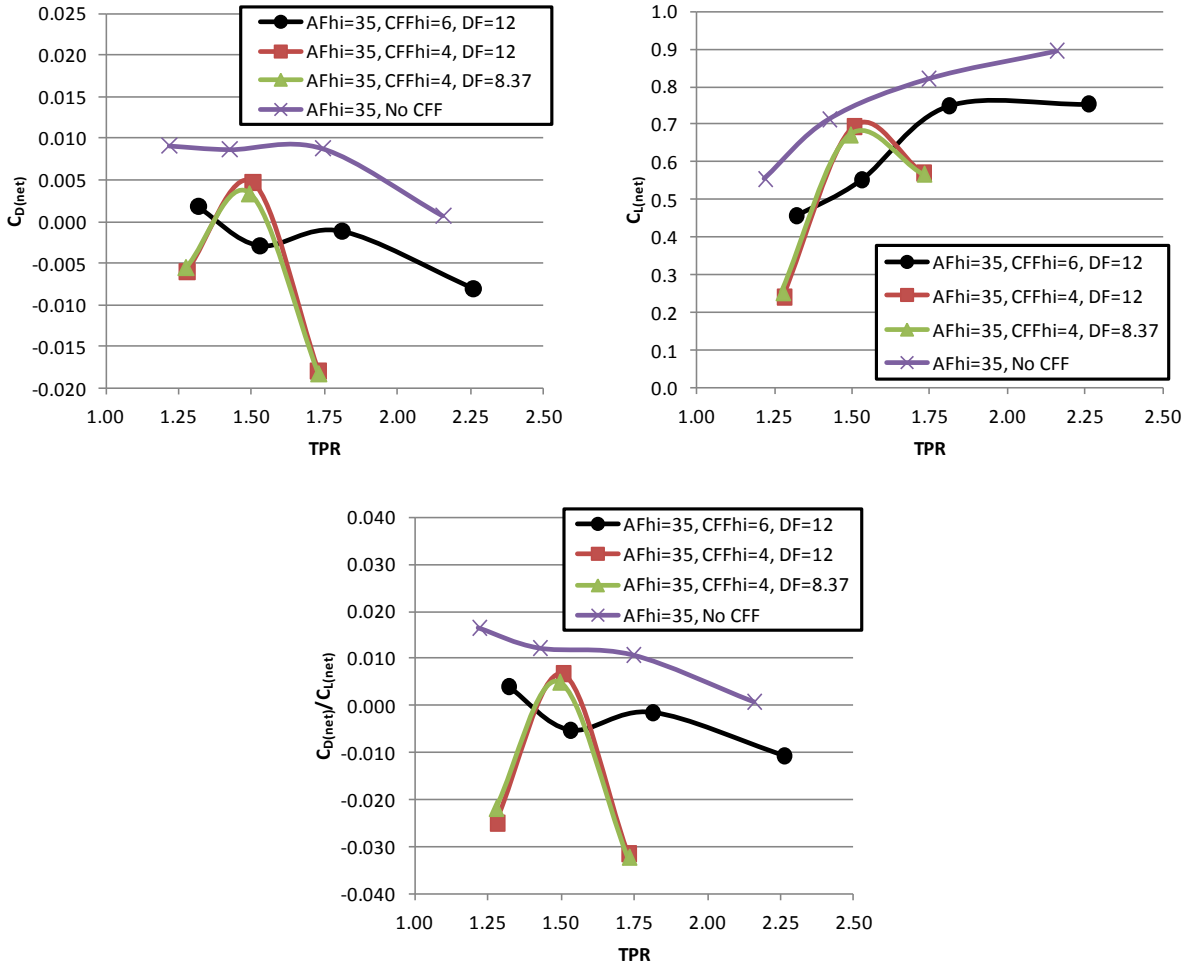

Fig. 46 BB AF/CFF: Net Lift and Net Drag Coefficients Vs. TPR for $h_{i(AF)}$ = 35in

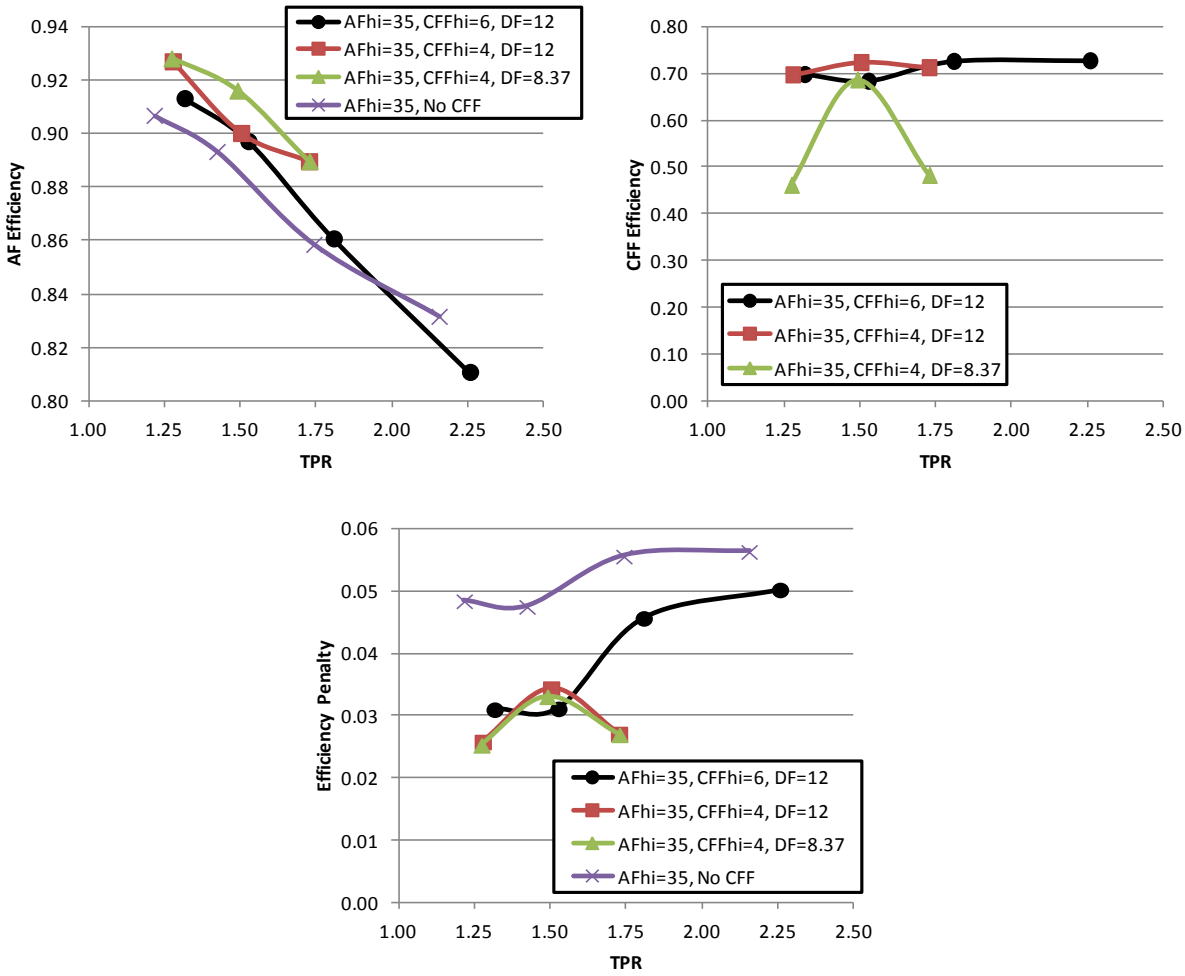

Fig. 47 BB AF/CFF: Efficiency and Efficiency Penalty Vs. TPR for $h_{i(AF)} = 35in$

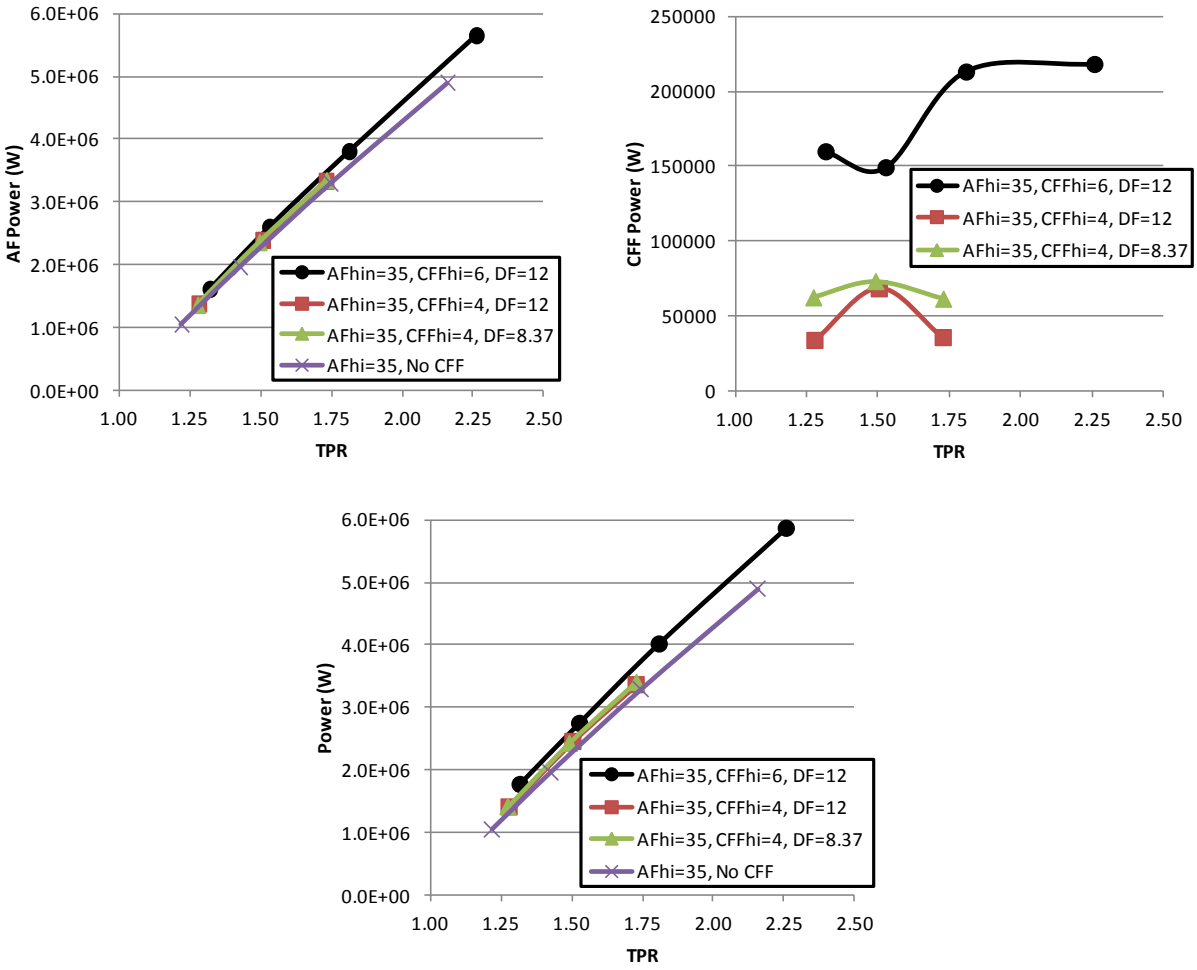

Fig. 48 BB AF/CFF: Power Vs. TPR for $h_{i(AF)} = 35in$

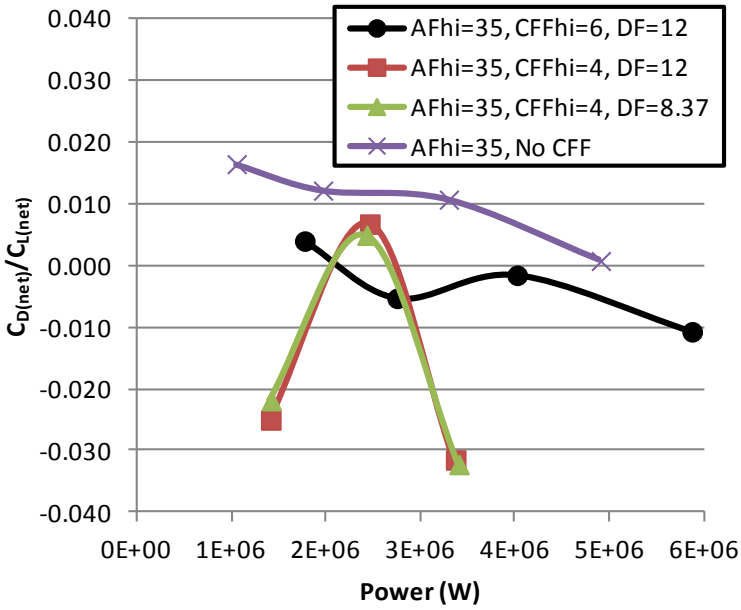

Fig. 49 BB AF/CFF: Net Lift to Net Drag Ratio Vs. Power for $h_{i(AF)} = 35in$

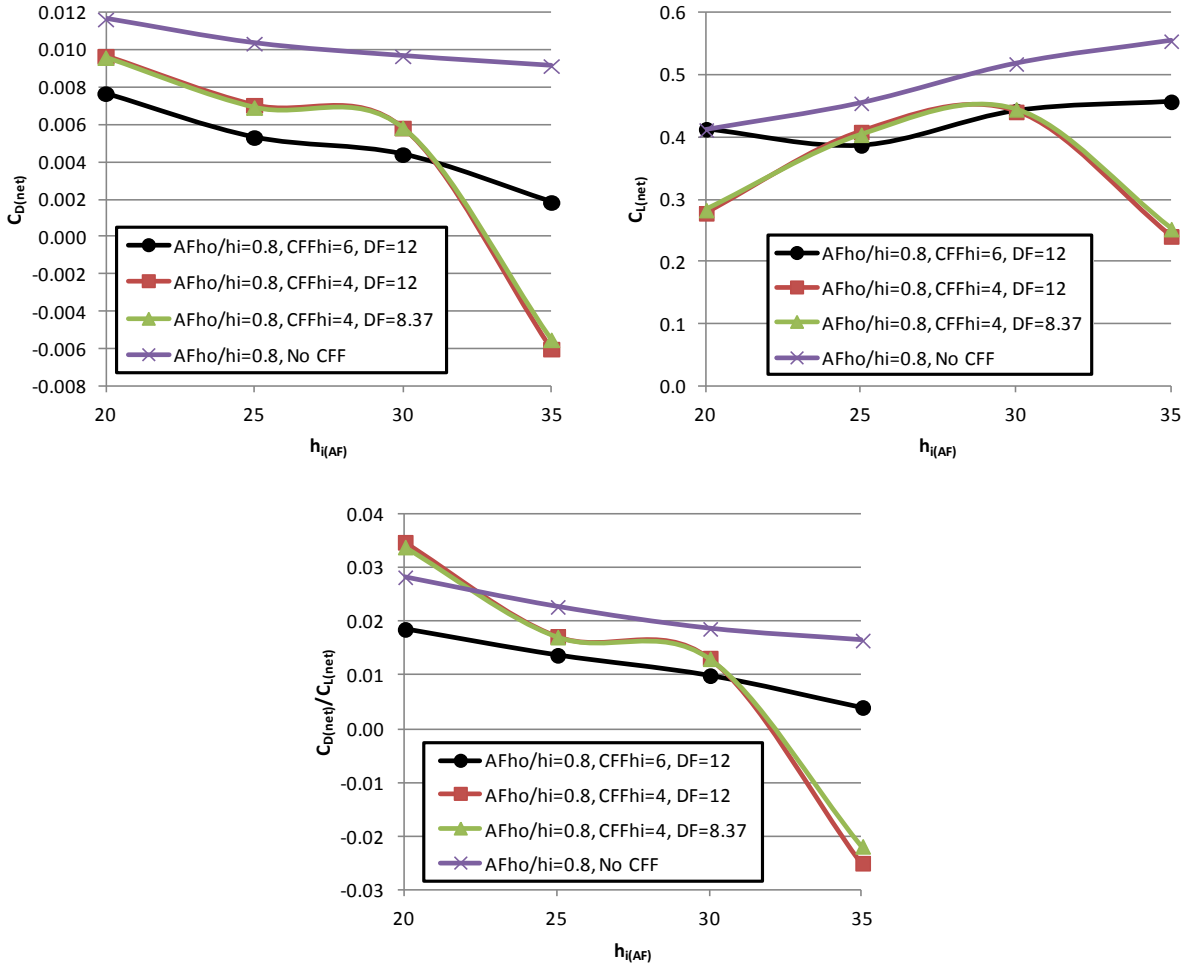

Fig. 50 BB AF/CFF: Net Lift and Net Drag Coefficients Vs. $h_{i(AF)}$ for $h_{o(AF)}=0.8h_{i(AF)}$

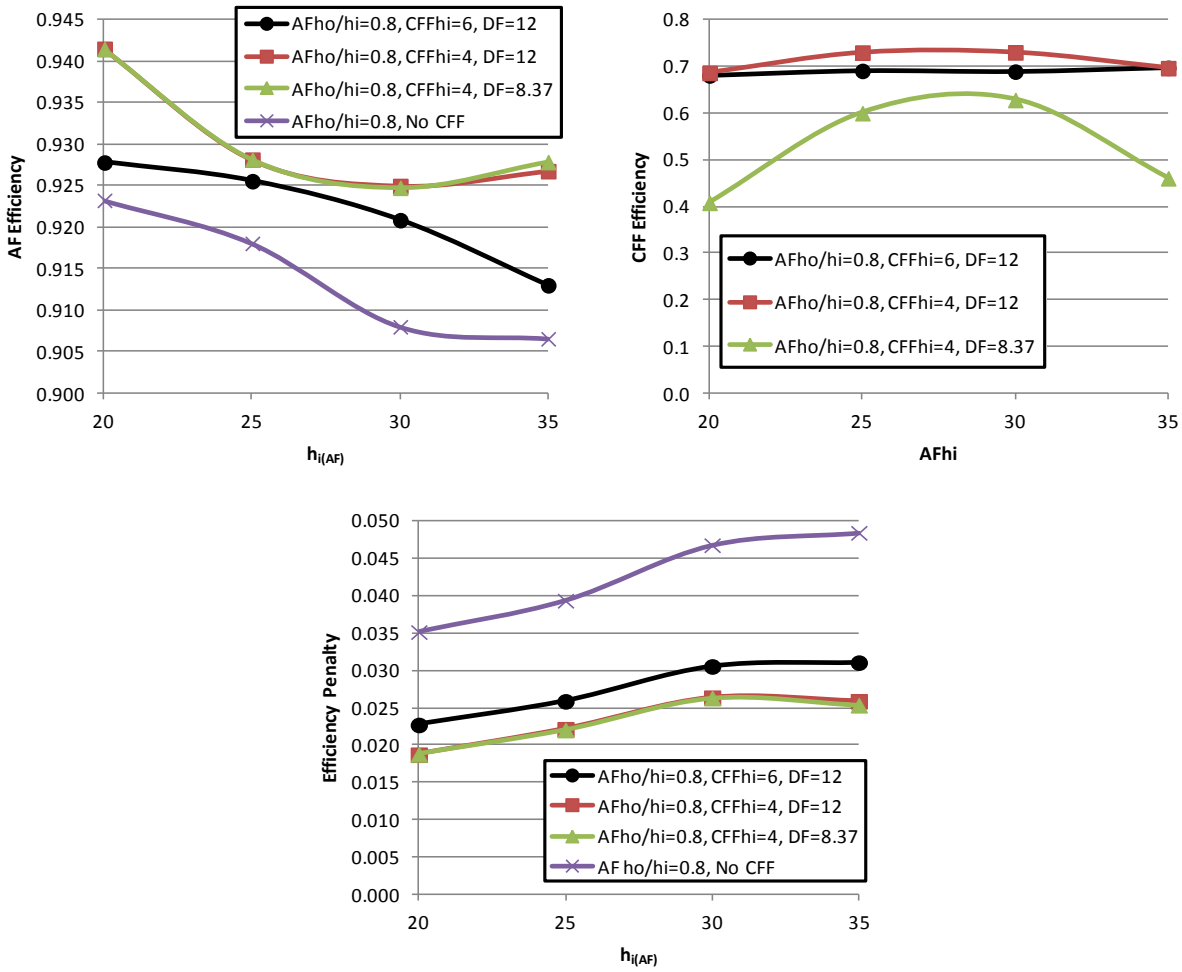

Fig. 51 BB AF/CFF: Efficiency and Efficiency Penalty Vs. $h_{i(AF)}$ for $h_{o(AF)}=0.8h_{i(AF)}$

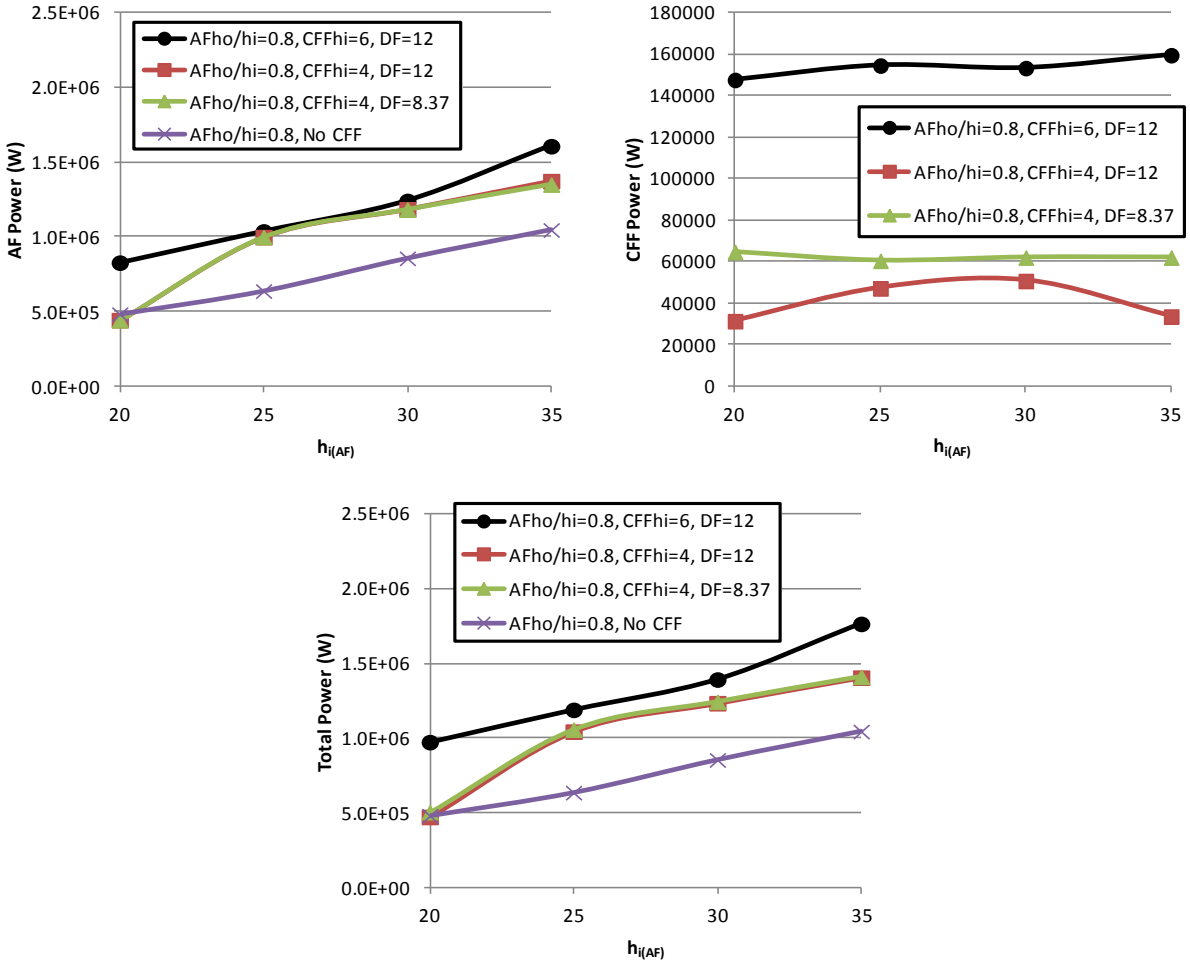

Fig. 52 BB AF/CFF: Power Vs. $h_{i(AF)}$ for $h_{o(AF)}=0.8h_{i(AF)}$

CFD Simulations of Full 3D BWB Geometry

In the previous sections the analyses were constrained to the 2D airfoil section corresponding to the BWB mid-span. In this section results are presented from integration of the black-box AF and CFF models into the full 3D BWB geometry. The goal here is not to perform a comprehensive design study, since this will require greater computational resources and time due to the grid refinement necessary to properly capture the boundary layer growth, shock position and strength, and flow features near the propulsor inlets and outlets. Instead the aim in this Phase I work was to extend the aforementioned 2D black-box models to the full 3D case, with the anticipation of further development into a robust design methodology (and implementation into an open source parallel CFD environment) in Phase II.

Several 3D BWB cases were simulated in Star-ccm+. All of the geometries were first constructed in Solidworks, and then exported into the CFD software package. The baseline BWB geometry was given to Propulsive Wing by NASA as a starting point. This geometry consisted of the spanwise airfoil sections. Taking this data into Solidworks, new lofts were created to approximate the actual smoothed contours of the vehicle. This geometry, with CFD surface mesh, is shown in Fig. 53. In order to reduce grid size, only half of the vehicle was simulated, with a symmetry boundary used at the mid-span, as shown in Fig. 54. This mesh consisted of 306,000 cells.

Unlike the 2D cases, where the freestream Mach number needed to be reduced to 0.75 in order to prevent a strong shock from forming on the suction surface, for the 3D cases the Mach number was increased back to the design cruise speed of 0.85. Figure 55 shows the Mach contours at the mid-span for the baseline geometry. The figure compares the flow field at 0^o, 3^o, and 6^o AOA. As anticipated, even at 6^o AOA, the shock present on the wing suction surface is still very week. In addition, the Mach contours offset 5m from the mid-span for the 0^o AOA case are shown in Fig. 56. Again, only a very weak shock is seen on the wing bottom surface. Pressure contours at 3^o AOA and 6^o AOA are shown in Figs. 57 and 58, respectively. Of particular note is the shock line that extends along the middle portion of the span near the trailing edge. The importance lies in that the propulsors will be placed here, and so one would expect a strong coupling between the two systems (i.e. between the external airframe shape and the fans).

The calculated C_L and C_D for these three cases are: $C_L(0^o)$=-0.064, $C_D(0^o)$=0.021; $C_L(3^o)$=0.23, $C_D(3^o)$=0.021; $C_L(6^o)$=0.483, $C_D(6^o)$=0.049. The L/D for these cases is about 10, which is lower than expected for a vehicle geometry such as this; however, this may be due to the type or refinement of the grid, since resolution of the shock location and strength plays a dominant role in determining the drag. More refined grids (up to over 1 million cells) were used for comparisons, but with only a minimal change in the value for C_D. Since the focus here is on

implementation of the new black-box propulsor models into the CFD calculations, the issue of accurate drag prediction will be deferred to future work in Phase II.

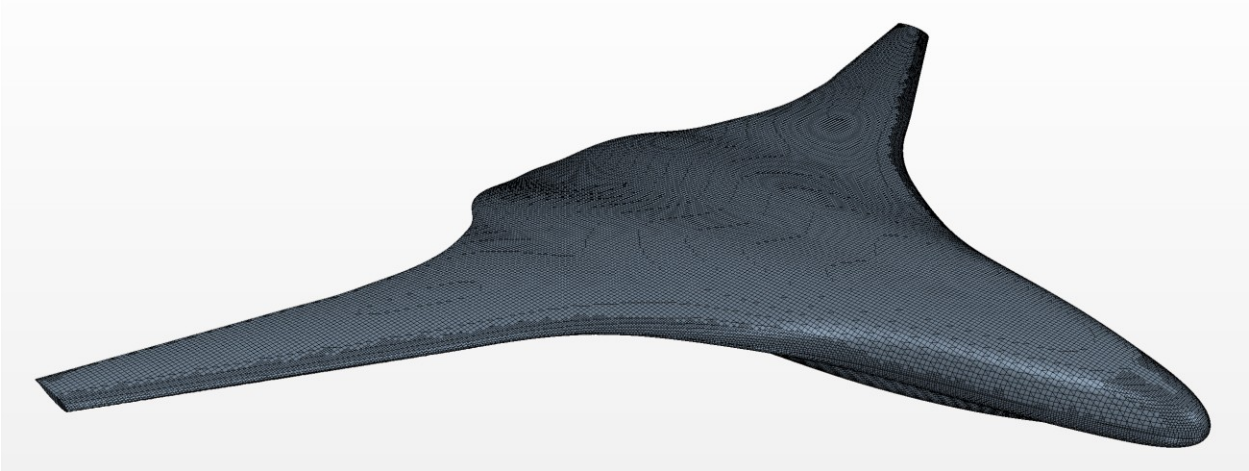

Fig. 53 Baseline BWB Geometry (from NASA)

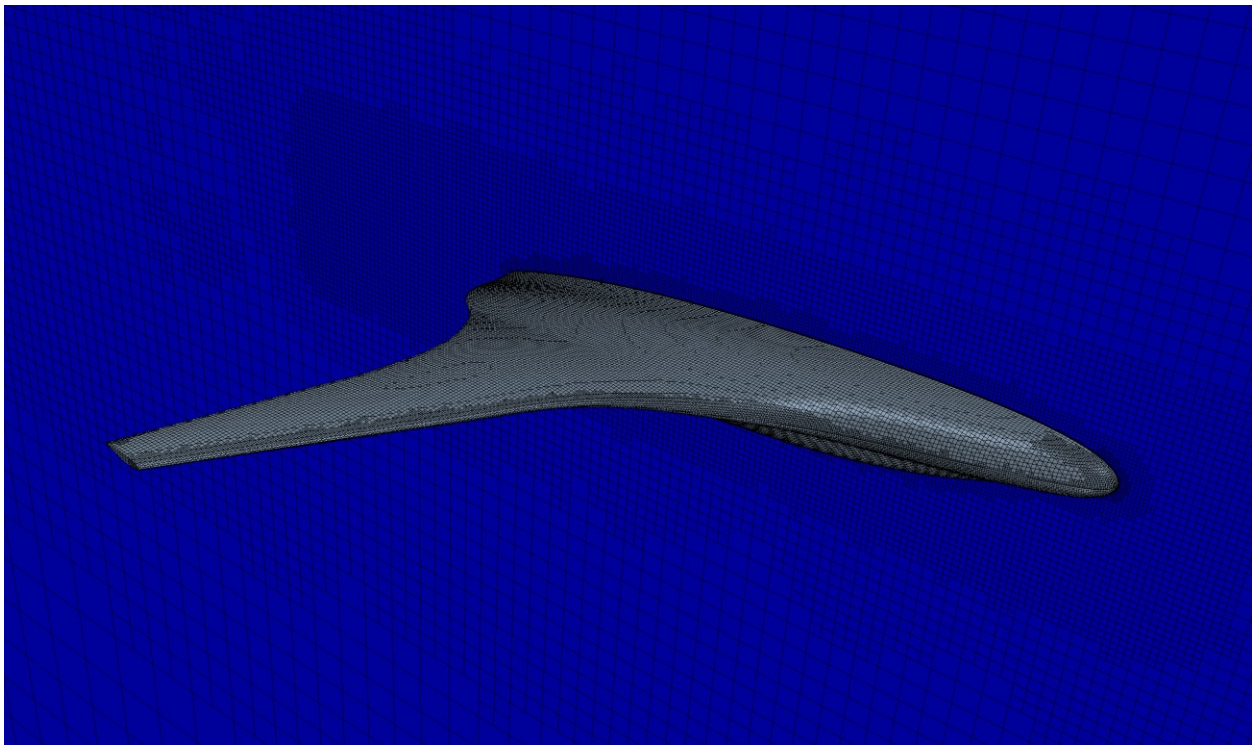

Fig. 54 Baseline BWB Geometry: Computational Mesh (306,000 Cells)

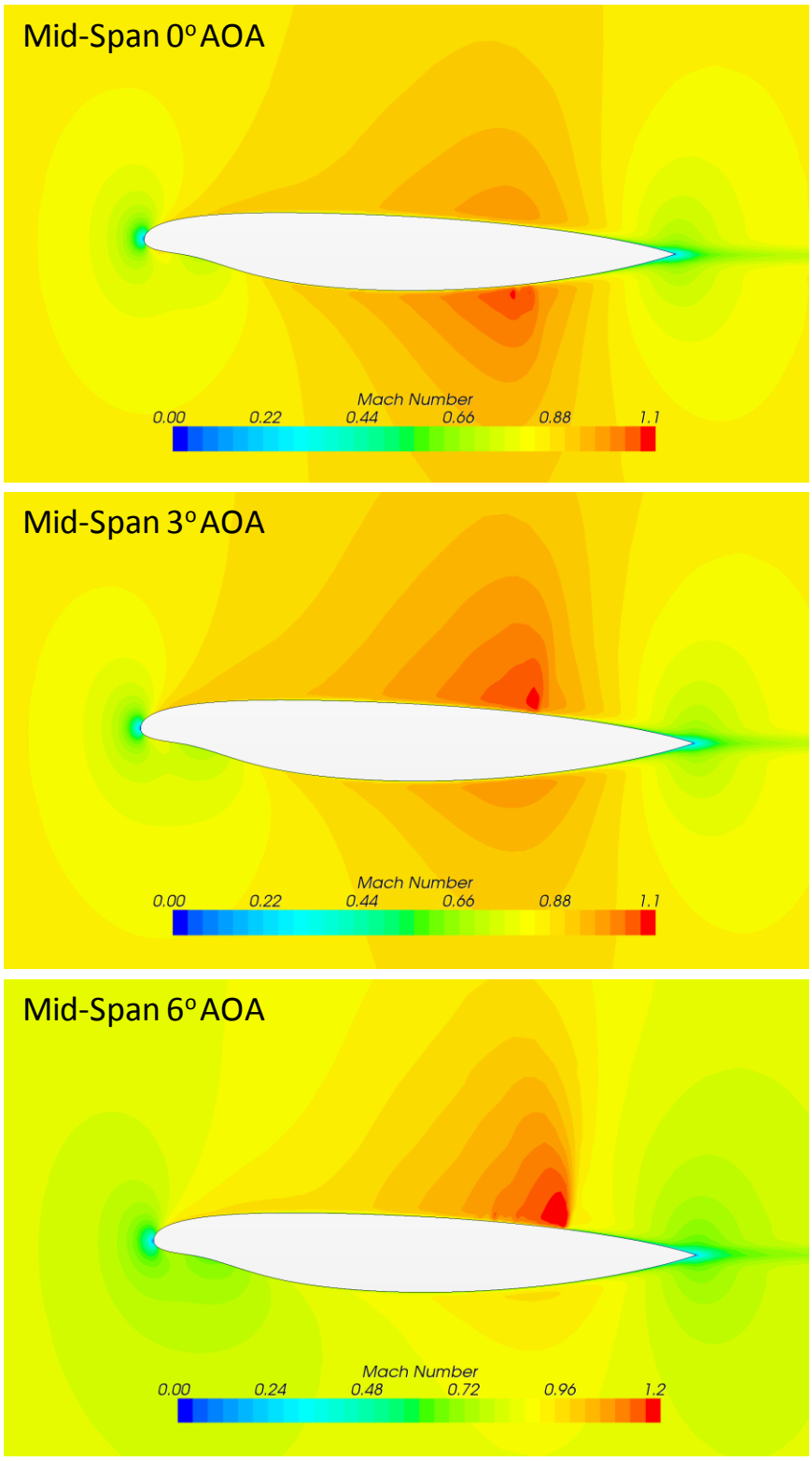

Fig. 55 Baseline BWB: Comparison of Mach contours at mid-span

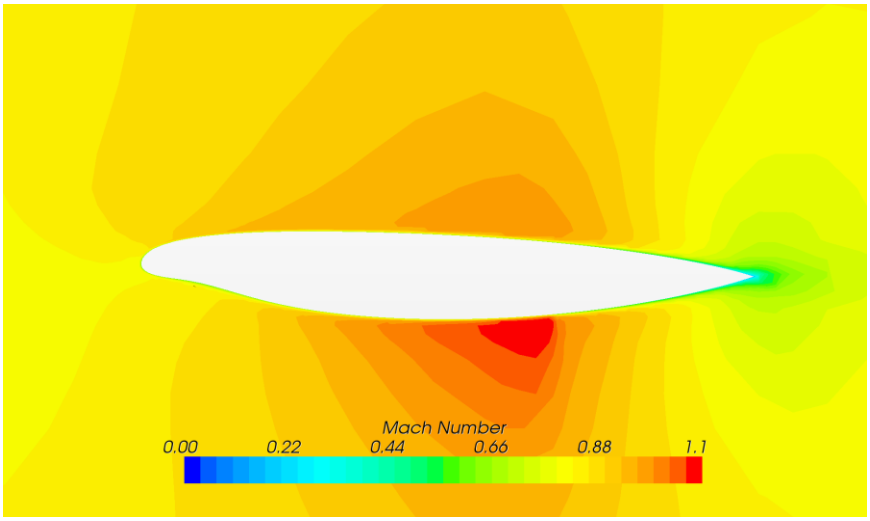

Fig. 56 Baseline BWB: Mach contours offset 5 meters from mid-span (0^o AOA)

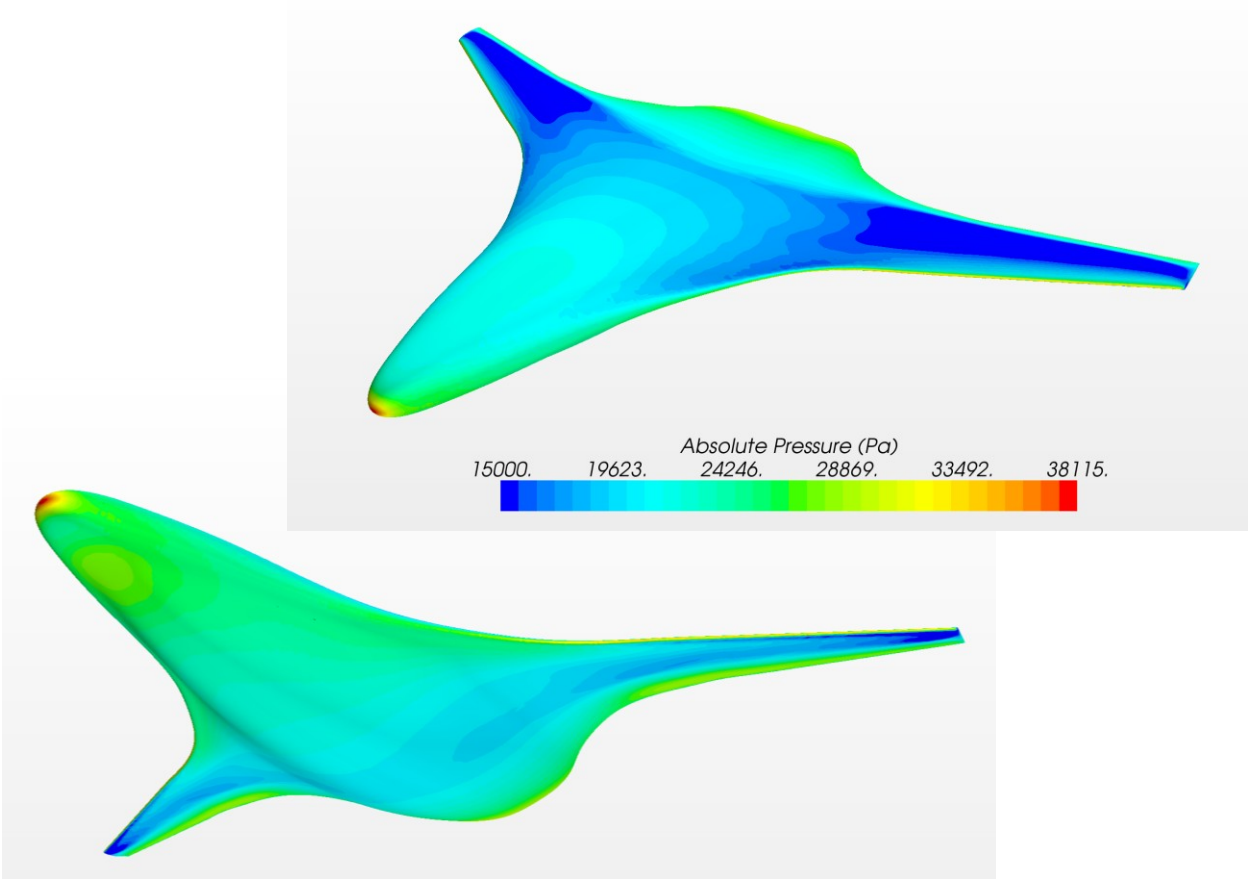

Fig. 57 Baseline BWB: Surface pressure contours (3^o AOA)

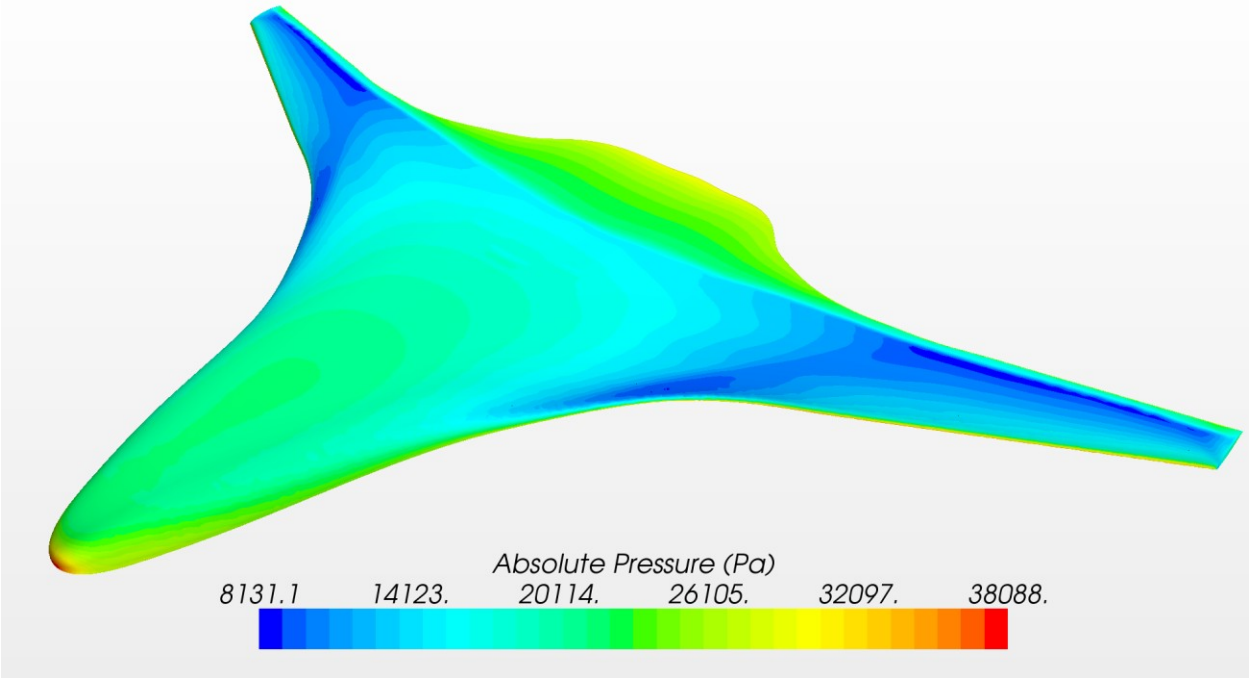

Fig. 58 Baseline BWB: Surface pressure contours (6^o AOA)

Before integrating the axial fan system into the BWB, it was necessary to modify the baseline geometry so that the trailing edge in the middle portion of the vehicle was straight (or nearly so). This new geometry is shown in Fig. 59. A computational mesh was created for the modified baseline case similar to the original, and consisted of 439,000 cells. Cases were run for this geometry, and surface pressure and Mach contour results at 3^o and 6^o AOA are shown in Fig. 60-62. For comparison, the calculated lift and drag coefficients for these cases are: $C_L(3^o)$=0.048, $C_D(3^o)$=0.015; $C_L(6^o)$=0.34, $C_D(6^o)$=0.03.

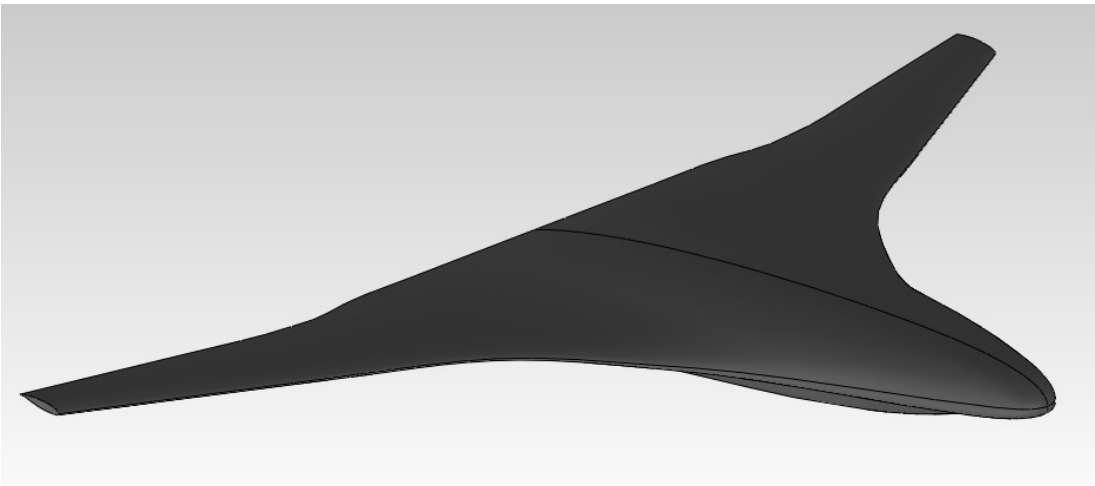

Fig. 59 Modified BWB (No Fans): Geometry

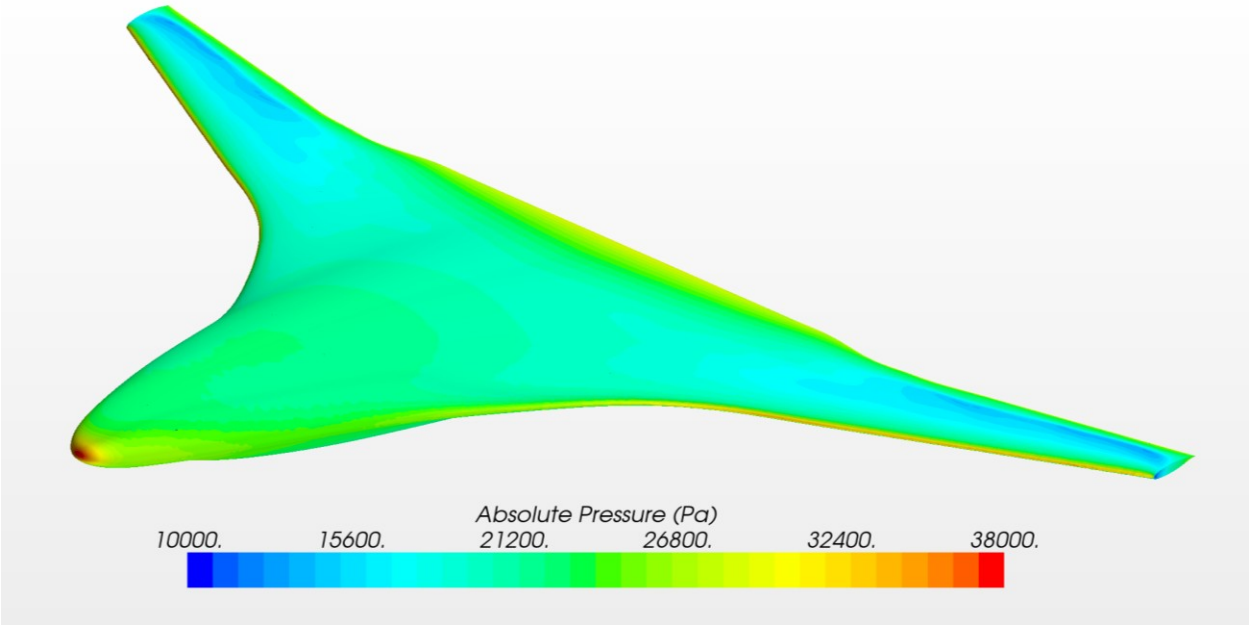

Fig. 60 Modified BWB (No Fans): Surface pressure contours (3^{o} AOA)

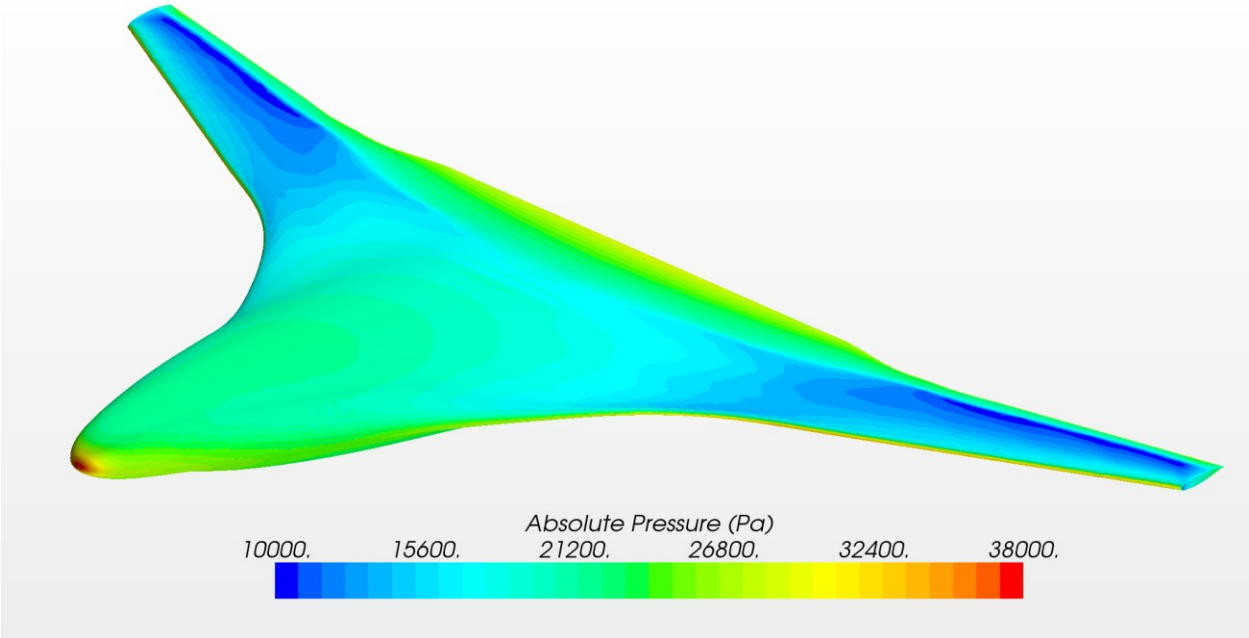

Fig. 61 Modified BWB (No Fans): Surface pressure contours (6^{o} AOA)

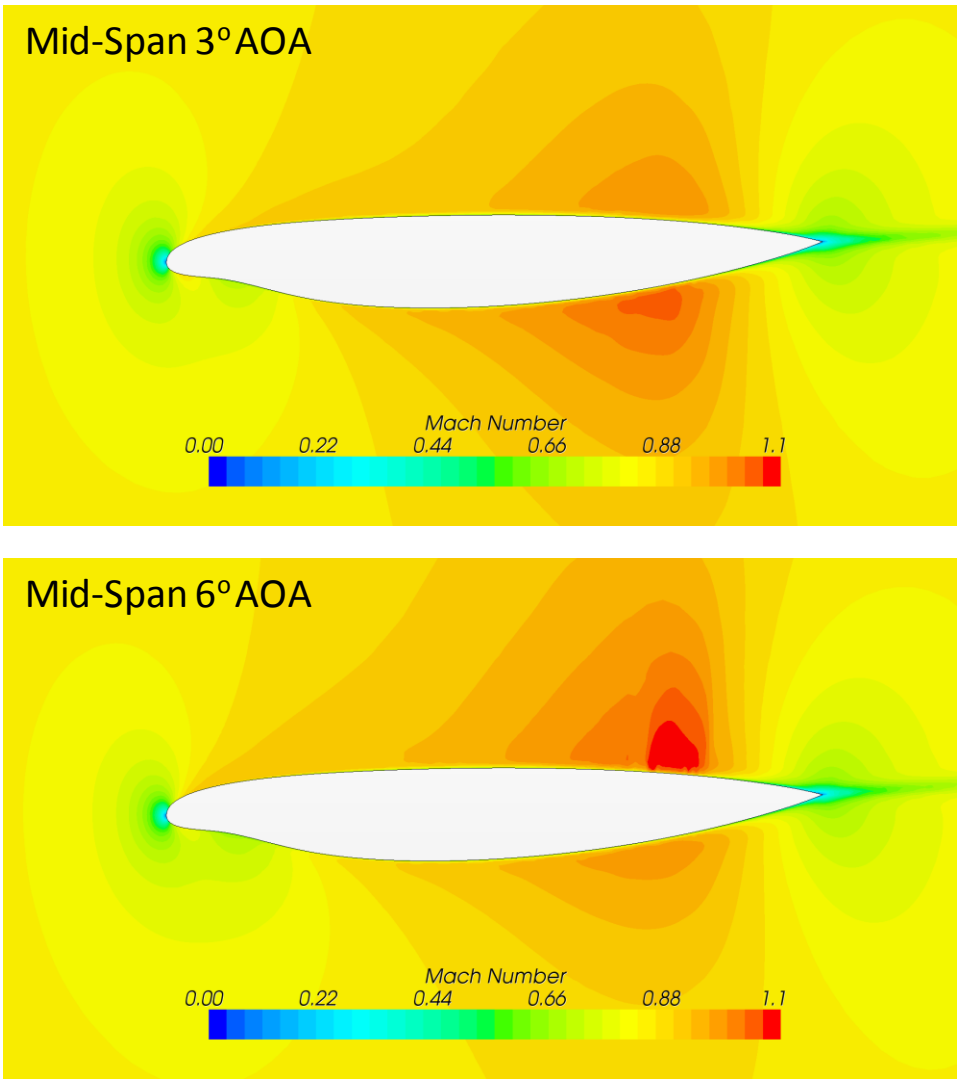

Fig. 62 Modified BWB (No Fans): Comparison of Mach contours at mid-span

With the modified geometry now created, next the BBAF geometry was added to the CAD model. To simplify the mesh generation and reduce convergence time, simple flat inlet and outlet faces were used. From the 2D cases, this was found to give less accurate results, particularly near the inlet; however, due to the computational and time constraints of the Phase I effort, this tradeoff was made. The axial fan geometry here corresponded to approximately a 30" inlet and 21.7" outlet (outlet to inlet height ratio = 0.72), with a propulsor span of 15m. The inlet height was not constant in this model due to the curvature of the vehicle; however, the geometry creation was simpler with a straight extruded shape for the inlet height. In future design studies, multiple axial fans could be included by utilizing separate inlet faces for each (with corresponding outlets). The geometry for the BBAF test case is shown in Fig. 63 (with the mirror image also shown). As before, the actual CFD calculations were performed on only half of the vehicle with a symmetry boundary used at the mid-span.

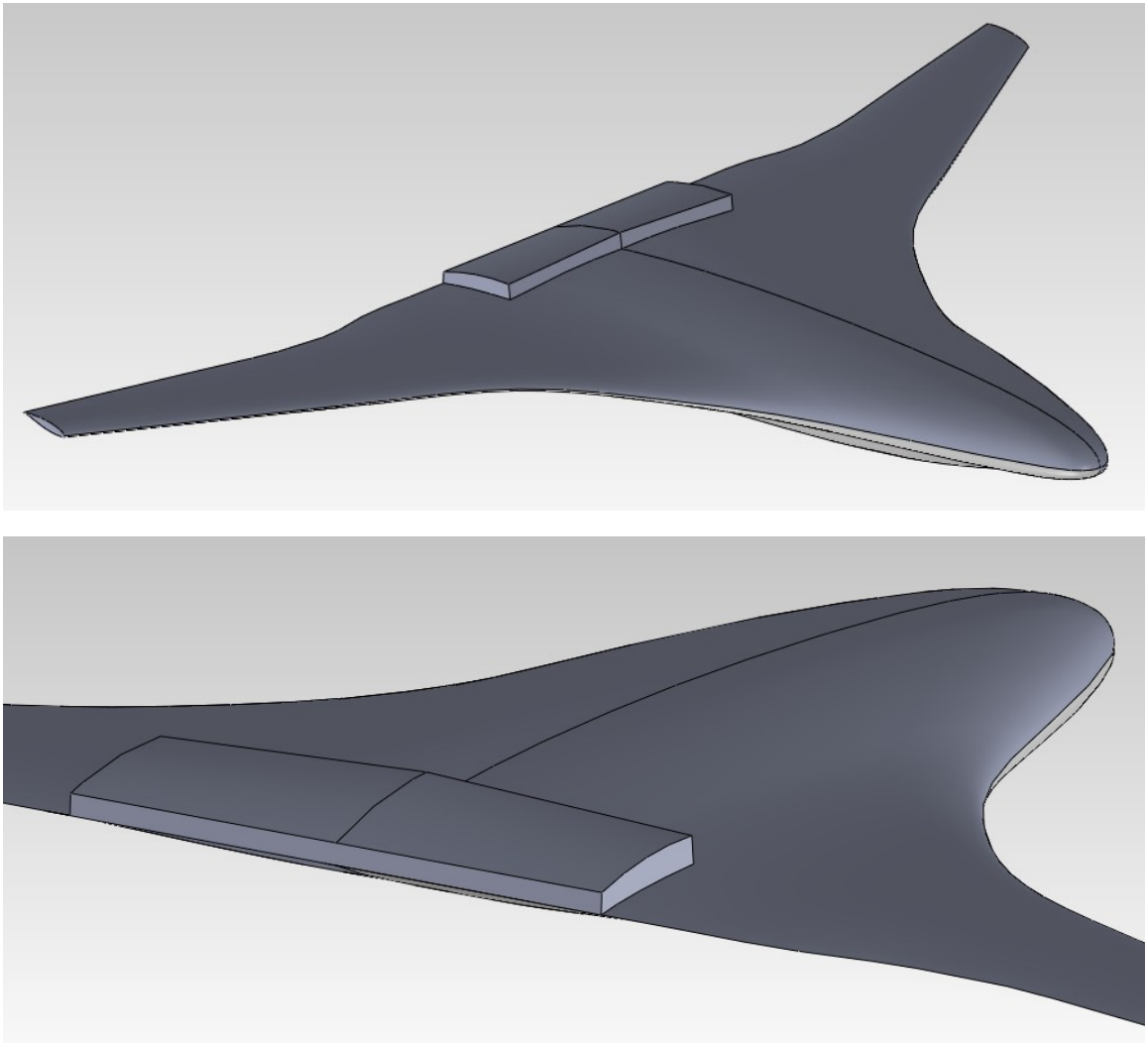

Fig. 63 Modified BWB (With BBAF): Geometry

Figure 64 shows the surface pressure contours for the first BBAF case with the mass flow rate (MFR) set to 425 kg/s at 3^o AOA. The calculated $C_{D(net)}$=0.005 and $C_{L(net)}$=0.112, TPR=1.25, η_{pen}=5.5%, and Power = 15.4 MW (for the entire 15m propulsor span). The Mach contours at the mid-plane and offset 5m from the centerline are given in Fig. 65. Compared with the case without the BBAF included, a shock appears on the axial fan top shroud. A closeup of this case is shown in the upper part of Fig. 66. Here it can be seen that the boundary layer is not properly ingested into the axial fan, resulting a region of lower velocity near the inlet. To remedy this, the MFR was increased to 475 kg/s. This case is shown in the bottom portion of Fig. 66. From the figure, the efficient ingestion of the boundary layer in seen, along with substantial wake filling. This is further demonstrated in Fig. 67 with the total pressure contours. Here, the entire boundary layer enters the axial fan, with almost no total pressure loss seen on the AF top shroud. The high total pressure at the AF outlet represents the thrust necessary to propel the vehicle. The calculated values for this latter case are: $C_{D(net)}$=0.0014, $C_{L(net)}$=0.119, TPR=1.34, η_{pen}=5.6%, and Power = 25.4 MW (for the entire 15m propulsor span).

Streamlines for this case are given in Figs. 68 and 69. The flow into and around the axial fan propulsion systems is smooth. The integration of the BBAF model into the 3D geometry was no more difficult than the earlier 2D cases, with convergence after only a few thousand iterations. Although the main focus here is on implementation of a dual AF/CFF propulsion model, the BBAF model has many potential uses, not only for the current design, but any other where one wishes to approximate the direct effect of the propulsor on the airframe aerodynamics. This could even include more conventional airframes, where typically early design CFD runs will not include a propulsor, since the vehicle outer mold lines and engine designs will be completely decoupled (i.e. one assumes little or no influence of one on the other). Although this is often an acceptable approximation for conventional designs, as shown here, the influence these two systems have on one another cannot be neglected, even early on in the design phase.

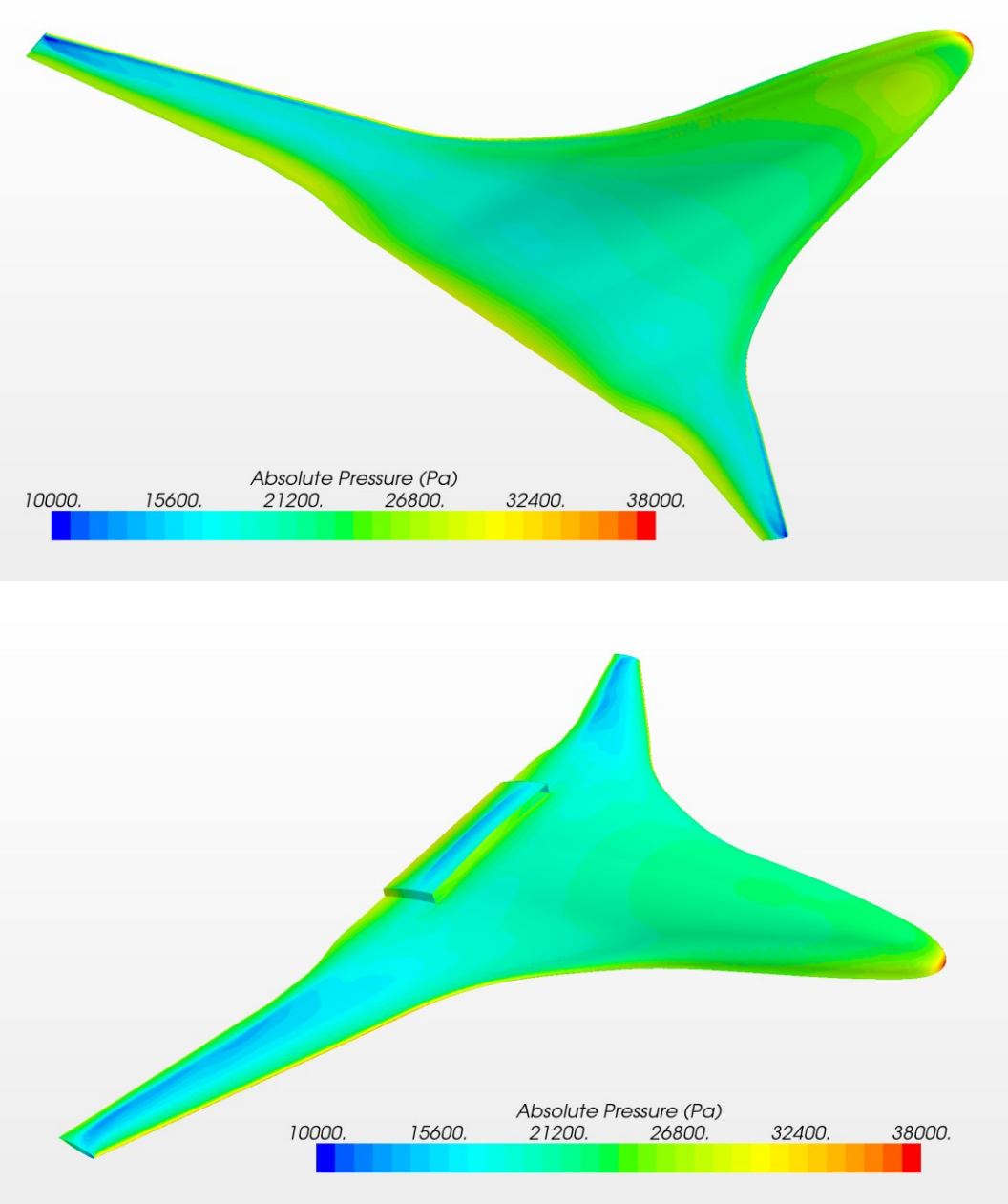

Fig. 64 Modified BWB (With BBAF): Surface pressure contours (3^{o} AOA)

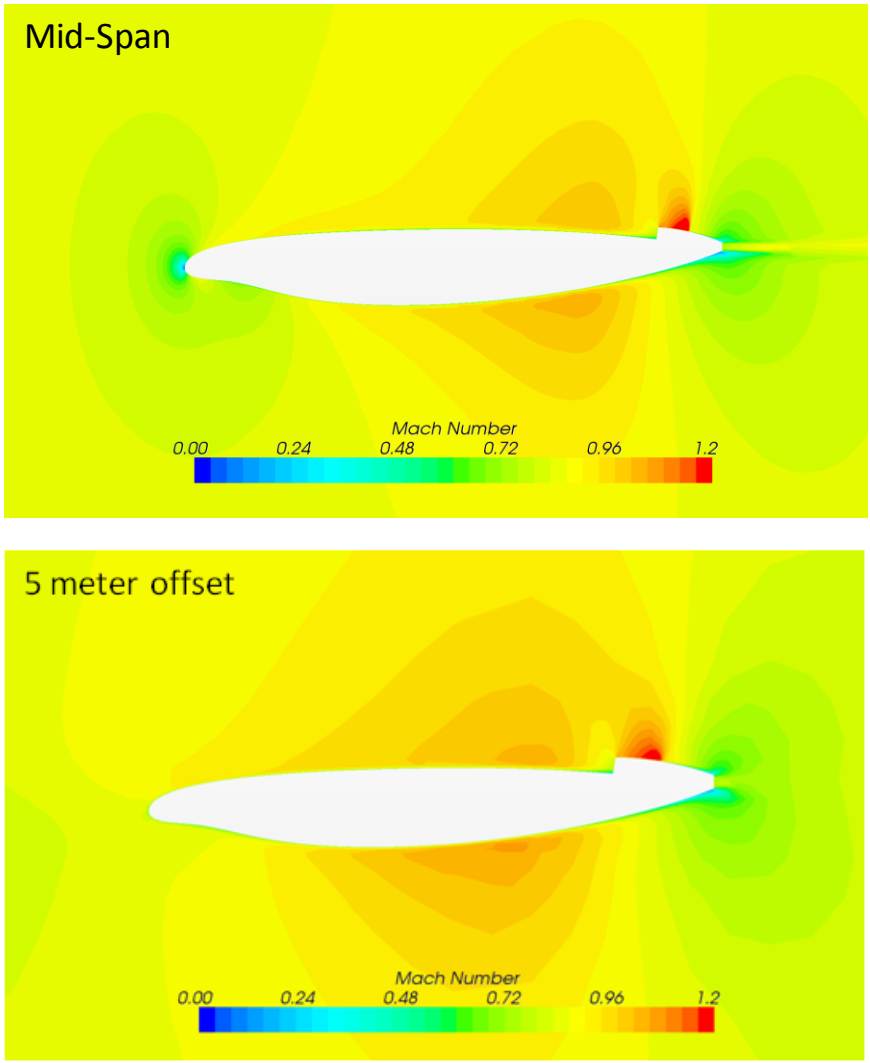

Fig. 65 BWB With BBAF: Mach contours at mid-span vs. 5 m offset (MFR = 425 kg/s, 3^{o} AOA)

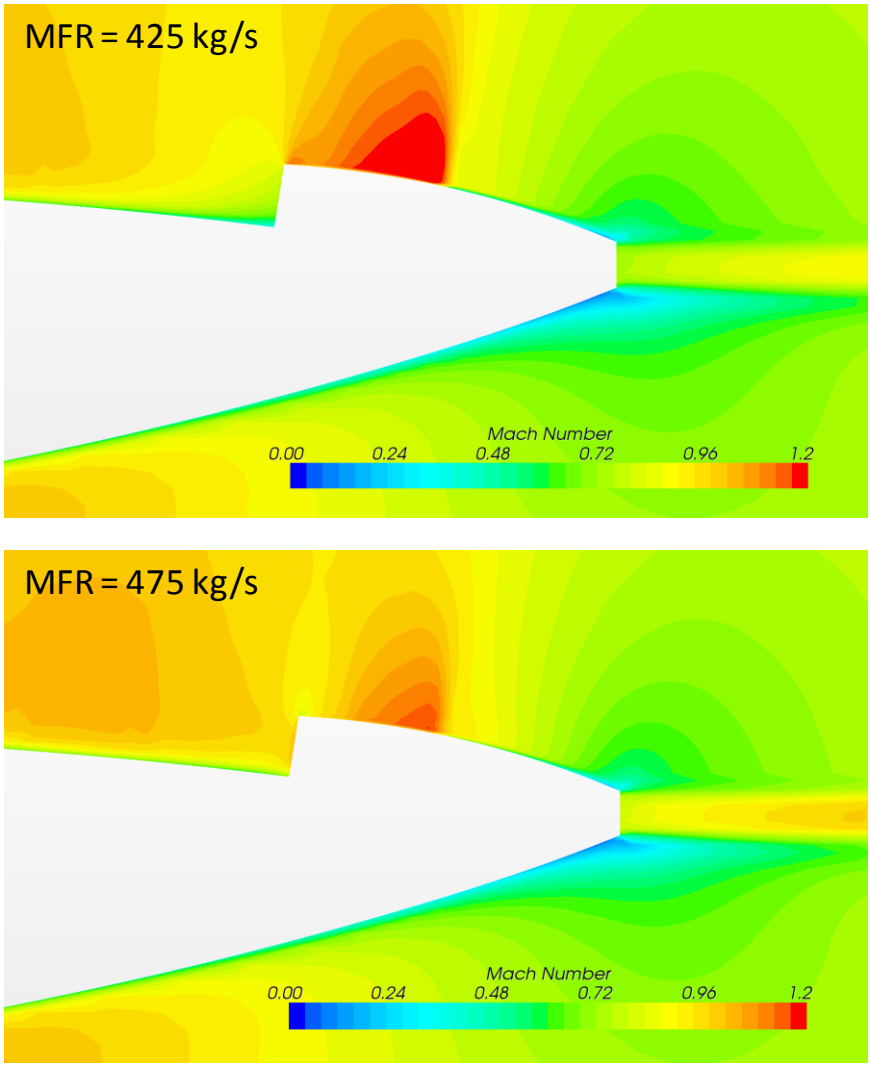

Fig. 66 BWB With BBAF: Mach contours at mid-span (MFR = 425 kg/s vs. MFR = 475 kg/s)

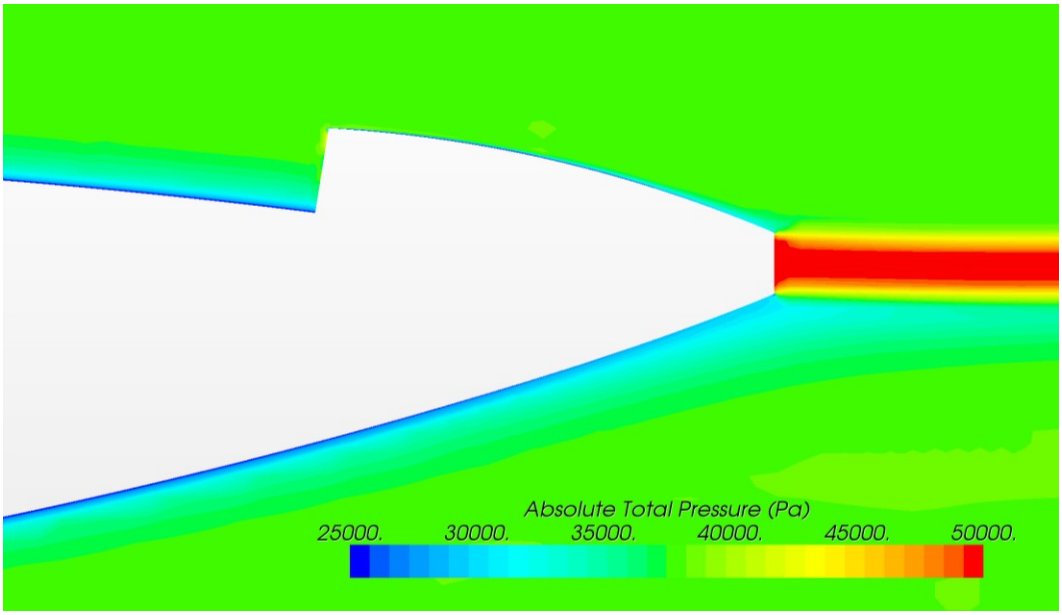

Fig. 67 BWB With BBAF: Total pressure contours at mid-span (MFR = 475 kg/s, 3^{o} AOA)

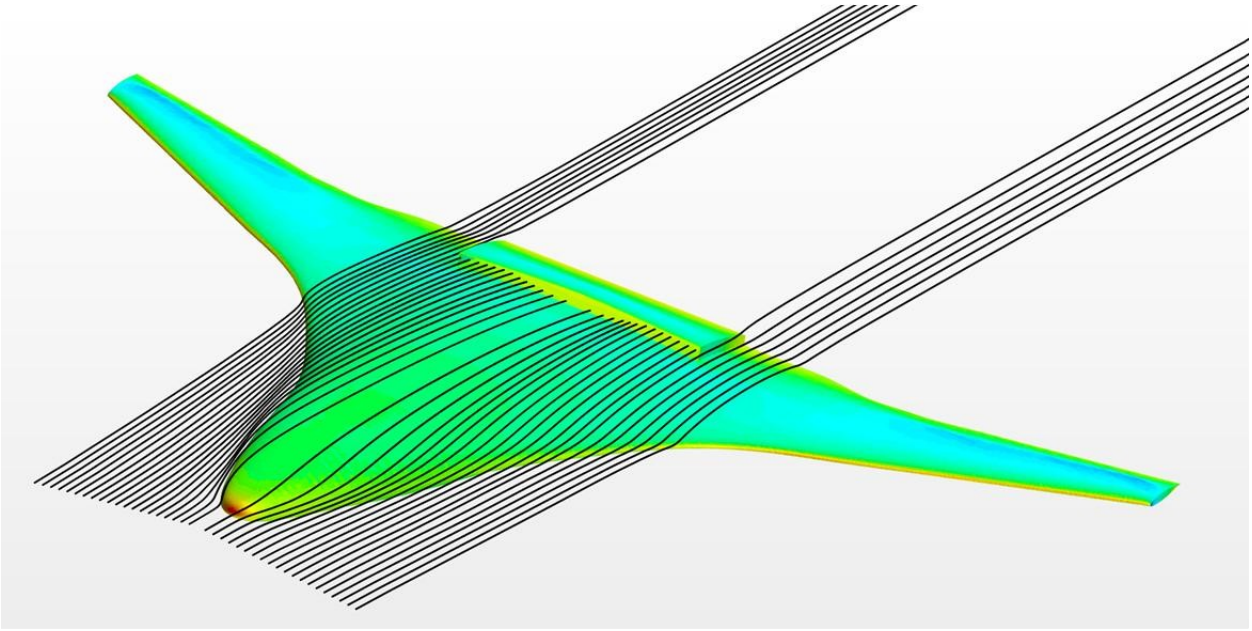

Fig. 68 BWB With BBAF: Vehicle streamlines (MFR = 475 kg/s, 3^{o} AOA)

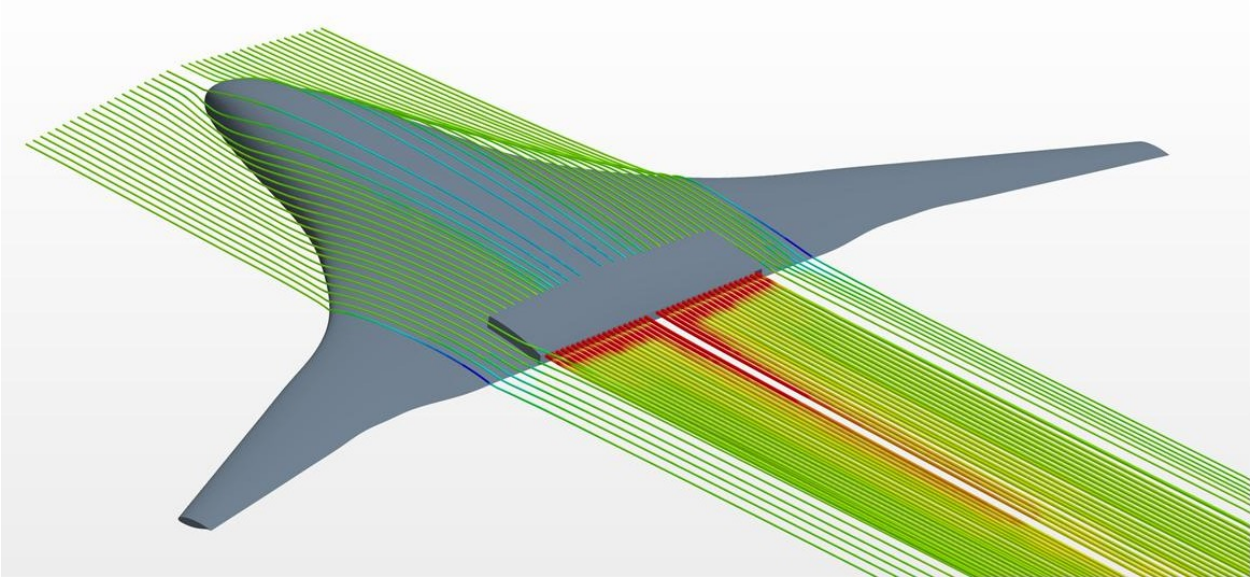

Fig. 69 BBAF vehicle streamlines contoured by total pressure (MFR = 475 kg/s, 3^{o} AOA)

In order to demonstrate the full 3D BWB vehicle with the BB AF/CFF propulsion model, one final calculation was performed. The BBAF model shown in Fig. 63 was further modified so that a 4" BBCFF inlet was present below the BBAF inlet, and a 2.5" BBCFF outlet was directly below the BBAF outlet. As previously mentioned, for better convergence inlet and outlet ducting should be used in the CFD model; however, due to computational and time constraints here the current model did not include this feature. As a result, convergence was challenging due to too much coupling between the pressure outlet boundary conditions used at the BBAF and BBCFF inlets and the external flow near the propulsor. Nevertheless, the model itself performed well and almost exactly as the 2D case, and so one would expect with additional geometry and grid refinements will work well. Figures 70 and 71 show the geometry for this case, while Figs. 72 and 73 show representative total pressure and streamline outputs.

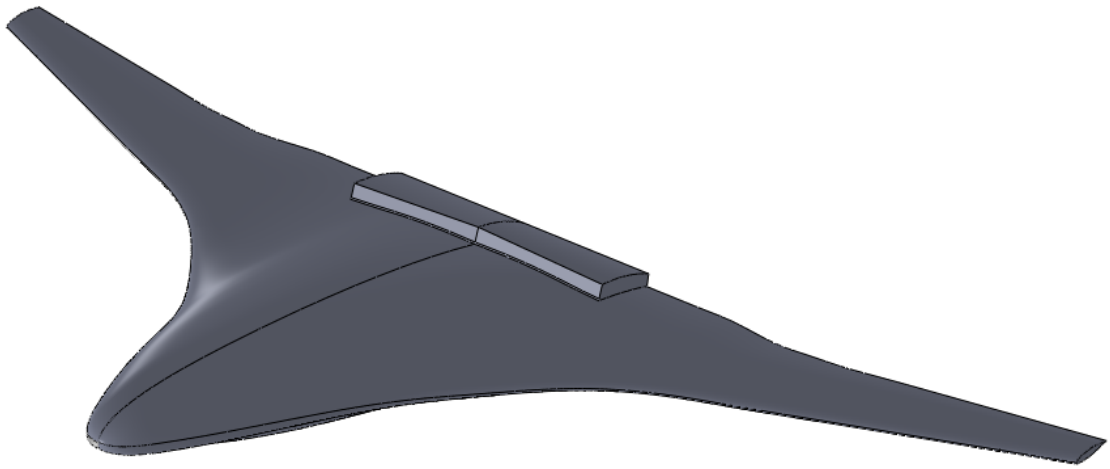

Fig. 70 BWB with BB AF/CFF: vehicle geometry

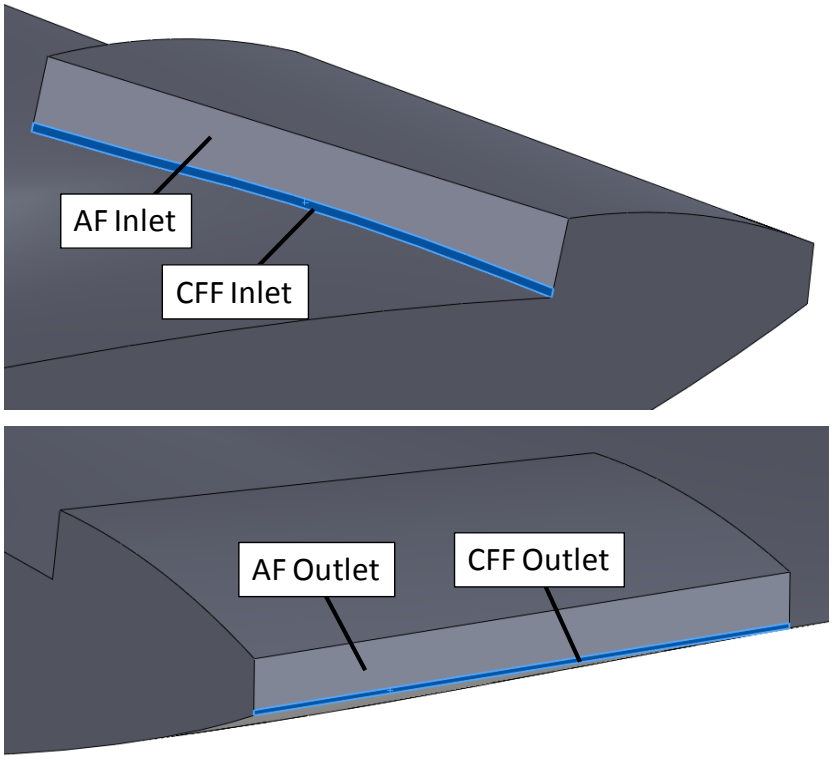

Fig. 71 BWB with BB AF/CFF: closeup near propulsor inlets and outlets

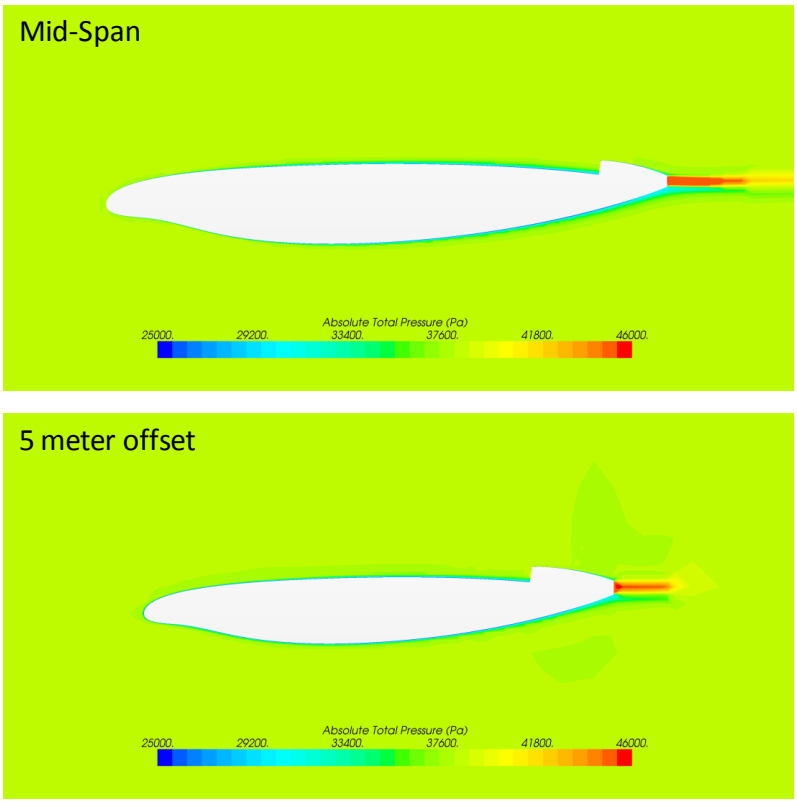

Fig. 72 BWB with BB AF/CFF: Total pressure contours at mid-span and offset 5m from centerline (MFR_{AF} = 475 kg/s, MFR_{CFF} = 35 kg/s, 3^{o} AOA)

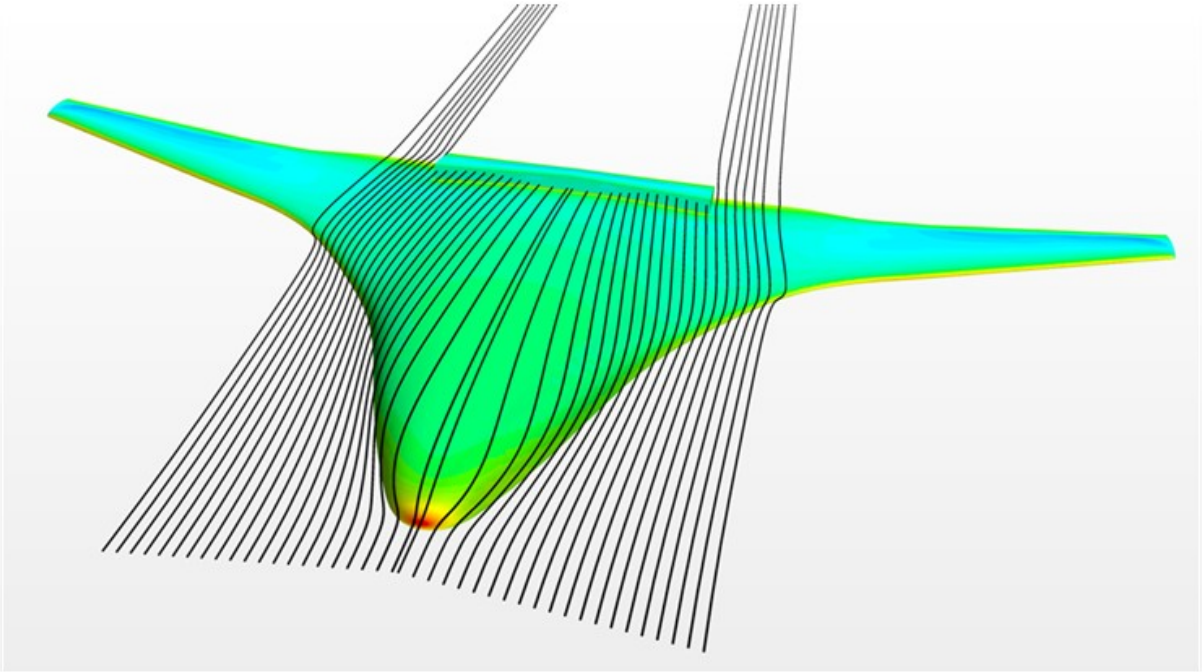

Fig. 73 BWB with BB AF/CFF: streamlines (MFR_{AF} = 475 kg/s, MFR_{CFF} = 35 kg/s, 3^{o} AOA)

System Layout, Finite Element Analysis, and Preliminary Weight Estimate

A preliminary calculation was performed to demonstrate the analysis method, as well as provide a baseline, for the weight of the CFF propulsion system. The same 12" diameter CFF was used in these calculations as was used previously for the CFF-Airfoil simulations. The width of the CFF inlet was assumed to be equal to the width of the rectangular AF inlet, here taken as 4 ft. This corresponded with the case from Ref. 4. A CAD model showing the basic layout for the system is given in Fig. 74. Propulsive Wing currently manufactures composite cross-flow fans from a combination of quasi-isotropic carbon fiber flat plates (for the end and divider plates) and pultruded carbon fiber blade sections. This manufacturing process works well for this type of fan, since the greatest forces are in the radial direction. The pultruded carbon fiber offers very high bending stiffness to weight ratio. For the fan shown in Fig. 74 (12” diameter, 47.5” length), the weight is approximately 27 lbs.

To establish a structural baseline for the fan blades, an FEA calculation was performed for a single blade segment. The blade section was assumed to span only 12”. From one of the CFF-Airfoil CFD simulations, the x and y aerodynamic force components (i.e. pressure and shear) were extracted as functions of azimuth angle (with zero degrees taken horizontally toward the outlet), and are shown in Fig. 75. For the present case, the maximum aerodynamic force is about 250 N/m. By contrast, for the 12” blade segment simulated here, the centrifugal force at 6,000 rpm is approximately 5,200 N. Thus the centrifugal force will be a major driving factor for the structural design of the blades. To further investigate this, a FEA calculation was setup corresponding to the aforementioned 12” blade segment. The ends were set as fixed boundary conditions. A 76.2 N load was applied normal outward from the surface to approximate the aerodynamic loading. A 5,200 N load was also applied to the blade in the y-direction to simulate

the centrifugal force. Figure 76 shows the von Mises stresses for the blade segment. Clearly there is a large amount of deformation due to the centrifugal force. The stresses at 300-400 MPa are also fairly high. Although pultruded carbon fiber can typically reach 1-1.5 GPa stress levels without problems, this may not be an acceptable safety factor for the system.

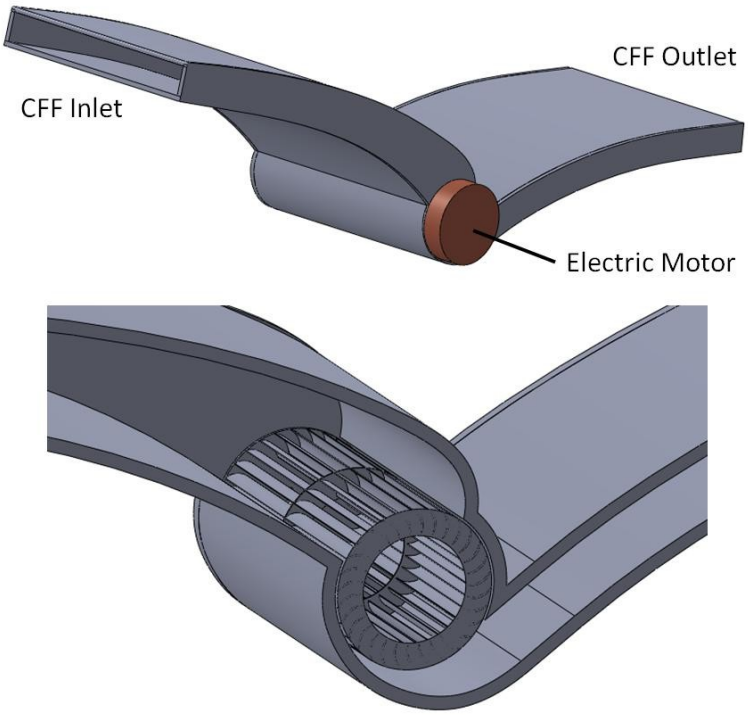

Fig. 74 CFF system layout

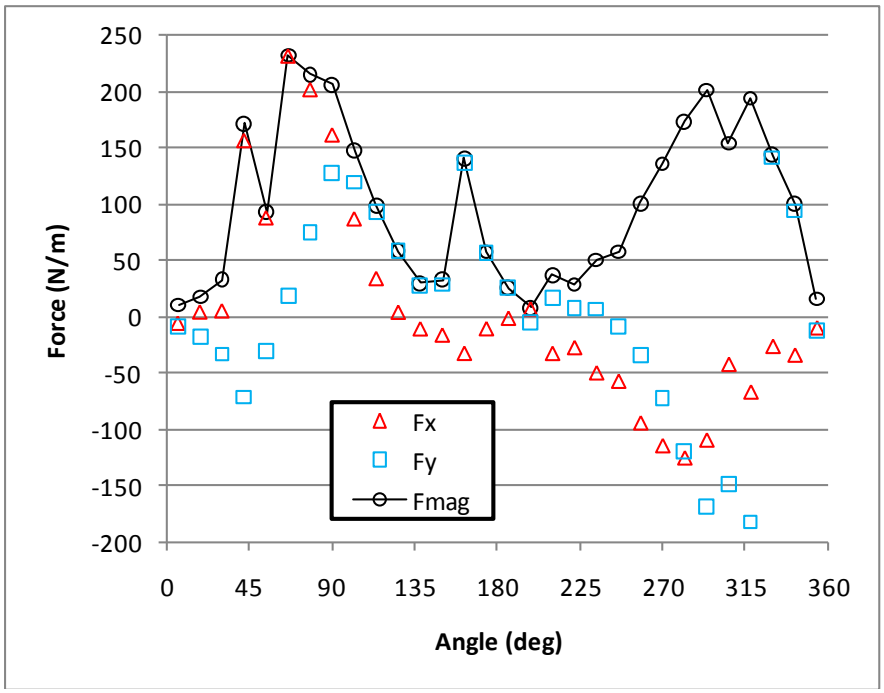

Fig. 75 CFF blade forces as a function of azimuth angle

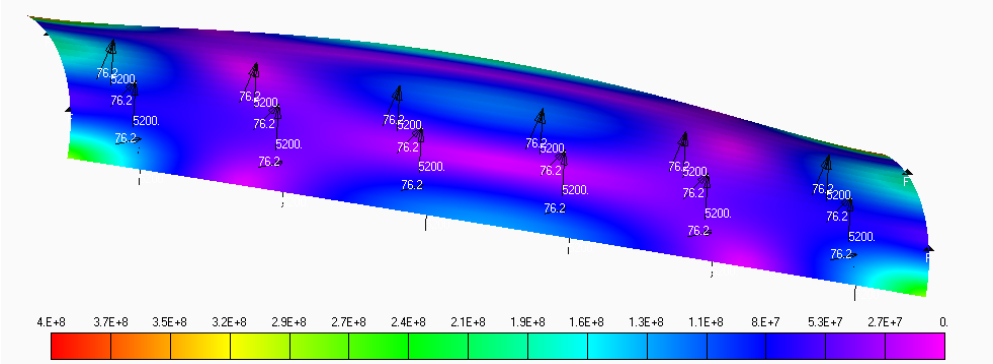

Fig. 76 Von Mises Stresses in CFF blade (load in N, stresses in Pa)

An ideal electric motor for this application will be capable of producing very high torque in the correct rpm range for the cross-flow fan. It must also take up as little space in the spanwise direction as possible. One potential candidate is a pancake motor, typically used in electric vehicles. An example is the Protean Drive In-Wheel Motor, from Protean Electric, Inc. Protean Electric's PD18 motor and specifications are shown in Fig. 77. Although this motor does not specifically meet the needs of the present fan design, the basic configuration works well when integrated into a CFF system. The large diameter would produce the high torque necessary to drive the CFF. These motors also include integrated control circuitry.

	Units	PD18
Peak output power @400Vdc	kW	81
Continuous output power @ 400Vdc	kW	64
Peak output torque	Nm	800
Continuous output torque	Nm	500
Nominal input voltage range	Vdc	200 – 400
Width	mm	115
Diameter	mm	420
Total motor mass	kg	31

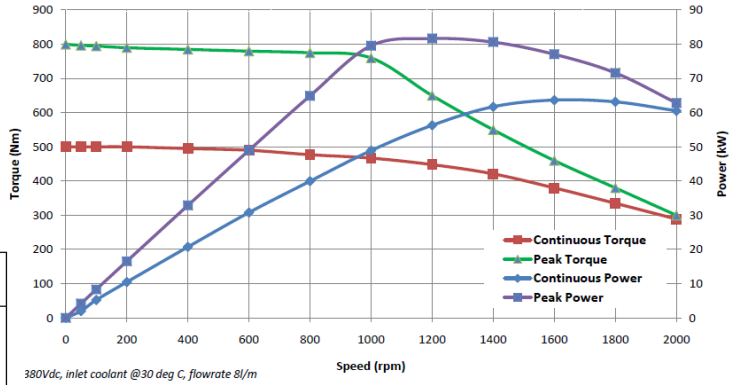

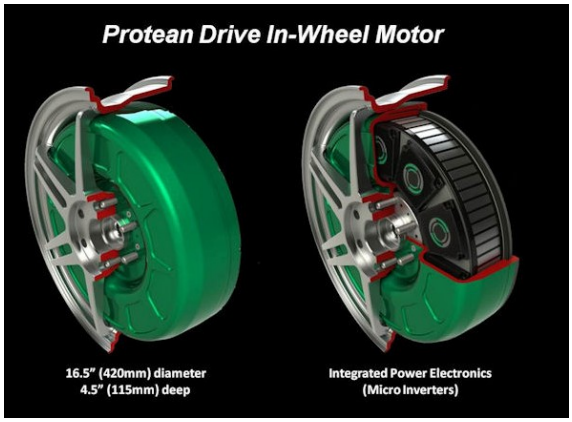

Fig. 77 Protean in-wheel electric motor specs (from Ref. 5)

Although the fan blade and electric motor baselines look promising, there are several options available to reduce their weights.

1. Reduce fan diameter: Fan weight is approximately linear with fan diameter, so a reduction in size from 12" to 8.37" diameter would yield a fan that weighs about 19 lbs. In addition, smaller diameter cross-flow fans will operate at higher rpm, but require lower torque (for a given power input). High speed, low torque motors typically weigh much less than low speed, high torque motors.
2. Increase blade thickness: By including a lightweight core material, for example foam, placed internally within the blades, the blade stiffness will be increased dramatically. This will allow a reduction in carbon fiber material, thus reducing weight. The combination of increased bending stiffness and reduced weight will dramatically lower blade stresses.
3. Carbon fiber motor casing: Utilize an electric motor with a carbon fiber composite casing instead of one made from aluminum or steel, like the current production motors made for electric cars. By replacing metal with carbon fiber, there is the potential for a 2-3 times weight savings in the motor casing.

Conceptual 3D Renderings of the Proposed AF/CFF BWB Configuration

Below are several conceptual 3D CAD renderings of the proposed AF/CFF BWB configuration (Figs. 78-83). In the models, two different size fans were utilized, since it is hypothesized that an optimized design will have a decreasing fan size in the spanwise direction. Practically this will probably result in two or three different fans sizes, since this would reduce design, fabrication, and maintenance costs over a design where every fan was a different size.

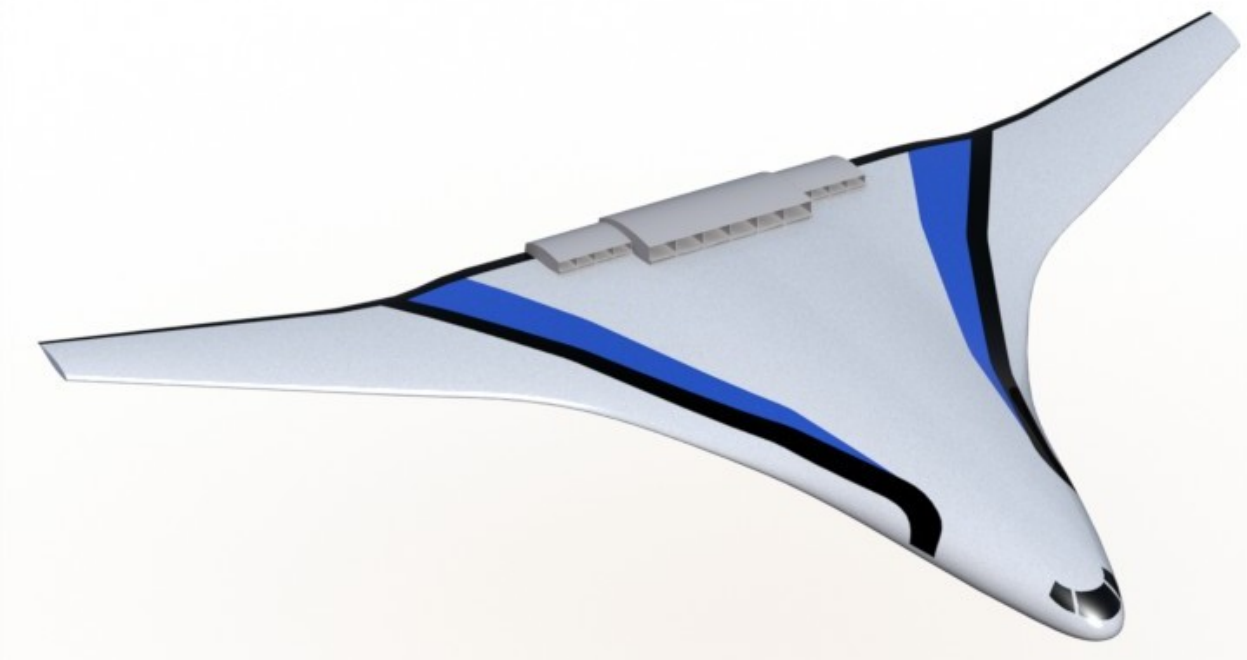

Fig. 78 AF/CFF BWB with propulsors at trailing edge

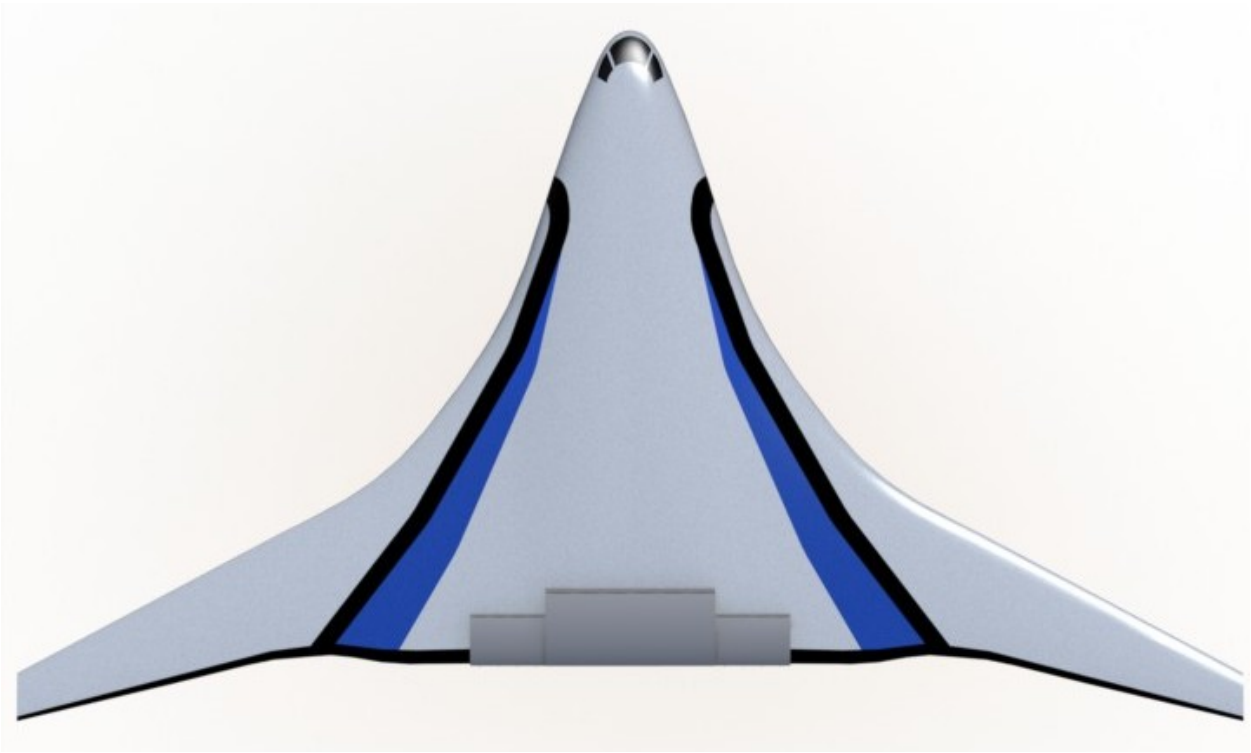

Fig. 79 AF/CFF BWB with propulsors at trailing edge (top view)

Fig. 80 AF/CFF BWB with propulsors at trailing edge (side view)

Fig. 81 AF/CFF BWB with propulsors at 80% chord

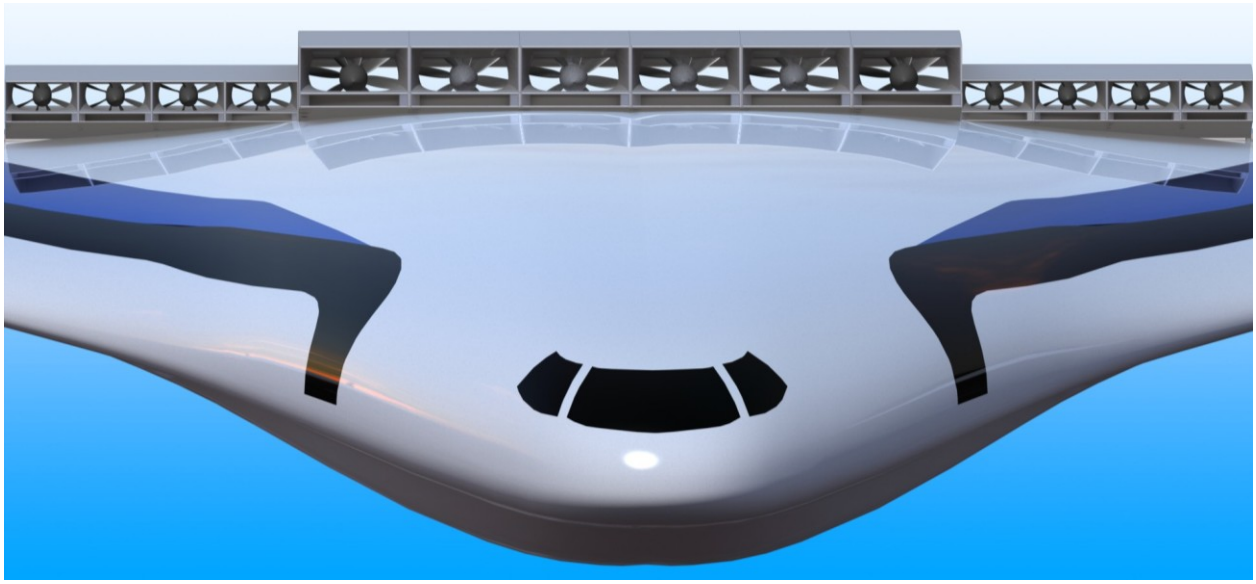

Fig. 82 Front view of AF/CFF BWB

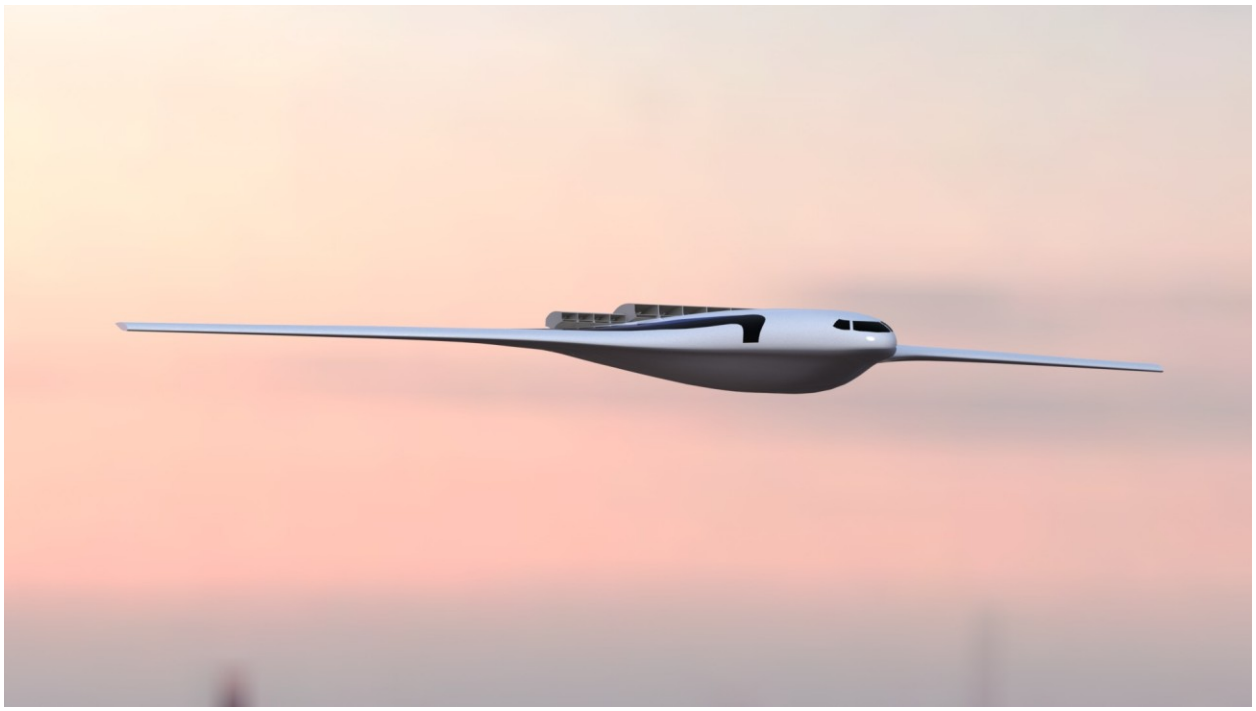

Fig. 83 Conceptual rendering of AF/CFF BWB

Phase III Potential

Assuming success in Phase II, where wind tunnel testing will be performed to validate and refine the CFD models, along with an extension of the current 3D analyses to a full design, significant opportunities exist to utilize this technology in Phase III. Firstly, the methods and computational modeling tools developed in this SBIR effort will be useful to researchers for future design efforts. One of the primary outcomes of this Phase I effort was showing the significance and magnitude of the coupling between the airframe and propulsor designs, thus necessitating an equally coupled design procedure. The models developed here and in Phase II will be made openly available to other researchers for future use upon the completion of the Phase II work.

Secondly, the Air Force Research Lab has expressed interest in this concept for future Air Force UAV applications. Propulsive Wing currently has a Cooperative Research and Development Agreement (CRADA) with AFRL. Due to the mutual interest within both organizations, in Phase III we will work to develop a collaboration between NASA and AFRL to design and build a scale-model UAV demonstrator aircraft, with the goal of eventually scaling up the model to meet specific NASA or Air Force missions. Such aircraft would be capable of flying at higher altitude, higher speed, and with longer endurance than current UAV systems, and eventually could lead to follow-ons to the Predator and Global Hawk classes of UAVs.

Lastly, AFRL has also expressed an interest in the development of a small UAV powered by turboelectric propulsion. This vehicle would most likely be air-launched, and combine the high lift, large payload capabilities of the current mini Propulsive Wing prototypes with the fuel and thrust benefits of a micro turbine electric generator power system.

References

1. Tillman, T.G. et al., "System Study and Distortion-Tolerant Fan Design for a Boundary Layer Ingesting Propulsion System," *UTRC Technical Report RR-0100151*, July 2010.

2. Jang, C., Choi, S., and Kim, K., "Effects of Inflow Distortion due to Hub Cap's Shape on the Performance of Axial Flow Fan," *Journal of Fluid Science and* Technology, Vol. 3, No. 5, 2008.

3. Kawai, R., Brown, D., Roman, D., and Odle, R., "Acoustic Prediction Methodology and Test Validation for an Efficient Low-Noise Hybrid Wing Body Subsonic Transport," *NASA Contract Number NNL07AA54C*, October 2008.

4. Felder, J., Kim, H.D., Brown, G., and Chu, J., "An Examination of the Effect of Boundary Layer Ingestion on Turboelectric Distributed Propulsion Systems," *AIAA Aerospace Sciences Meeting*, January 2011.

5. Protean Electric company website: [http://www.proteanelectric.com/products/2/products.html]

REPORT DOCUMENTATION PAGE

Form Approved
OMB No. 0704-0188

Public reporting burden for this collection of information is estimated to average 1 hour per response, including the time for reviewing instructions, searching existing data sources, gathering and maintaining the data needed, and completing and reviewing the collection of information. Send comments regarding this burden estimate or any other aspect of this collection of information, including suggestions for reducing this burden, to Department of Defense, Washington Headquarters Services, Directorate for Information Operations and Reports (0704-0188), 1215 Jefferson Davis Highway, Suite 1204, Arlington, VA 22202-4302. Respondents should be aware that notwithstanding any other provision of law, no person shall be subject to any penalty for failing to comply with a collection of information if it does not display a currently valid OMB control number.

PLEASE DO NOT RETURN YOUR FORM TO THE ABOVE ADDRESS.

1. REPORT DATE *(DD-MM-YYYY)*	2. REPORT TYPE	3. DATES COVERED *(From – To)*
28-9-2011	Final	Feb 2011 – Sept 2011

4. TITLE AND SUBTITLE
Hybrid Axial and Cross-Flow Fan Propulsion for Transonic Blended Wing Body Aircraft

5a. CONTRACT NUMBER
NNX11CD95P

5b. GRANT NUMBER

5c. PROGRAM ELEMENT NUMBER

6. AUTHOR(S)
Kummer, Joseph, D
Allred, Jimmie, B

5d. PROJECT NUMBER

5e. TASK NUMBER

5f. WORK UNIT NUMBER

7. PERFORMING ORGANIZATION NAME(S) AND ADDRESS(ES)
Propulsive Wing, LLC
321 Rt. 5, PO Box 321, Elbridge, NY 13060

8. PERFORMING ORGANIZATION REPORT NUMBER

9. SPONSORING/MONITORING AGENCY NAME(S) AND ADDRESS(ES)
NASA Glenn Research Center
21000 Brookpark Road
Cleveland, OH 44135

10. SPONSORING/MONITOR'S ACRONYM(S)
GRC

11. SPONSORING/MONITORING REPORT NUMBER

12. DISTRIBUTION/AVAILABILITY STATEMENT

13. SUPPLEMENTARY NOTES

14. ABSTRACT
Ideally, standard fan/engine designs can directly be embedded within the airframe of a vehicle. Unfortunately, doing so causes both performance penalties and structural challenges due to boundary layer flow ingested into the propulsors. For the present design concept, a dual-propulsion axial fan (AF) and cross-flow fan (CFF) system is investigated. This system provides the excellent efficiency of the axial fan, but with the benefit of the cross-flow fan system providing boundary layer flow mitigation. The purpose of this research was to develop the necessary computational tools to analyze this configuration, and then to show that the combined propulsor solution has performance benefits over the single axial fan system. Results from the CFD simulations clearly demonstrate the potential for reducing the efficiency penalty incurred by the axial fan due to inlet non-uniformity. Axial fan compression efficiency improvements of up to 2.5% were shown when the CFF propulsor was included in the calculation. In addition, clear trends exist between net lift and drag coefficients, total pressure ratio, and fan parameters. Lastly, the CFD data showed significant changes in the flow field around both the 2D airfoil, as well as the full 3D blended-wing-body vehicle due to the inclusion (or exclusion) of the distributed propulsors. This demonstrates that it is impossible to segregate the airframe force calculations from those for the individual fans. Instead, net lift and net drag must be calculated by directly integrating pressure and shear forces around all external surfaces, including the pressure force over the inlet and outlet control surfaces, and then adding to these values the force due to the momentum fluxes through the propulsors.

15. SUBJECT TERMS
Distributed, embedded propulsion; Dual axial/cross-flow fan propulsion; Blended-wing-body; Wake ingestion

16. SECURITY CLASSIFICATION OF:			17. LIMITATION OF ABSTRACT	18. NUMBER OF PAGES	19a. NAME OF RESPONSIBLE PERSON
a. REPORT	b. ABSTRACT	c. THIS PAGE	None	75	Joseph Kummer
U	U	U			19b. TELEPHONE NUMBER *(Include area code)* 315-252-2559